AD-A238 159

NAVAL POSTGRADUATE SCHOOL
Monterey, California

DTIC
ELECTE
JUL 15 1991
S B D

THESIS

ABLATIVE HEAT SHIELD STUDIES
FOR
NASA MARS/EARTH RETURN ENTRY VEHICLES

by

Michael K. Hamm

September, 1990

NASA Thesis Advisor: William D. Henline
Thesis Co-Advisor: Max F. Platzer

Approved for public release; distribution is unlimited.

91-04919

91 7 12 648

REPORT DOCUMENTATION PAGE

Form Approved
OMB No. 0704-0188

1a REPORT SECURITY CLASSIFICATION UNCLASSIFIED	1b RESTRICTIVE MARKINGS

2a. SECURITY CLASSIFICATION AUTHORITY	3 DISTRIBUTION/AVAILABILITY OF REPORT
2b. DECLASSIFICATION/DOWNGRADING SCHEDULE	

4. PERFORMING ORGANIZATION REPORT NUMBER(S)	5 MONITORING ORGANIZATION REPORT NUMBER(S)

6a. NAME OF PERFORMING ORGANIZATION Naval Postgraduate School	6b OFFICE SYMBOL (If applicable) 31	7a. NAME OF MONITORING ORGANIZATION Naval Postgraduate School

6c. ADDRESS (City, State, and ZIP Code) Monterey, CA 93943-5000	7b. ADDRESS (City, State, and ZIP Code) Monterey, CA 93943-5000

8a. NAME OF FUNDING/SPONSORING ORGANIZATION	8b OFFICE SYMBOL (If applicable)	9 PROCUREMENT INSTRUMENT IDENTIFICATION NUMBER

8c. ADDRESS (City, State, and ZIP Code)	10 SOURCE OF FUNDING NUMBERS			
	PROGRAM ELEMENT NO	PROJECT NO	TASK NO	WORK UNIT ACCESSION NO

11. TITLE (Include Security Classification) ABLATIVE HEAT SHIELD STUDIES FOR NASA MARS/EARTH RETURN ENTRY VEHICLES (UNCLASSIFIED)

12. PERSONAL AUTHOR(S) Hamm, Michael, K.

13a TYPE OF REPORT Master's Thesis	13b TIME COVERED FROM _____ TO _____	14. DATE OF REPORT (Year, Month, Day) Sept 90	15 PAGE COUNT 122

16 SUPPLEMENTARY NOTATION The views expressed in this thesis are those of the author and do not reflect the official policy or position of the Department of Defense or the U.S. Government

17	COSATI CODES		18. SUBJECT TERMS (Continue on reverse if necessary and identify by block number)
FIELD	GROUP	SUB-GROUP	Ablative, Hypersonic, NASA, Mars, Heat Shield

19 ABSTRACT (Continue on reverse if necessary and identify by block number)

The research performed in this thesis is to determine the ablative behavior of ceramic Reusable Surface Insulation (RSI) materials in a hypersonic high enthalpy flow that i used to simulate entry into Earth atmosphere. Actual arc jet experimer ts were performed to measure mass loss, melt run off, and fiber collapse of these materials and compare the experimental results with predicted theoretical values. The tests were performed to ascertain if RSI type materials could be used for entry vehicles proposed in NASA Mars missions.

20 DISTRIBUTION/AVAILABILITY OF ABSTRACT ☒ UNCLASSIFIED/UNLIMITED ☐ SAME AS RPT ☐ DTIC USERS	21 ABSTRACT SECURITY CLASSIFICATION Unclassified
22a. NAME OF RESPONSIBLE INDIVIDUAL William D. Henline / Max F. Platzer	22b TELEPHONE (Include Area Code) 408-646-2311 22c OFFICE SYMBOL 67

Ablative Heat Shield Studies

for

NASA Mars/Earth Return Entry Vehicles

by

Michael K. Hamm

Lieutenant, United States Navy

B.A., University of Colorado,Boulder

Submitted in partial fulfillment

of the requirements for the degree of

MASTER OF SCIENCE IN AERONAUTICAL ENGINEERING

from the

NAVAL POSTGRADUATE SCHOOL

September, 1990

Author: _____

Michael K. Hamm

Approved by: _____

William D. Henline, NASA Thesis Advisor

_____

Max F. Platzer, Thesis Co-Advisor

_____

M.S. Chandrasekhara, Second Reader

_____

E. Roberts Wood, Chairman

Department of Aeronautics and Astronautics

ii

ABSTRACT

The research performed in this thesis is to determine the ablative behavior of ceramic Reusable Surface Insulation (RSI) materials in a hypersonic high enthalpy flow that is used to simulate entry into Earth atmosphere. Actual arc jet experiments were performed to measure mass loss, melt run off, and fiber collapse of these materials and compare the experimental results with predicted theoretical values. The tests were performed to ascertain if RSI type materials could be used for entry vehicles proposed in NASA Mars missions.

TABLE OF CONTENTS

LIST OF SYMBOLS

Nomenclature

B' - dimensionless mass loss rate

C_H - surface heat transfer coefficient, lbm/ft^2sec

C_p - material heat capacity, BTU/lbm °R

E - energy reference

h_w - wall enthalpy, BTU/lbm

H_s - total enthalpy at shock location, BTU/lbm

K_T^m - thermal conductivity, BTU/ft sec °R

M - mass reference, lbm

$\dot{M}$ - mass flow rate, lbm/sec

P_e^o - stagnation pressure, atm

q - heat flux, BTU/ft^2 sec

Q - heat transfer coefficient, lbm^2/ft^4 sec^2

R_n - model nose radius, ft

R_v - spectral reflectivity

s - streamline distance coordinate

t - time, sec

T - temperature, °R

U - tangential velocity

V - normal velocity component

V_{∞} - freestream velocity, ft/sec

y - surface normal coordinate

Subscripts and Superscripts

e - edge reference

m - melt reference

o - initial

obs - observed by experimentation

rad - radiative reference

S - references for shock location

s - surface reference

T - total

v - vaporization reference

w - wall reference

$/$ - derivative

Greek Symbols

δ - *characteristic thickness, ft*

ε - *void fraction*

ε_s - *suface emissivity*

λ - *blowing rate correction factor*

μ - *viscosity*

ψ - *function of mass loss and heat transfer coefficient*

ρ - *density, lbm/ft^3*

σ - *Stefan-Boltzmann constant*

τ - *shear force*

ACKNOWLEDGMENT

I. INTRODUCTION

A. GENERAL BACKGROUND

The return from space to earth requires a heat shield that provides adequate thermal protection for the return vehicle against hypersonic aerodynamic surface frictional heating, yet has minimal weight. The purpose of this thesis is to determine if less dense heat shield materials can be used in this application and if the recessional rates of the lighter materials are proportional to the density. The results of this study may influence the design of proposed NASA Mars missions.

High enthalpy, hypersonic glassy ablators have been proposed for the NASA Mars Rover Sample Return Mission (MRSR). This utilizes an Apollo type capsule for Earth aerocapture (use of the Earth's atmosphere to slow the vehicle) upon return from Mars. The proposed preliminary capsule sketch design is shown in Figure 1 [Ref. 1] with the trajectory plot of the proposed aerocapture profile shown in Figure 2 [Ref. 1]. The requirements imposed by such a trajectory indicate the need for an ablative type heat shield. This requires a preliminary study of both the heat shield energy balance and surface recession equations.

The primary calculations for the aerocapture profile assume laminar equilibrium boundary layer flow over the entire nose radius of the capsule. This assumption, is of course, an oversimplification and turbulent flow is expected in portions of the shock layer, which will increase the surface heating and recession rates of the aerocapture return vehicle.

As shown by Henline [Ref. 1], based on a model for porous glassy ablators, the Earth return profile surface recession for the MRSR vehicle is estimated to be 0.22 inches, with the heat shield ablative material being composed of LI 2200 RSI.
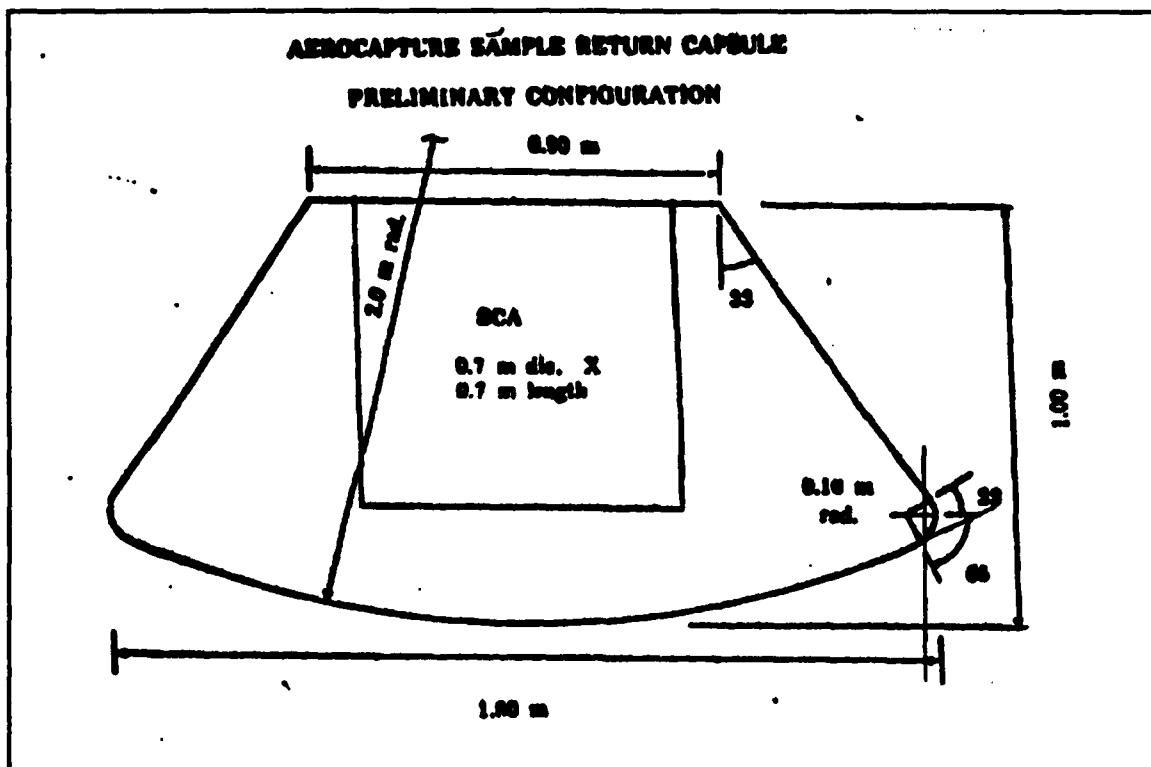
1

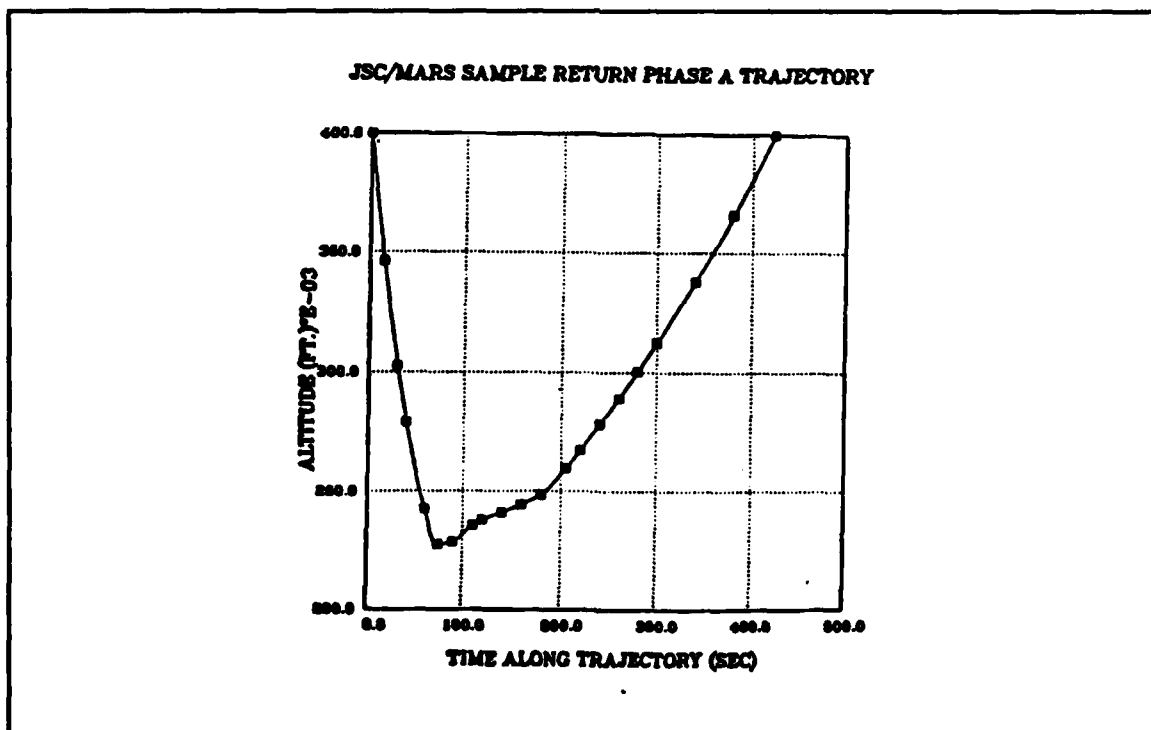**Figure 1** Mars Return Capsule Sketch

Figure 2 Trajectory Profile

2

The following experiments are designed to assess if the surface recession predictions set forth for the MRSR vehicle are valid and determine the governing energy balance and surface recession equations.

B.   ABLATIVE MATERIALS

Returning from space, the problem of reentry involves dissipating the excess kinetic energy acquired when a body is placed into orbit. The return to Earth transforms the potential energy into kinetic energy, which is then converted to frictional heat energy. The vehicle must then be protected from this hypersonic frictional reentry heating. Early space reentry vehicles used charring ablators for their surface thermal protection. This ablative process uses the heat of thermal decomposition and the surface material heat of vaporization to block the hypersonic surface frictional heating.

Glassy ablators are thought to be able to provide the necessary protection and weight savings needed for a space reentry vehicle. Among the first studies of glassy ablators were the investigations of Tektites [Ref. 2]. Tektites are meteorites that have possible origin as debris from a meteor impact on the moon. This impact propagated molten glass into space, which then hardened into spheres and traveled to Earth. Upon entering the Earth's atmosphere they experienced hypersonic surface frictional heating. The behavior of Earth entry on these glassy spheres was studied and simulated [Ref. 2]. Tektite behavior during Earth entry sparked further study and development of glassy ablators which are currently being studied for use on Earth reentry vehicles.

Glassy ablators mitigate the aerodynamic heating by several mechanisms. These include the latent heat of vaporization of the ablating surface material, transpiration (absorption of energy by the vaporized surface material as it propagates away from the ablating surface) or convective blockage, viscosity changes of the glassy material from a semi solid amorphous material to a viscous liquid flowing material, emission of radiant energy from the ablating surface, transmission, and absorption of the incident radiation through the surface of the ablative material [Fig. 3].
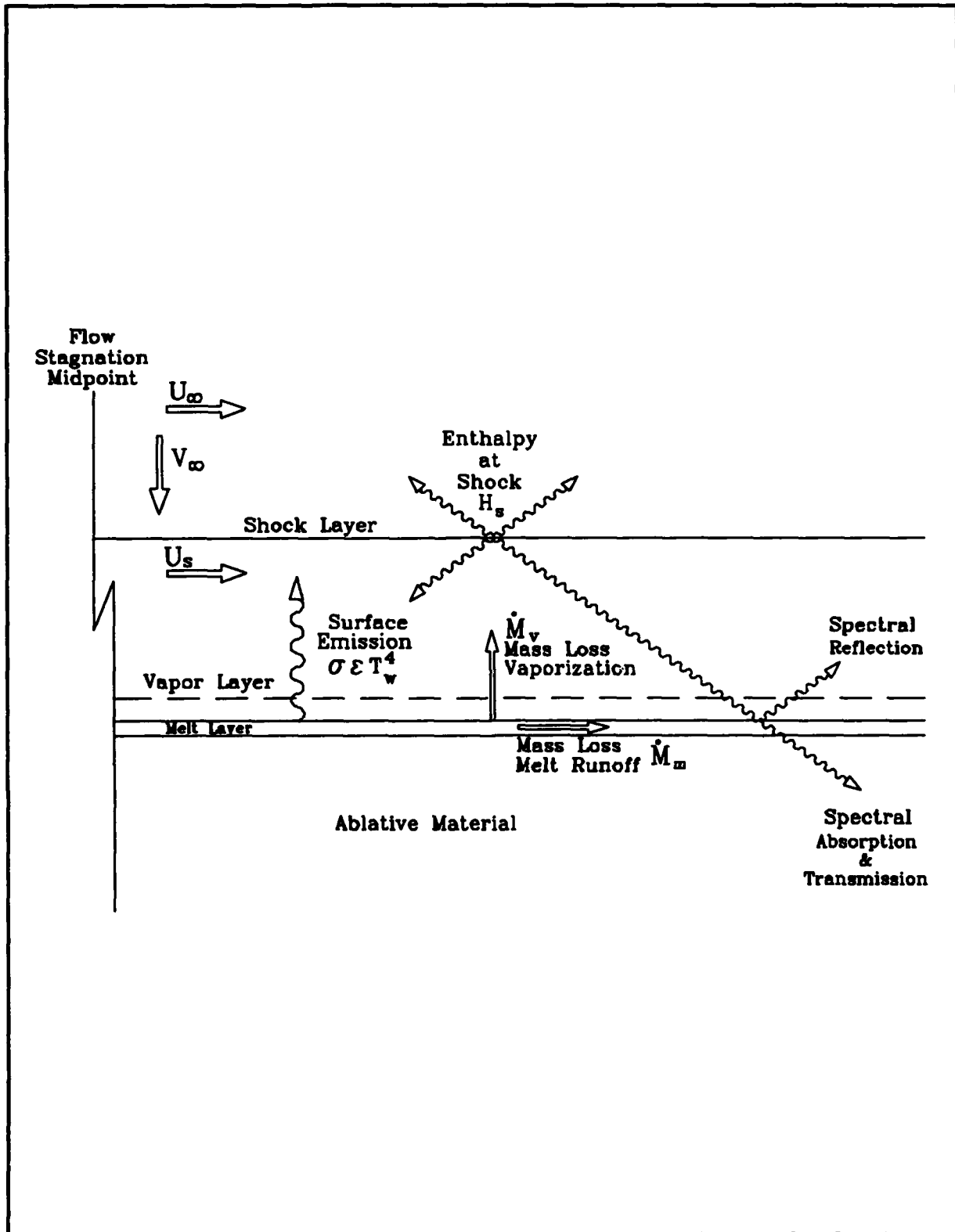
3

Figure 3 Energy Flow Model

Reusable Surface Insulation

A material that behaves like a glassy ablator on the surface, has a low thermal conductivity, is structurally tough, lightweight, and is in some sense reusable, would be desirable for the protective heat shield used on Earth entry vehicles. A material for this purpose has been developed that utilizes silicon dioxide (fused quartz) in a fibrous packed matrix forming blocks which can behave as a glassy ablator on the surface when subject to very high surface heat fluxes. It is also lightweight, reusable, and has a low thermal conductivity. These fibrous silicon dioxide blocks are called Reusable Surface Insulation (RSI), and are given the designation by the manufacturer, Lockheed Insulation (LI) followed by one hundred times the material density per cubic foot. The primary constituent of the RSI material is silicon dioxide, but may contain other compounds (e.g. alumina borosilicate) to affect the thermal and physical properties.

Since RSI has a much lower thermal conductivity than quartz, as well as being a tough material structurally, it is proposed that the RSI be used as an ablative surface for Earth return vehicles. On the Space Shuttle for example, the RSI is used as a radiatively cooled surface insulation. The density of RSI is up to 16 times less than solid quartz and has a much lower transmissivity allowing less radiant energy to propagate to the back face of the material. Since RSI is virtually opaque it has virtually no relative transmissivity. These properties make RSI potentially a more viable source for a glassy ablative heat shield material than solid quartz.

C. REENTRY MODELING

The hypersonic frictional heating of reentry needs to be modeled both mathematically and physically so that simulations of the flow and resultant response of the ablative material to the surface heating may be closely studied. Before a complete Earth entry model can be developed and expanded to

encompass all parameters, verification of basic parameters of the ablative process must be established. Basic experimentation to refute or verify the theoretical predictions established for ablative materials entering Earth's atmosphere must be performed. The high enthalpy flow of hypersonic Earth entry can be approximated in an arc jet. This is essentially a high enthalpy hypersonic wind tunnel. The arc jet is the primary experimental apparatus in which RSI models will be inserted to study their ablative behavior. The RSI ablative behavior observed in the arc jet tests will be compared to theoretical predictions. Correlation studies will be made between the mathematical model and physical model to determine if use of RSI materials are feasible for the proposed future NASA Mars missions.

The primary thermal/ablative response model for both solid and porous (RSI) ablators is outlined in the following section.

II. MATHEMATICAL MODELING

A. MELTING ABLATOR THEORY

Melting ablators are composed of two material types. One is a melting solid, which may be a pure crystalline structure or an impure solid. These melting solids have a distinct melting point and latent heat of fusion. The other material group includes highly viscous semi solid materials, which have no distinct phase transition point and no latent heat of fusion. Quartz and glass materials will perform as glassy ablators and are part of the second ablative material group. The following discussion pertains solely to a mathematical model for glassy ablators.

The region of interest and study is the hemispherical ablation model stagnation point, which is where equilibrium flow conditions are assumed [Fig. 3]. The melt layer at the stagnation point is assumed very thin compared to the surface radius of curvature of the ablating material (approx 0.2 mm) and extends outward from the stagnation point until the temperature lowers to the material congealing point.

As shown by Bethe and Adams [Ref. 3] the melt layer region will be a very small portion of the total volume and for a typical heat shield on a reentry vehicle, the primary region of interest will be a spherical stagnation region in which the melt flow can be envisioned as very thin and axisymmetric. The melt layer can also be considered as an incompressible flowing liquid layer and the equations governing this liquid layer are very similar to the case of an incompressible gas boundary layer for the coordinate system shown [Fig. 4]. The three basic energy equations for solid glassy ablators applicable to the experimental arc jet flow are,

CONTINUITY

$$\frac{\partial(U_m r)}{\partial s} + \frac{\partial(V_m r)}{\partial y} = 0 \qquad (1)$$

7

Figure 4 Flow Model Orientation

S MOMENTUM

$$\frac{\partial U_m}{\partial t} + U_m \ \frac{\partial U_m}{\partial s} + V_m \ \frac{\partial U_m}{\partial y} - \frac{\partial}{\partial y} \ [\mu_m \frac{\partial U_m}{\partial y}] - \frac{1}{\rho_m} \ \frac{\partial P_m}{\partial s} \tag{2}$$

8

ENERGY

$$\frac{\partial h_m}{\partial t} + U_m \frac{\partial h_m}{\partial s} + V_m \frac{\partial h_m}{\partial y} - \frac{1}{\rho_m} \frac{\partial}{\partial y} [K_T^m \frac{\partial T_m}{\partial y}] \qquad (3)$$

Radiation will not enter these surface ablation equations since all testing is in arc jet flow; whereas, in the flight condition case, the radiative heat terms would not be disregarded.

These three basic equations for solid glassy ablators are developed to provide the total stagnation point linear recession rate due to ablation for solid glassy materials. To ascertain the general behavior of these three basic equations [Eq. 1-3], a dimensionless order of magnitude analysis must be performed, as shown by Henline [Ref. 1]. The quantities considered known at this point are the heat shield nose radius and the various transport and thermodynamic properties. The melt layer superficial flow velocity and the vehicle nose radius, together with the given transport coefficients are used as reference values. The temperature used, for the transport properties, is the melt surface vaporization temperature. This analysis results in three dimensionless groups of relative transport events, (free convection, forced convection and conduction) which occur over the entire distance between the shock layer and the back face of the ablative material [Fig. 3]. This region is mathematically and physically continuous. In some cases this region will contain frothing and bubbling of the ablative surface from vaporization or transpiration. The highly nonlinear dependency of the viscosity of glasses strongly couples the solution of the momentum equation to the solution of the energy equation. To obtain a useful theory without extensive numerical analysis, some assumptions and approximations must be made to solve Equation 3. From the Bethe and Adams [Ref. 3] simplified energy Equation 3, along with assuming a quasi static melt layer and by noting that the melt velocity u_m is linear in the s direction near the stagnation point [Fig. 4], the numerical analysis can be avoided. In general the surface temperature is not known and must be determined as a result of the complete shock layer/melting ablator, coupled solution. An additional presumption that the glass

9

a specific vapor pressure in accordance with thermochemical equilibrium at the surface is made. For high heat fluxes the melt surface temperatures will be at or near the glass equilibrium vapor pressure (boiling point). Further development and integrations of the three basic equations develop into a qualitative explicit expression for the total ablation rate.

$$V_T = V_v + \frac{2\delta_m^2}{\mu_m^e} \; [\tau_m^{e'} - 2\delta_m P_m^{''}] \qquad (4)$$

Which can be further developed based on a Reynolds analogy at the ablative surface to give,

$$V_T \approx V_v + 2\frac{\delta_m^2}{\mu_m^e} \left[\frac{\rho_m V_m}{R_n} \sqrt{\frac{2P_{e_o}}{\rho_m}} + 4\delta_m \frac{P_{e_o}}{R_n^2} \right] \qquad (5)$$

The mass loss rate as a function of recessional velocity are written,

$$\dot{M}_T = \dot{M}_v + \dot{M}_m \qquad (6)$$

$$\dot{M}_T = \rho_m V_T \qquad (7)$$

$$\dot{M}_v = \frac{\delta M_T}{\delta t} \qquad (8)$$

This total ablation rate calculation allows for the development of the stagnation region surface energy balance.

$$\rho_s U_s C_{H_t} [H_s - h_w] - \dot{M}_V H_V - \sigma T_{w1}^4 = \dot{M}_T C p_m (T_w - T_O) \qquad (9)$$

Due to the arc jet flow conditions the shock layer radiative heat flux q_v and the surface reflectivity of RSI, R_v are both assumed zero.

In the case of porous (RSI) ablators, the material has a void fraction of 85%-95%. This significant void fraction will strongly influence the thermophysical and transport properties of the melting and ablating RSI materials. This influence is currently unknown but is modeled by a linear functionality [Ref. 1].

For this reason a revised expression must be derived for the surface recession of RSI materials to account for the high void fraction. The density for RSI is expressed as a linear function of the fully dense solid such that the melting RSI density is $\rho_\epsilon = \rho_m(1-\epsilon)$, where $\epsilon = \epsilon(t,T,P)$ in the melt layer of the RSI, being a function of time, temperature, and pressure. The viscosity of the RSI is assumed to behave in the same linear fashion with the RSI viscosity $\mu_\epsilon = \mu_m(1-\epsilon)$. The simplified equations for RSI materials are represented by

CONTINUITY

$$\frac{\partial(\rho_m U_m r (1-\epsilon))}{\partial s} + \frac{\partial(\rho_m V_m r (1-\epsilon))}{\partial y} = 0 \qquad (10)$$

S MOMENTUM

$$\frac{\partial}{\partial y}(\mu_m(1-\epsilon)) \frac{\partial U_m}{\partial y} = \frac{\partial P_m}{\partial s} \qquad (11)$$

ENERGY

$$\rho_m(1-\epsilon) \, Cp V_m \frac{\partial T_m}{\partial y} = \frac{\partial}{\partial y} \left[K_T^m \frac{\partial T_m}{\partial y}(1-\epsilon) \right] \qquad (12)$$

11

Using the same integration procedures as for the solid glass, the total recessional velocity for the porous material is

$$V_T \approx \frac{V_v}{(1-\epsilon)} + \frac{4}{3} \frac{(1-\epsilon_O)^2 \delta_m^2}{\mu_m^{\bullet}} \left[\tau_m^{\epsilon'} - \frac{3}{2} (1-\epsilon_O) \delta_m P_m \right] \qquad (13)$$

Comparing the equation of the total melt runoff from the non-porous glass it can be seen the melt velocity is approximately proportional to $(1-\epsilon^2)$, which suggests that the melt layer for RSI, porous ablators, should be negligible (this is verified by microscopy in Chapter 5).

The recession and energy equations developed in Equations 12 and 13 are the basis for the experiments to test the theoretical versus actual recession rates and behavior characteristics of porous as well as non-porous glassy ablators which are discussed below.

B.   ENERGY BALANCE AND CORRELATIONS FOR DATA ANALYSIS

Most current mathematical models for glassy ablative materials have part of their origin from the Bethe and Adams work [Ref. 3]. The complete ablative process is comprised of many mechanisms; these include surface shear, melt flow, heat conduction, convective energy blockage due to blowing, and surface radiation emission. All these energy fluxes account for subgroups of the total energy balance. The whole ablative process involving these different mechanisms must be combined in such a fashion that the net surface recession rate and surface temperature can be predicted consistently with respect to the experimental data. The mathematical functionality of each subgroup must also fit the observed physical behavior characteristics and basic laws of physics. Sometimes the mathematical functions of a subgroup cannot be verified with the current technology and the measurements taken must be assumed correct in concept and functional trend.

12

The thermodynamic system for these energy balance equations are confined to the effective heat fluxes of the arc jet, the physical arc jet model itself and all its surfaces, and all energy emissions from the arc jet model while in the arc jet flow. During the ablation process thermochemical equilibrium is assumed at the stagnation point.

From Equation 9, specific modifications are made to simplify and revise the equation parameters.

$$\rho_s U_s C_{H_t} \quad [H_s - h_w] - \dot{M}_V H_s - \sigma \epsilon_s T_w^4 = \dot{M}_m Cp(T_w - T_0) \qquad (14)$$
$$term1 \qquad term2 \qquad term3 \quad term4 \qquad term5$$

The first term $\rho_s U_s C_{H_t}$ is the ablating surface heat transfer coefficient defined below and is a function of flow enthalpy, pressure, effective nose radius, and free stream velocity.

$$Q_t = \rho_s U_s C_{H_t} \qquad (15)$$

The following empirical expressions are available to represent Q_t in the arc jet [Ref. 4] and are simplified for these test conditions. Q_t is a function of the dimensionless blowing rate parameter B'.

$$B' = \frac{\dot{M}}{Q_t} \qquad (16)$$
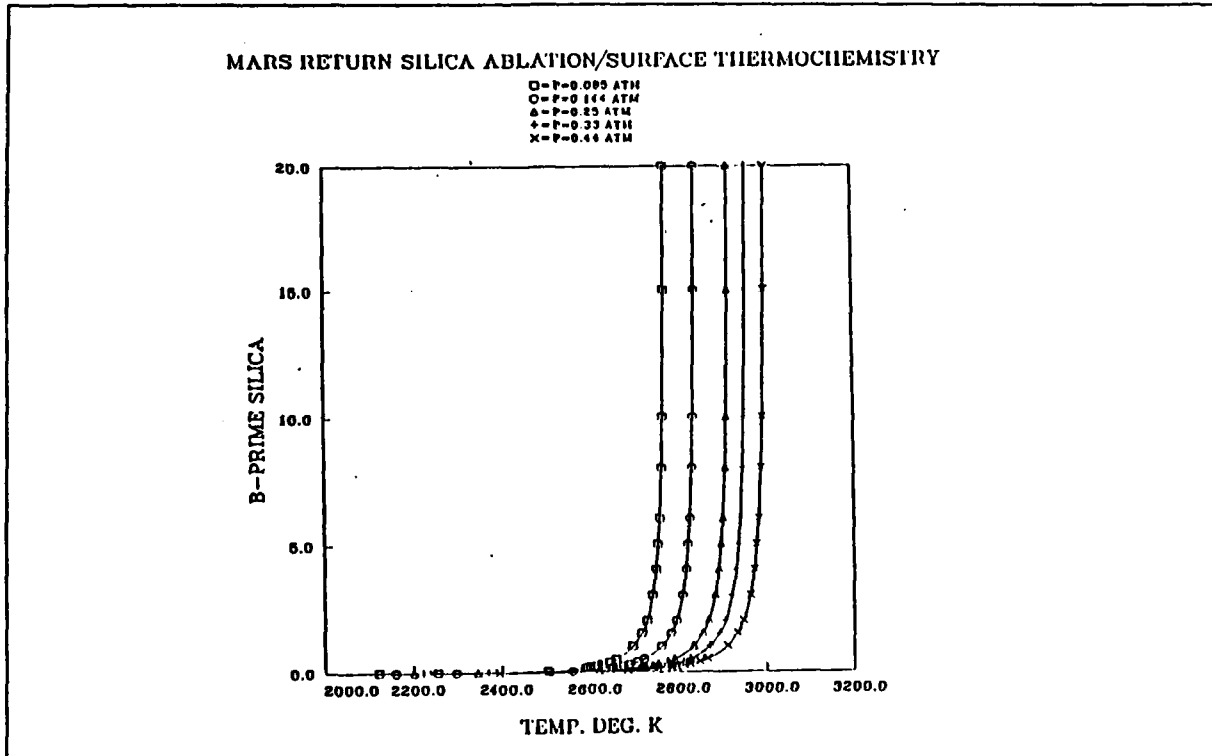
$$Q_t = \psi \, Q_0 \qquad (17)$$

13

Figure 5 B' Curve

$$\psi = \cfrac{\cfrac{2\lambda \dot{M}_v}{Q_0}}{Q_0 \left[e^{\frac{2\lambda \dot{M}_v}{Q_0}} - 1 \right]} \qquad (18)$$

$$Q_0 = \rho_v U_v C_{H_0} = \frac{89.74}{H_s} \left[\frac{V_\infty}{10000} \right]^2 \sqrt{\frac{P_{\theta_0}}{R_n}} \qquad (19)$$

Equation 19 has been taken from the Marvin and Deiwert [Ref. 5] cold wall heat transfer coefficient correlation for arc jets.

Term one in Equation 14 is an estimate of the arc jet heat flux to the arc jet model during the test. The model stagnation point heat flux decreases with time as the surface ablates and increases the effective nose radius of the model. This term also allows for the time variance of the heat transfer coefficient from the flow into the model as a function of time dependent model shape change.

14

Term two in Equation 14 is the difference in the arc flow total stagnation enthalpy H_s and the wall surface enthalpy of the ablating material.

$$h_w = Cp[T_w - T_0] \qquad (20)$$

Resulting in a total energy flux into the system of

ENERGY INTO SYSTEM

$$E_{in} = Q_t [H_s - h_w] \qquad (21)$$

Term three is the energy lost due to heat of vaporization of the surface ablating material.

VAPORIZATION ENERGY OUT OF SYSTEM

$$E_{v_{out}} = \dot{M}_v H_w \qquad (22)$$

$$H_w = h_w + \Delta H_v \qquad (23)$$

Term four is the energy lost due to emitted radiant energy from the surface. The emissivity of the surface is accounted for in this equation by the fact that the observed calibrated pyrometer radiant brightness temperature is used for the radiant energy flux out.

RADIANT ENERGY OUT

$$E_{rad} = \sigma T_{W_{obs}}^4 \qquad (24)$$

The observed temperature $T_{W\,obs}$ is experimentally obtained from disappearing wire pyrometer readings. Term five is the energy lost to combined melt cap runoff and in depth heat conduction.

15

MELT RUNOFF ENERGY

$$E_{m_{RO}} = \dot{M}_T \, Cp \, (T_w - T_O) \qquad (25)$$

The revised energy balance equation for solid glassy ablators is now

ENERGY BALANCE EQUATION

$$Q_t \, [H_s - h_w] - \dot{M}_V \, H_w = \sigma \, T_{w_{obs}}^4 + \dot{M}_T \, h_w \qquad (26)$$

To solve the energy balance equation, empirical values for total mass loss rate, calculated by recession rate measurements, and observed surface ablation temperature by disappearing wire pyrometer readings, are obtained. The free stream velocity, total flow enthalpy, and flow stagnation pressure are calculated from calibration data for the 60 megawatt Interactive Heating Facility and a computer program for isentropic nozzle flow expansion. The surface emissivity term will be unity since emitted radiant flux is based on measured surface temperature through the disappearing wire pyrometer (based on black body calibration). Known empirical data, observed experimental data, and calculated data from the behavior of the B' curve [Fig. 5], which represents dimensionless vaporization rate at the surface, will be used to iteratively solve for the vaporization and melt mass components of the total mass loss rate.

III. EXPERIMENTAL PROCEDURES

A.   OVERVIEW

The purpose of this experimentation is to obtain vital physical data needed to complete the melting ablator energy balance equation [Eq. 26], other objectives include determination of mass loss rates, ablative surface temperatures, ablation rates, and ablation mechanics. This information will allow a test of the mathematical model prediction of the melt and vaporization rates to see if these are consistent with the measured total recession rates. If so, the ratio of the melt to vaporization rate, and the dependence of this on the system conditions will help define the material ablative efficiency and characterize its general behavior. To obtain the required data, different combinations of ablative materials, pressures, and heat fluxes were used for observation in the 60 megawatt Interactive Heating Facility (arc jet).

In addition to the primary experimental objectives, light and electron microscopy studies of the ablation samples were performed. Subsurface investigation on the behavior of the RSI fibers will enhance the physical ablation model mechanics. Calculations of the apparent surface emissivity, and pressure change effect on the physical ablative model will enable more accurate ablative rate predictions.

B.   TEST SEQUENCE

For all of the arc jet tests, the same basic sequence of events occurred in testing each arc jet model. After the fabrication of the bulk material, the model was machined to the test dimensions and had a sting mount attached. The model was then weighed and placed into the arc jet test chamber where it was subject to hypersonic high enthalpy flow conditions. The model was observed by recording equipment during the run. After the test run the model was photographed, weighed, measured, sectioned and micrographed (see Chapter 4).

The arc jet has many limitations some of which are: no direct measurement of the flow enthalpy, nonuniform heat fluxes throughout the arc stream, no direct measurement of the model ablative surface

temperature, and large amounts of background optical noise in optical spectral data. Despite all of the shortfalls associated with the arc jet, it is the only current means available to simulate high enthalpy hypersonic flow conditions. To complete the experimental data requirements needed in solving the energy balance equation, which are not provided by the arc jet test conditions, the optical data gathering equipment must provide the remaining necessary information to calculate the data. For this purpose, during the arc jet run an array of recording equipment was used to obtain such data.

The recording equipment used during each run was a high speed movie camera, which provided detailed images of the ablating model surface during the test. Still photographs of the model and ablating surface were also taken. A video recording camera, which provided instant feedback of the arc jet run. A disappearing wire pyrometer was used for determination of the apparent surface temperature of the ablating model. Also a spectrometer for spectral emission analysis radiating from the ablating model surface was used. This instrument suffered from large amounts of background noise and provided no conclusive information to this study.

The arc jet operation and control was performed by an arc jet technician at the arc jet control console. The operating procedures of the arc jet are outlined in the NASA arc jet manual [Ref. 6]. The arc jet conditions were run according to a preplanned test matrix.

Once the finished arc jet model was readied it was placed into the arc jet by mounting it onto a retractable water cooled swingarm (sting). The sting was in the standby position (see Chapter 4) until the arc jet flow was ready for model insertion. The arc jet was started and the flow stabilized after closing the model in the test chamber and evacuating the chamber to .0005 atmospheres pressure.

With the model in the standby position and the arc jet flow stabilized, the data recording equipment was started. The model was next inserted into the arc jet flow for the specified exposure time or less if the model began to fail. During the test run, all optical recording was automatic except for the disappearing wire pyrometer and the still photography, which were manually operated.

18

The disappearing wire pyrometer operates by adjusting an internal wire voltage and optical filtering to match the apparent color of the ablative model surface, which makes the wire in the viewfinder "disappear". The model was viewed by the disappearing wire pyrometer through a mirror attached to the inside wall of the arc jet test chamber [Fig. 8] so that the region containing the stagnation point could be seen.

During the arc jet run, all data recorders and cameras were recording continuously with multiple disappearing wire pyrometer readings being taken. Due to the dynamic surface recession of the model and the static mounting of the recording apparatus, the data recording zone on the model was approximated prior to the arc jet run. The ablating surface of the model would pass through the viewing range of the optical pyrometer and the preset mirror for the disappearing wire pyrometer. The recession rate of the arc jet model ultimately determined the total number of disappearing wire pyrometer read-outs possible during the arc jet run.

After the arc jet test run was completed the model was retracted into the standby position and the arc jet was shut down. The arc jet model was then removed from the sting and taken out of the test chamber. Limited model handling after the arc jet test preserved the ablative surface properties for later studies. Model internal structure observations of the arc jet model were made by sectioning and observing by light and electron microscopy (see Chapter 5).

IV. EXPERIMENTAL EQUIPMENT & TECHNIQUES

A.   60 MW INTERACTIVE HEATING FACILITY

The 60 megawatt Interactive Heating Facility (IHF) arc jet is a high enthalpy hypersonic wind tunnel in which an electric current is used to raise the internal energy level of the flowing medium, usually air, to a state which can be used to simulate reentry conditions of a body through the earth's atmosphere.
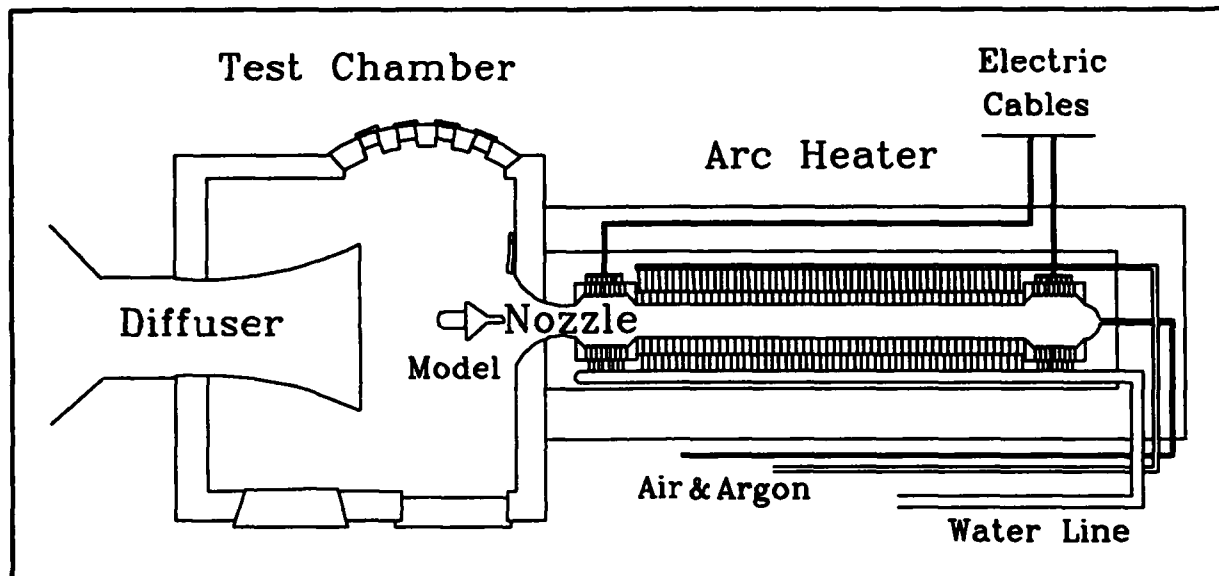

Figure 6 Arc Jet

The arc jet consists of four major components, the arc heater, nozzle, test chamber, and exhaust nozzle [Fig. 6].

1.   Arc Heater

The arc heater consists of a layered sequence of water cooled copper ring-annulus sections. At the upstream end of the arc heater is the electrode package for the anode and downstream prior to the nozzle is the cathode electrode package. Up to 8000 amps continuous current at 7000 volts can be fed through the NASA Ames 60 megawatt Interaction Heating Facility. The ring-annulus sections are cooled

20

by high pressure water circulating through each ring. The model heat flux may be adjusted by regulating the arc input current and the injected gas flow pressure. The operating parameters used in each test are based on prior heat flux calibration test runs.
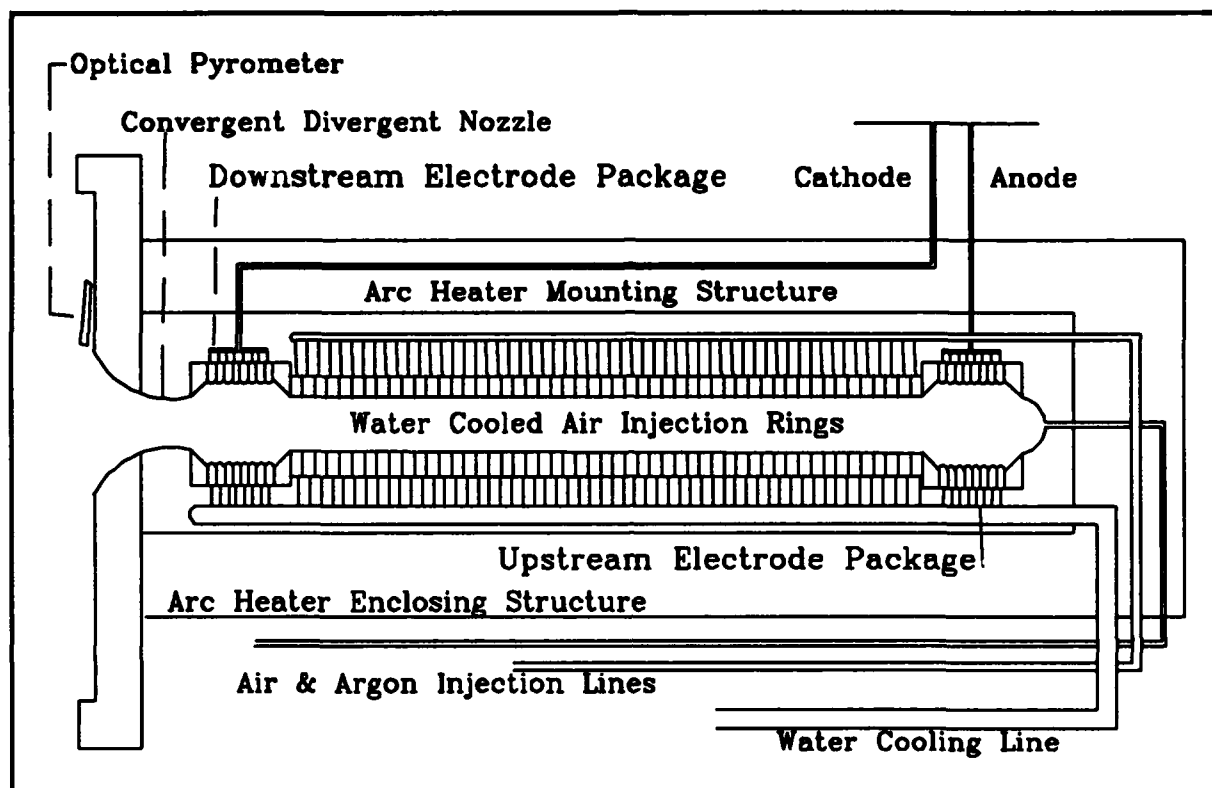
Figure 7 Arc Heater Section

2.   **Nozzle**

A convergent-divergent nozzle is attached to the downstream end of the arc heater section. The nozzle may be interchanged with other expansion ratio sizes to achieve different flow conditions. The nozzle in all of the following test runs had an exit diameter of 13 inches and an inlet diameter of 2.5 inches, for a geometric expansion ratio of 27. Test model placement distance from the nozzle exit determines the final flow expansion ratio, mach number, heat flux, and stagnation pressure at the model surface. The inlet gas manifolds control inlet gas pressures which regulate the downstream pressures.

Increasing the manifold pressure beyond a given point will only choke the flow in the convergent-divergent nozzle throat. So to obtain higher stagnation pressures the model must be moved closer to the convergent-divergent nozzle exit.

3. Test Chamber

The arc jet test chamber is a pressure vessel that houses the model mounting sting, traverse mechanisms, thermocouple conduits, cooling lines, observation windows, and diffuser [Fig. 8]. The model is mounted in the test section on the sting which is on a water cooled strut swing arm. The swing arm is prepositioned in standby while the arc flow conditions are being brought up to test conditions. The pressure inside the chamber is reduced to the test conditions prior to arc flow initiation. Opposing sides of the test section and the ceiling are equipped with plexiglass or quartz observation windows, these allow instrumented observation and documentation of the test run as well as a means for a safety observer to monitor the flow and abort the run if necessary.

4. Exhaust Nozzle

The diffuser is mounted inside the test chamber, which is attached to the steam plant which provides the vacuum for the test chamber and is directly behind the model in the flow stream [Fig. 8]. This large diameter, water cooled, copper diffuser is needed to capture the bow shock produced on the model and to prevent circulation of the flow. The diffuser inlet distance from the arc jet model may be increased or decreased to maintain proper flow and temperatures inside the test chamber.

B. ARC JET MODELS

1. Reusable Surface Insulation

To fabricate the RSI block, fibrous strands of pure spun silicon dioxide with a mean fiber diameter of .003 mm are immersed in water to make a slurry. The water silicon dioxide slurry is then
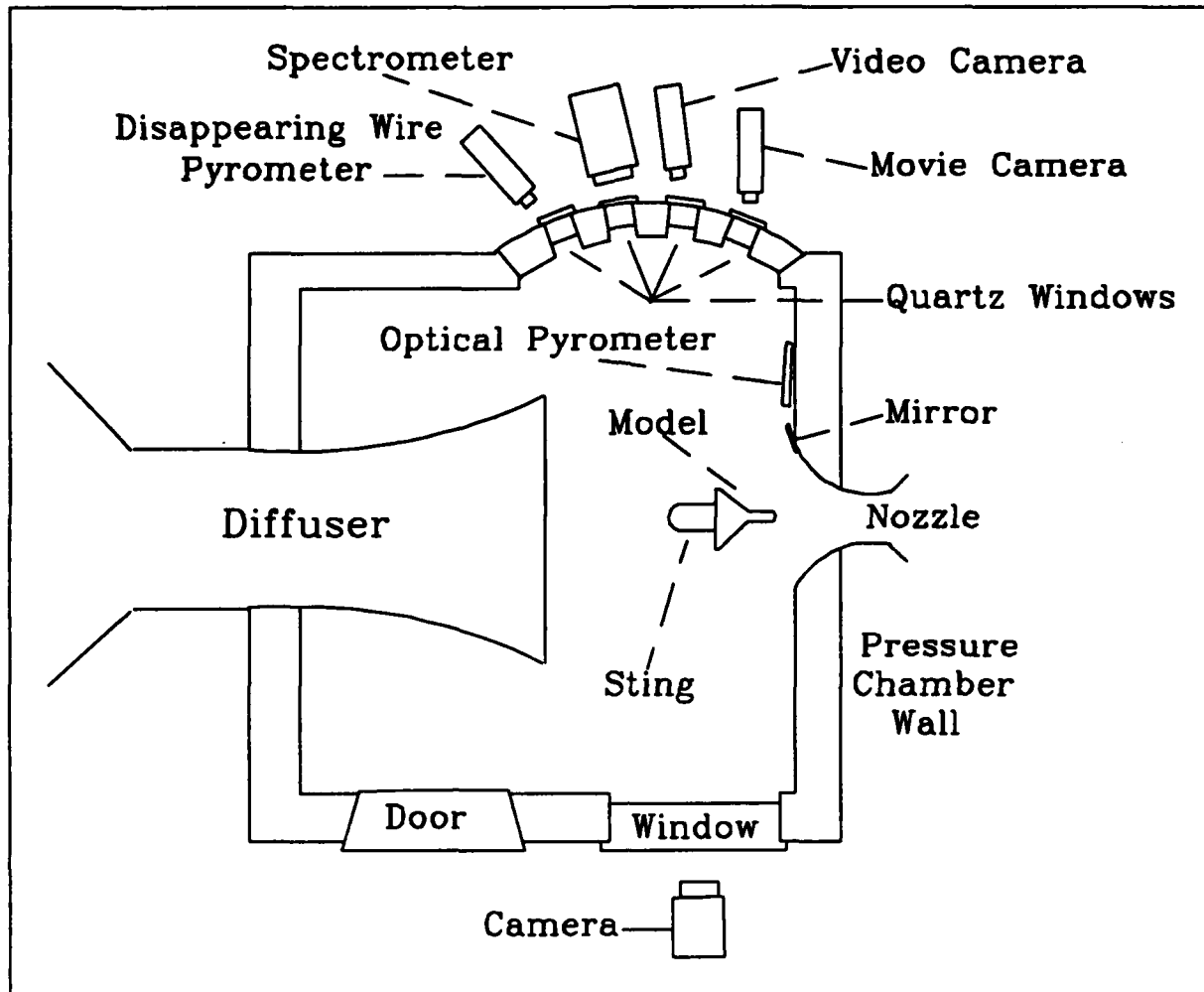
Figure 8 Test Chamber Section

placed into an agitation machine which breaks the silicon dioxide fibers into shorter stands, a process which increases the density of the silicon dioxide water matrix. When the desired density of the slurry has been reached the agitation process is terminated.

The water silicon dioxide slurry is then placed into a pressing apparatus, where the water is pressed out of the slurry mixture until the desired volume has been reached. The slurry cube is then placed into a firing oven (2450 deg F for 90 minutes), where the water evaporates and the silicon dioxide fibers are allowed to partially fuse together (sinter). The removal of the water and partial fusing of the silicon dioxide fibers transforms the slurry block into a lightweight rigid structure now capable of being machined into the proper arc jet test model dimensions.

23

The arc jet models are not composed of pure silicon dioxide. The LI 2200 models contain two percent silicon carbide in the form of minute crystals which are attached to the silicon dioxide fibers in the matrix of the partially fused fiber block [Fig. 9].

Figure 9 Silicon Cardide Crystals in LI 2200

24

2. Arc Jet Model Construction

The arc jet models were cut and machined from larger blocks of the raw material. Five

types of materials were used to make the models, LI 2200, LI 1800, LI 900, solid quartz, and solid
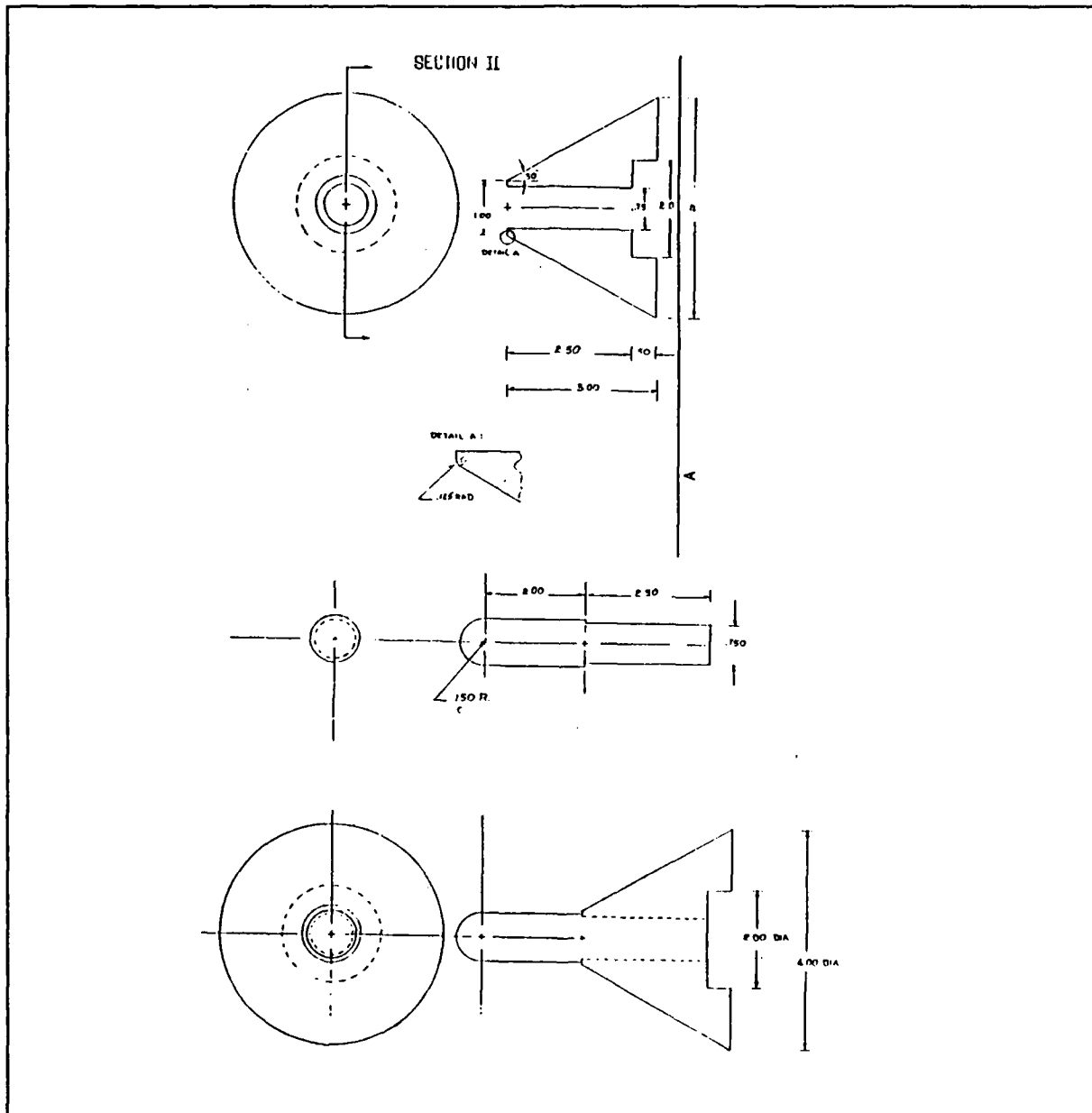
Figure 10 Section Models

graphite. The LI 2200, LI 1800, and LI 900 models were made entirely of the RSI material with a sting mount attached to the flared end by Room Temperature Vulcanizing (RTV) adhesive. The solid quartz and solid graphite models were made in sections [Fig. 10] so that the solid quartz, or graphite was inserted into a blown silica flared base (silfrax) and attached with RTV. The model dimensions are shown in Figure 11, the shape of the models was to provide a hemispherical surface with a uniform diameter rod behind so that the ablative properties could be determined. The hemispherical nose section was used to minimize shape change over that which would occur on a blunt or pointed surface. The aft section of the model is designed to protect the sting on the swing arm.

LI 2200 is composed of silicon dioxide fibers along with 2 percent silicon carbide pressed and cured into blocks which has a density of 22 pounds per cubic foot. LI 1800 and LI 900 however are composed of pure silicon dioxide fiber and are pressed and cured into blocks with a density of 18 and nine pounds per cubic foot respectively. These blocks are inspected and then cut into the approximate model size before being machined into the proper dimensions.

3.   Arc Jet Model Weights

Determination of the mass loss due to vaporization was important in correlating the experimental recession data model. Model weight before and after the arc jet runs were used to determine total mass loss due to vaporization. To determine if atmospheric water absorption into the models influenced their weight, which would bias the vapor mass loss depending on the relative humidity of the day of weighing, a test was performed to determine the percentage of the model weight that was absorbed atmospheric water. The test of dry weight versus wet weight (atmospheric) differed by .05 percent. This was judged to be a small enough difference to discontinue model oven drying. The solid quartz and graphite model inserts were inspected prior to weigning for anomalies that might affect the test run. After the arc jet run was complete each model was reweighed on the same scale after allowing the model to cool to room temperature. RSI model post test weighing allowed for no change in mass of the RTV adhesive

26
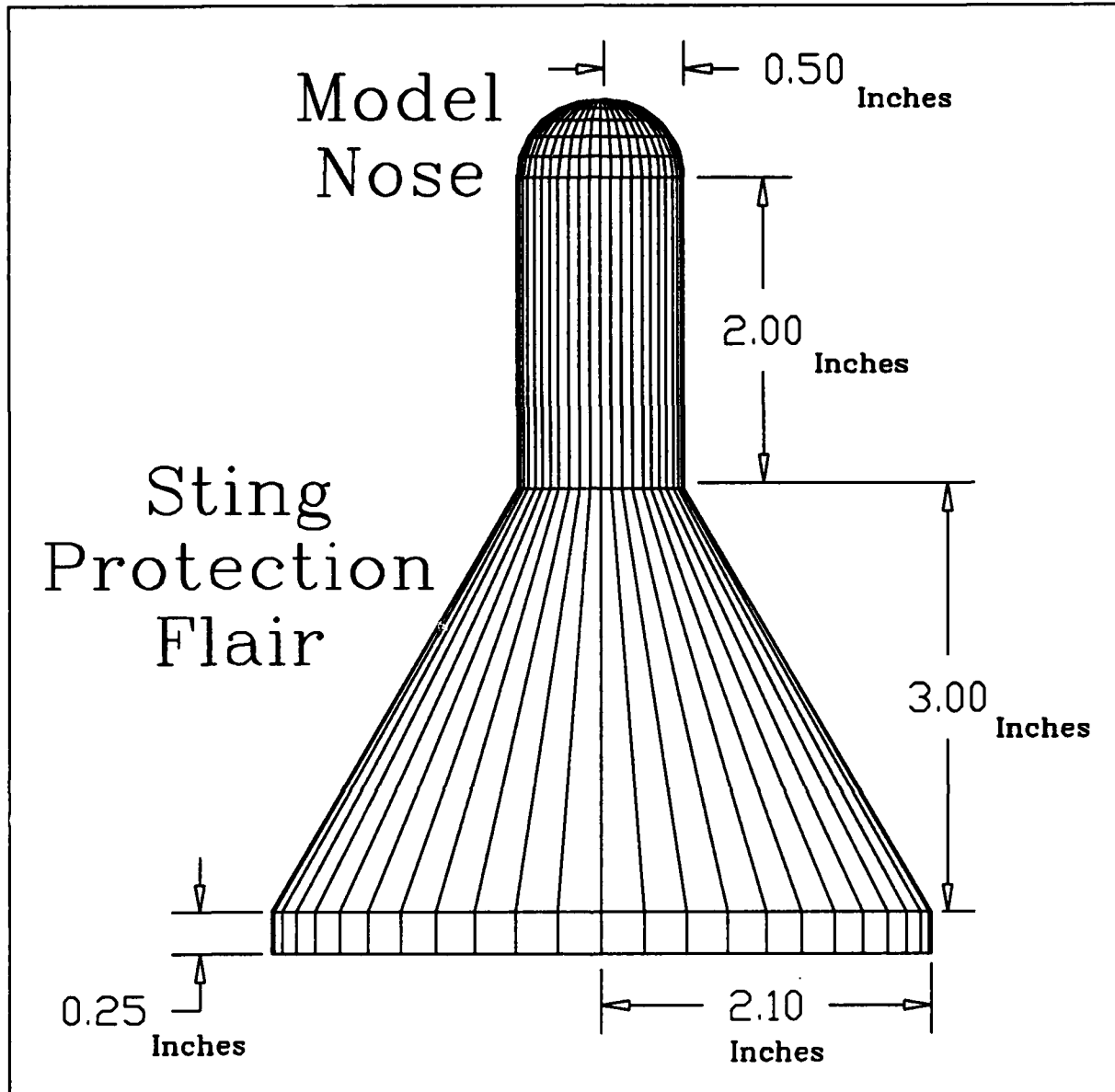
Figure 11 RSI Arc Jet Model

due to heating in the arc jet because of no apparent discoloration or loss of flexibility. Solid quartz and graphite model inserts were cleaned of all attached RTV material prior to post test weighing.

4. Arc Jet Water Matrix Models

LI 900 models were used in a proof of concept test to determine the influence of a water impregnated RSI models in the arc jet flow. Upon pressure reduction, the water freezes to form an ice/RSI matrix.

For this test LI 900 models, prepared the same as before, were immersed in de-aerated deionized distilled water, then degassed at 20 microns Hg vacuum of pressure for ten minutes. After degassing the model, water and container were placed inside a vacuum desiccator. A 20 micron vacuum was applied and remained for 15 minutes or until just prior to model insertion and mounting in the arc jet test chamber.

C.   RECORDING EQUIPMENT

Optical pyrometers were used to approximate the model ablative surface temperature by the apparent brightness of the model while in the arc jet flow. A thermogage pyrometer with a 30 inch focal length and wavelength of 20 microns was mounted inside the test chamber [Fig. 8] and connected to a data acquisition recording computer, which recorded throughout each arc jet test run.

A disappearing wire pyrometer was mounted outside of the test section and viewed the model though a quartz window [Fig. 8]. The manual operation of the disappearing wire pyrometer was conducted throughout each test run with the number of temperature readings depending on the test run length and recessional velocity of the model. Reading the disappearing wire was difficult due to the small model size and the short duration of the tests.

28

V. RESULTS & DATA REDUCTION

A. MOTION PICTURES

High speed motion pictures were taken of most of the arc jet runs and these movies were the primary basis for all linear recessional data. Fine details of the surface ablation process may be seen in the movies regarding the shock layer and shock standoff distance from the model during the ablation process. The lensing effect, however does have an effect on the measurement of the actual versus measured values seen in the movies. This distortional effect was presumed to be constant throughout all model measurements and therefore no compensation was made.

The lensing effect of the shock layer on the model measurements is a documented phenomenon which creates distortional problems when viewing an object surrounded by a three dimensional shock layer. The distortional effects caused by this phenomenon does not allow precise measurement of objects on the other side of the shock layer. The dynamic movements of the model ablative surface cannot be measured without containing these distortional effects, so all linear recession data does contain the lensing distortional effects.

While viewing the high speed movies of the models in the arc jet flow, the dynamic surface shear forces on the ablative surface produces ring waves, which vary in height, wave pattern, and expansion speeds. These ring waves harden and remain intact on the solid quartz models upon removal from the arc jet flow. The other models contained ring waves during the test and could be seen in the movies, but they were not large enough to be evident upon removal from the arc jet flow.

During the arc jet runs the model behaved in one of two modes, remain intact, in which the surface began to ablate and contain melt runoff with no major shape changes during the test run (other than radius change). The other mode was structural failure, the failure of the model was characterized by

29

rapid shape changes during the arc jet run along with large "peeling" sections of the model during the run. Traces of these two model behavior modes are represented in Figure 12 and 13. The analysis of the high speed movies resulted in tracings of each photographed model and are shown in the Appendix.
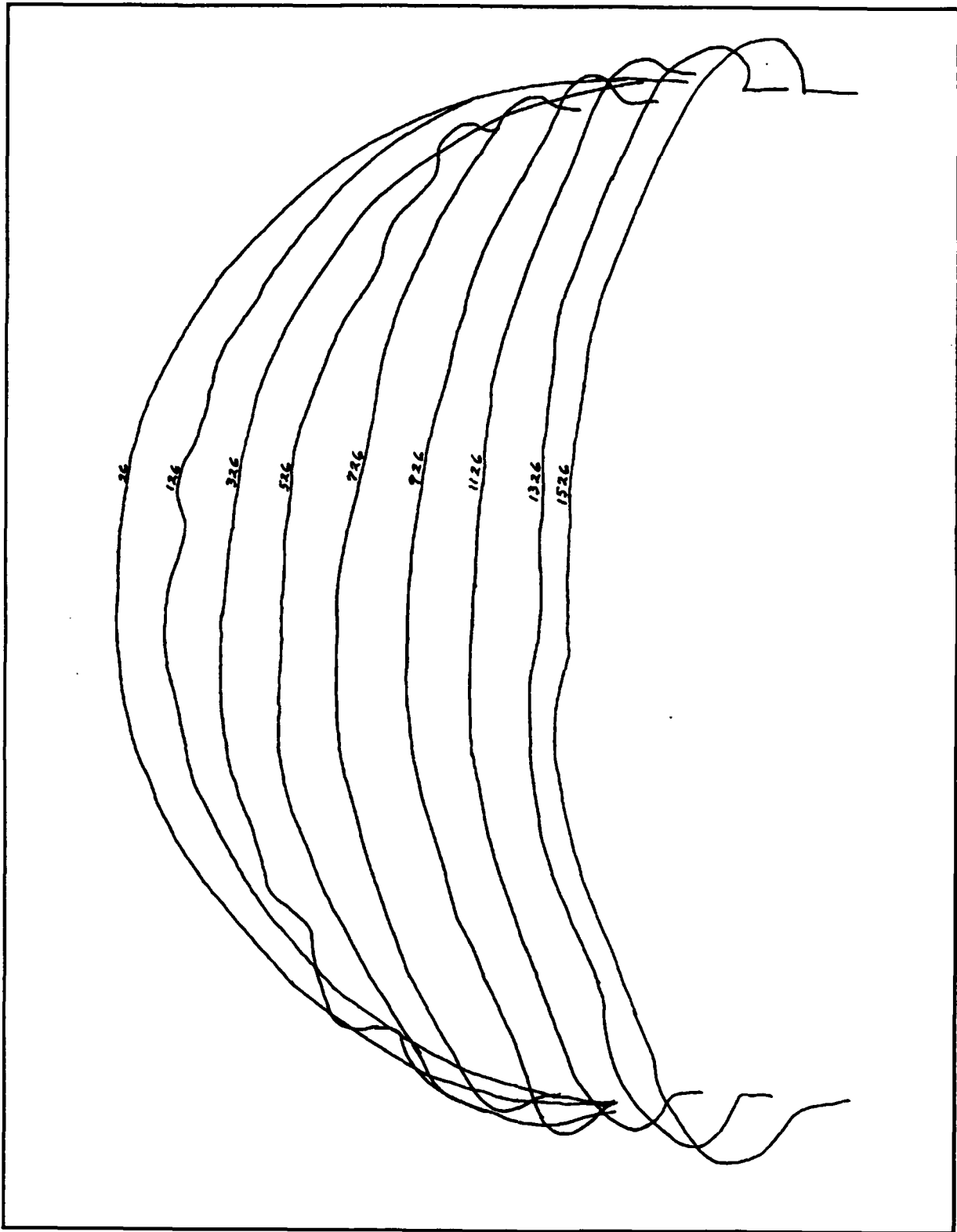
Figure 12 Intact Model Tracing
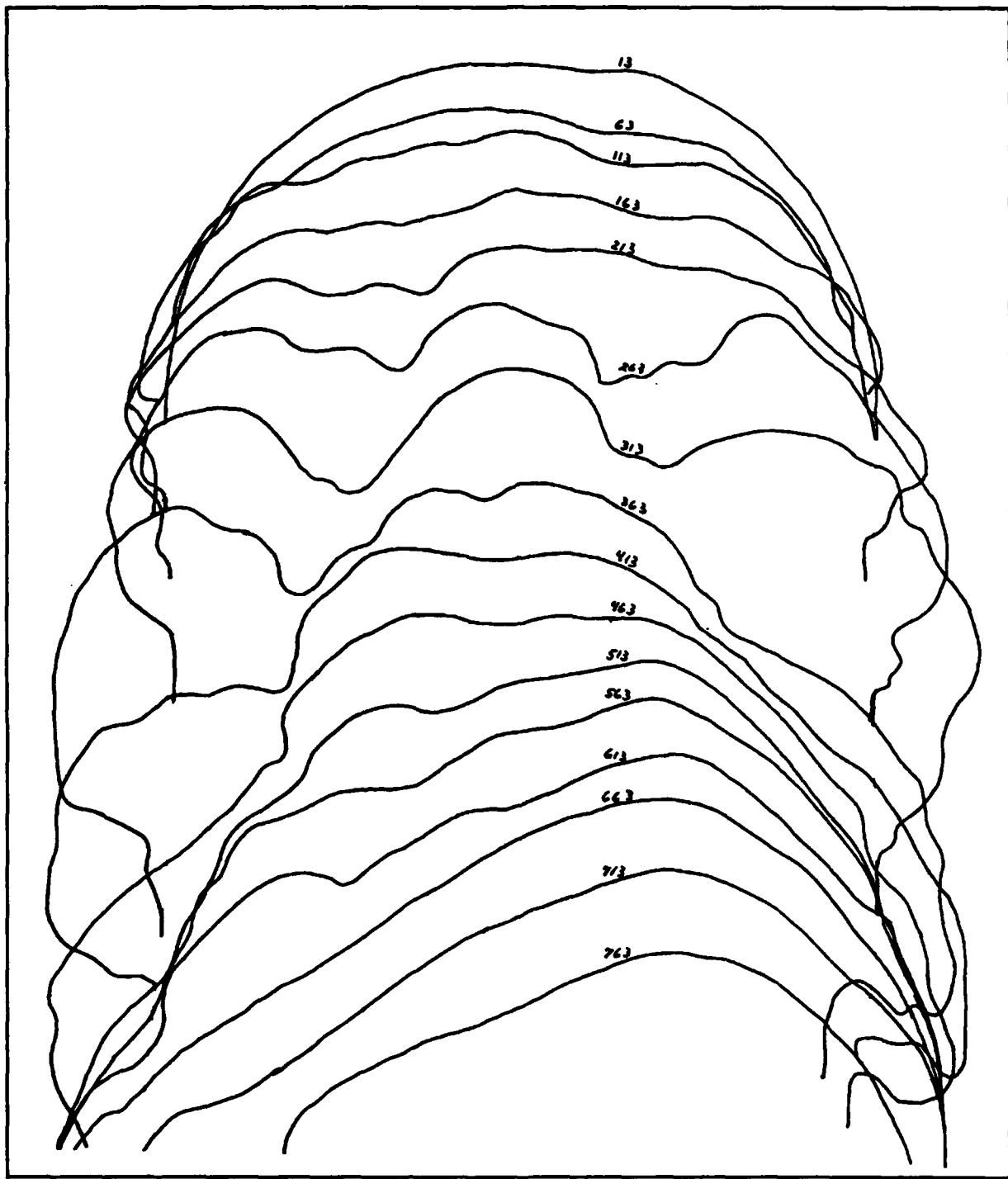
Figure 13 Failed Model Tracing

B.   MASS LOSS

The first estimate for vaporization mass loss calculation was obtained from the weight change of the model before and after the arc jet run. The total mass loss due to melt runoff and vaporization is a function of the total linear recession and material density. The surface recessional velocity of the test model was assumed linear. The data points for each pressure and material were fit to a linear regression as seen in Figures 17 though 28. From the calculations and measurements a summary chart of all test runs is shown in Figure 14.

C.   RECESSION RATES

From the tracings of the high speed movies, the recessional rates were determined assuming a linear fit of the data points. The pressure effects upon the recession rates of each material can be clearly seen in Figure 20,27, and 28. These pressure effects have an abrupt discontinuity around .330 atmospheres stagnation pressure.

D.   MASS LOSS RATES

As discussed earlier the preliminary mass loss rates were determined as a function of total recession and time. This value was used in the c..rgy balance equation [Eq. 26], with iterative solutions calculated by a computer code [Appendix]. These solutions for vaporization and melt runoff mass loss rates are shown in Figure 29 through 40, along with the actual measured experimental mass loss and experimental error tolerance regions.

E.   GRAPHITE SURFACE TEMPERATURES

Experimentally measured surface temperature readings are shown in Figure 41 through 45 as compared to computer generated surface temperature profiles [Ref. 4].

60 MEGAWATT ARC JET TEST RESULTS

Run	Model	Date	Run Time	Wt Init	Wt Final	Wt Diff	Wt Rate	Rec Total Rate	Rec Rate	Amp	Volt	Pressure Stag	Chbr	Dwir	Noz Dst	Str	Heat Flux	Vol	M	Total Enth
1	Q01	5/9	30	106.72	106.10	0.62	.021	.005	0.08	5000	3210	.085	32.5	1905	7.7	I	830	25720	10.0	22500
2	Q02	5/9	30	106.86	104.05*	2.81*	.094*	.011	0.29	6000	7250	.330	124.3	2160	7.7	I	1420	24500	9.2	21000
3	LI2203	5/8	30	112.01	110.90	1.11	.037	.015	0.43	5000	3400	.085	32.7	2160	7.7	I	830	25720	10.0	22500
4	Q03	5/10	20	106.48	103.47	3.01	.151	.009	0.16	6000	7000	.440	121.0	2000	3.0	I	1000	24500	8.9	21750
5	—5/15—————ABORTED———																			
6	LI2202	5/16	20	109.44	100.98	8.46	.423	.066	1.31	6000	7250	.440	123.0	———	3.0	I	1000	24500	8.9	21750
7	LI2201	5/16	15	124.28	116.76	7.52	.537	.111	1.48	6010	7240	.440	122.8	2200	3.0	F	1000	24500	8.9	21750
8	LI8902	5/17	8	76.47	75.89	0.58	.064	.241	2.05	5020	3900	.085	32.4	2200	7.7	F	830	25720	10.0	22500
9	LI0901	5/17	8	51.33	50.43	0.90	.090	.241	2.24	5020	3450	.085	34.5	2295	7.7	F	830	25720	10.0	22500
10	LI2204	5/18	30	127.38	125.64	1.78	.059	.021	0.66	5020	4630	.144	53.4	2200	.7.7	I	1027	25290	10.0	22500
11	—5/21—————ABORTED———																			
12	LI2205	5/21	15	120.01	115.14	4.87	.325	.089	1.26	6010	7230	.330	113.4	2300	7.7	F	1420	24500	9.2	21000
13	LI2206	5/22	15	122.87	118.00	4.87	.271	.111	1.19	6040	7290	.440	122.7	2200	3.0	F	1000	24500	8.9	21750
14	—5/29—————ABORTED———																			
15																				
16	LI2207	6/6	30	128.32	126.82	1.50	.050	.023	0.89	2500	6000	.184	71.3	2200	7.7	F	891	21820	8.4	18000
17	LI0904	6/6	6	72.40	71.92	0.48	.096	.241	2.00	5000	4600	.065	56.0	———	20.7	F	830	25720	10.0	22500
18	LI2208	6/6	30	116.73	115.64	1.09	.036	.015	0.45	5000	4500	.085	52.8	2200	20.7	I	830	25720	10.0	22500
19	LI2209	6/11	30	123.78	121.88	1.90	.063	.027	0.90	2700	6000	.250	82.0	———	5.5	F	1070	21740	8.1	18000
20	LI2210T	6/13	30	—	—	—	—	—	—	5000	3450	.085	82.0	2150	7.7	F	830	25720	10.0	22500
21	LI0909T	6/13	10	—	—	—	—	—	—	5000	3450	.085	31.0	2100	7.7	F	830	25720	10.0	22500
22	G01	6/15	30	86.10	85.34	0.76	.025	.006	0.06	5000	3450	.085	32.2	2560	7.7	I	830	25720	10.0	22500
23	G02	6/15	30	86.23	84.21	2.02	.067	.003	0.06	6000	7300	.330	122.5	2740	7.7	I	1420	24500	9.2	21000
24	G04	6/15	30	86.02	84.87	1.15	.038	.002	0.03	5000	4650	.144	55.0	2630	7.7	I	1027	25290	10.0	22500
25	LI0906W	6/15	10	72.37	72.22*	0.15*	.015*	.015	0.07	5020	3400	.085	32.1	2000	7.7	I	830	25720	10.0	22500
26	LI0903W	6/18	20	71.34	70.78*	0.56*	.028*	.026	0.46	5000	4600	.144	54.6	2270	7.7	I	1027	25290	10.0	22500
27	LI0907W	6/18	20	74.94	73.66*	1.28*	.064*	.045	0.82	6000	7270	.330	122.7	2240	7.7	I	1420	24500	9.2	21000
28	LI1802	6/19	30	—	—	—	—	.022	0.06	5000	3400	.085	31.1	2200	7.7	I	830	25720	10.0	22500
29	LI1801	6/19	7	—	—	—	—	.159	2.00	6000	7600	.330	123.0	2360	7.7	F	1420	24500	9.2	21000
30	G03	8/19	30	85.87	83.56	2.31	.077	.004	0.08	6000	7700	.440	121.0	3250	3.0	I	1000	24500	8.9	21750
UNITS		Sec	grams	grams	g/s	Inch	In/s	Amps	Volt	Atm	Psia	K	Inch				Btu ft/s ft^2s			Btu Lbm

F=Model Structure Failure
I=Model Structure Intact
*=Possible Invalid Data Due to Model Breakage or Melt Loss

Figure 14 Data Summary Chart

```
                              RECESSION -VS- TIME
                                   TIME (sec)
RUN  1    2    3    4    5    6    7    8    9   10   11   12   13   14   15   16   17   18   19   20   21   22   23   24   25   26   27   28   29   30
1         .048
2                        .101 .663      .048      .153 .091           .128           .016      .827           .235                .059           .086
3              .021                                                   .266           .143      .182           .339           .268                .298
                                             .095                              .159                                                    .397           .423
                                                                                                 .276                                         .562
4    ------------------------------ ABORTED ------------------------------
5    ------------------------------ NO FILM ------------------------------
6    ------------------------------------------------------------------------
7    .116 .243 .476 .677 .825 .9631 .051 .181 .181 .251 .311 .361 .421 .49 /-------------------------------------
8    .126 .384 .631 .8241 .871 .271 .47 /----------------------------------------------------------------------
9    .126 .351 .631 .8181 .181 .371 .59 /----------------------------------------------------------------------
10   .055 .094 .149 .193 .226 .276 .309 .348 .397 .447 .475 .524 .563 .602 /-
11   ------------------------------ ABORTED ------------------------------
12   .071 .110 .192 .264 .373 .489 .525 .714 .791 .867 .9281 .867 .061 .071 .171 .38 /---
13   .094 .161 .278 .394 .488 .577 .705 .794 .871 .944 .9931 .051 .121 .19
14   ------------------------------ ABORTED ------------------------------
15   ------------------------------ ABORTED ------------------------------
16   .016 .032 .058 .096 .111 .127 .148 .160 .196 .222 .238 .278 .286 .302 .328 .360 .381 .391 .413 .439 .466 .487 .513 .550 .571 .587 .614 .645 .582
17   .271 .514 .8121 .071 .30 /----------------------------------------------------------------------
18   .027 .068 .092 .124 .157 .189 .222 .281 .308 .330 .346 .384 .411 .438 /-
19   .068 .118 .100 .243 .299 .344 .395 .451 .502 .570 .897
20   ------------------------------ NO TRACE THERMOCOUPLE ------------------------------
21   ------------------------------ NO TRACE THERMOCOUPLE ------------------------------
22   ------------------------------------------------------.01-------.011-------------------------------------.065
23                                                                                                                          .054
24                                                                                                                          .027
25   .056 .011 .039 .072 /---
26   .083 .094 .150 .216 .255 .305 .361 .411 .466 .505 .546 .597 .623 .659 /-
27   .088 .178 .272 .366 .455 .533 .622 .716 .810 .469
28   .149 .191 .242 .314 .361 .381 .433
29   .124 .339 .664 1.06 /--                                                                                                         .074
30   .016                                                                                                                                       .38
     1    2    3    4    5    6    7    8    9   10   11   12   13   14   15   16   17   18   19   20   21   22   23   24   25   26   27   28   29   30
```
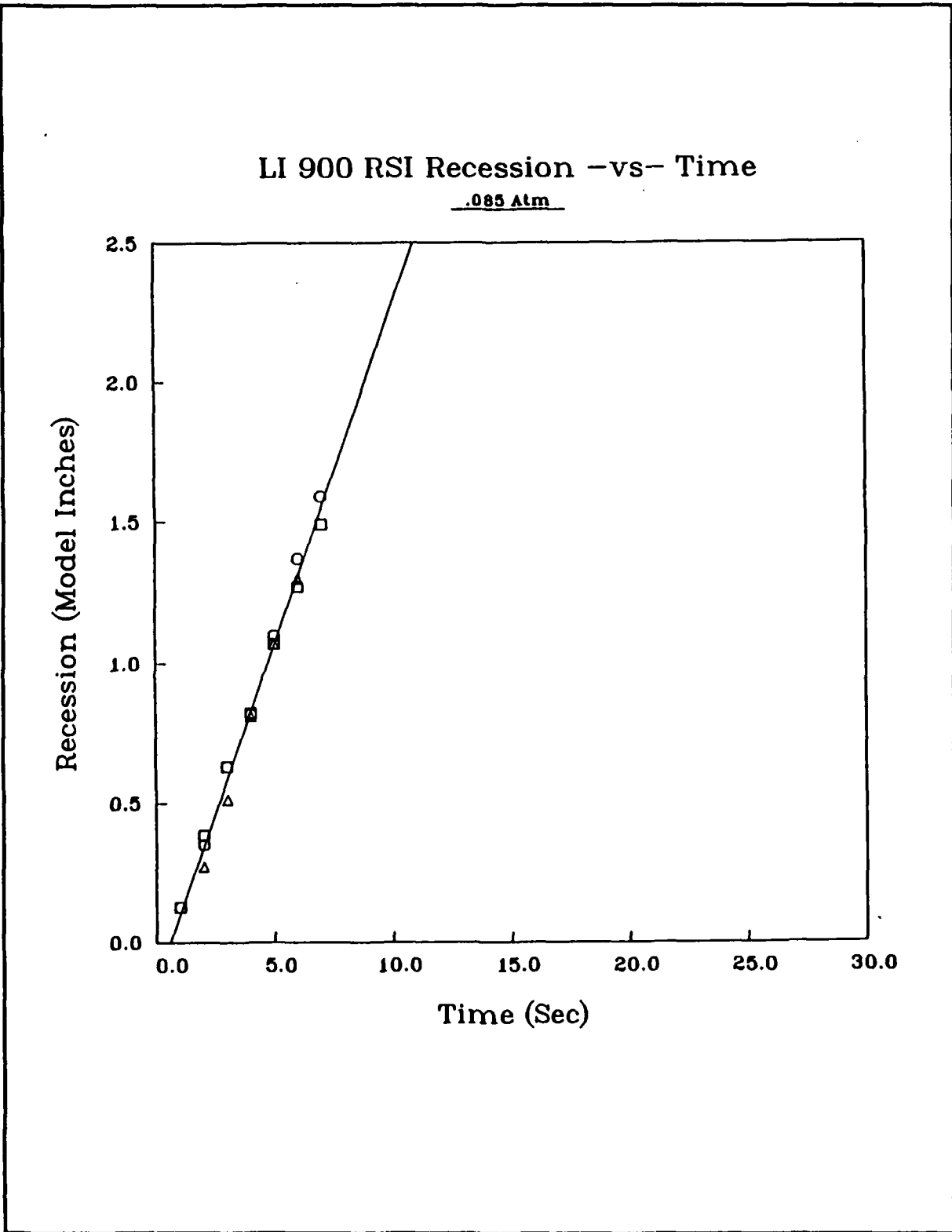
Figure 15 Recession -vs- Time Summary Chart

35

MODEL NOSE RADIUS VERSUS TIME
TIME (sec)

Figure 16 Nose Radius -vs- Time Summary Chart

LI 900 RSI Recession −vs− Time

.085 Atm

Figure 17 LI 900 Recession
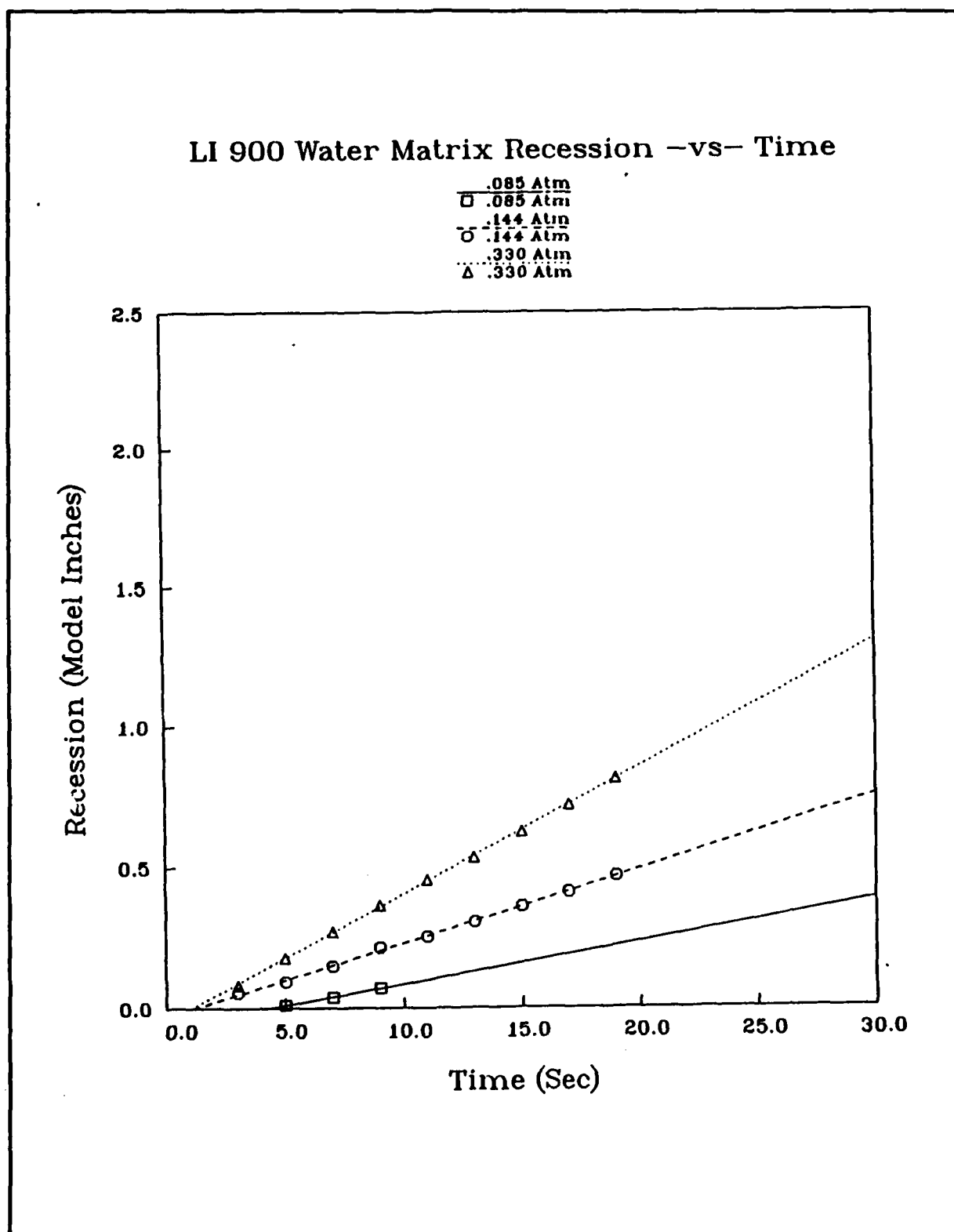
Figure 18 LI 900 Water Matrix Recession
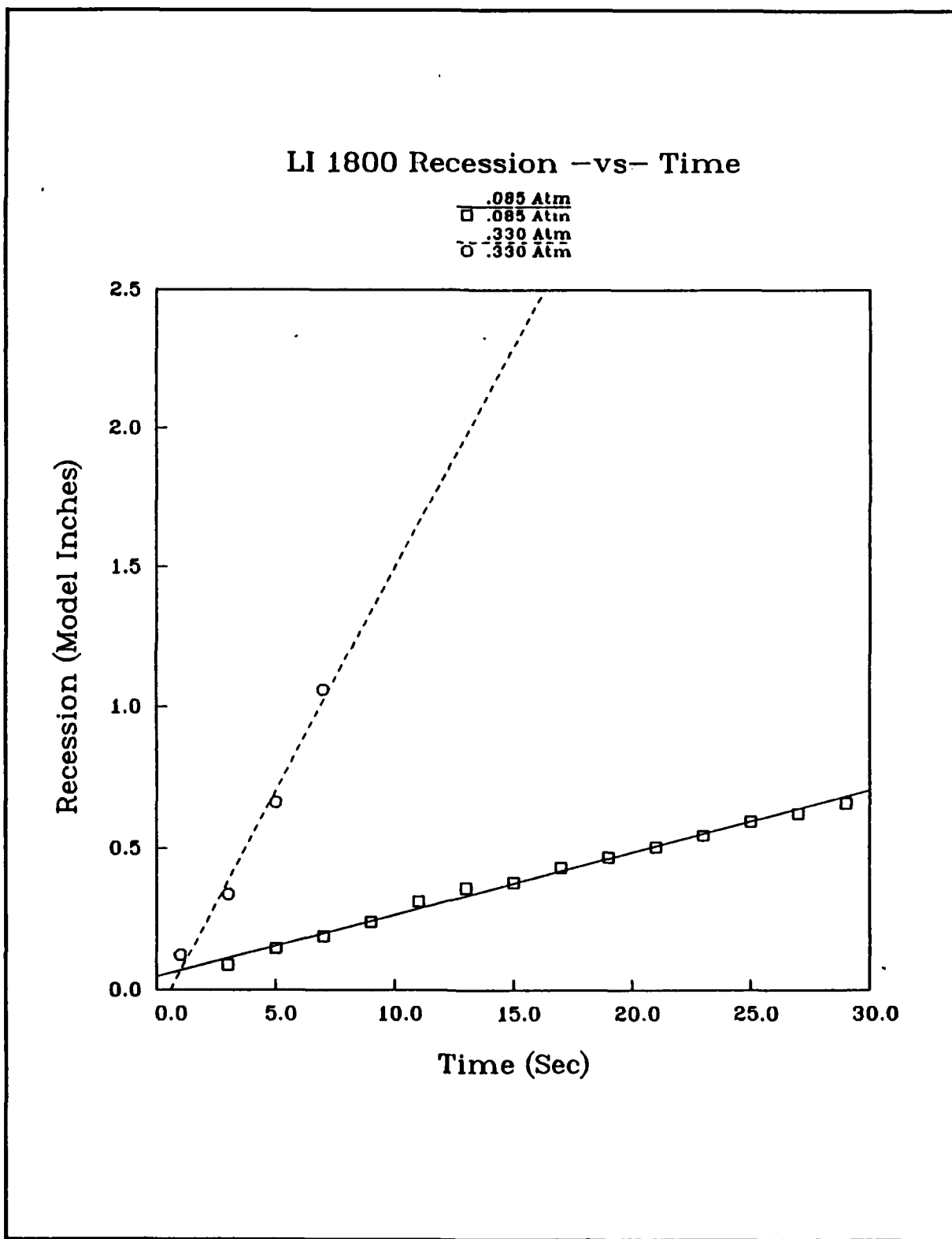
Figure 19 LI 1800 Recession
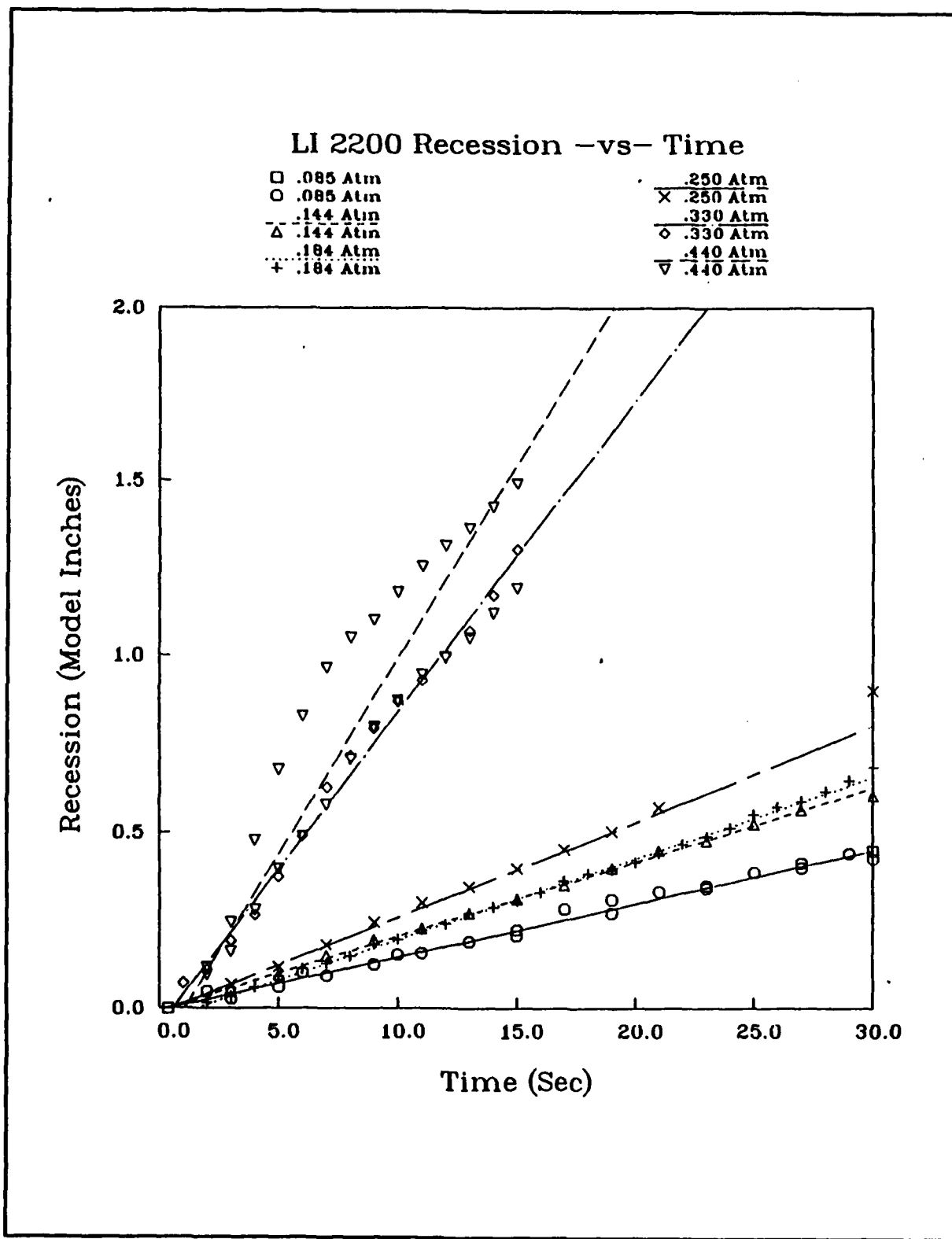
Figure 20 LI 2200 Recession

40

LI 2200 Recession —vs— Time
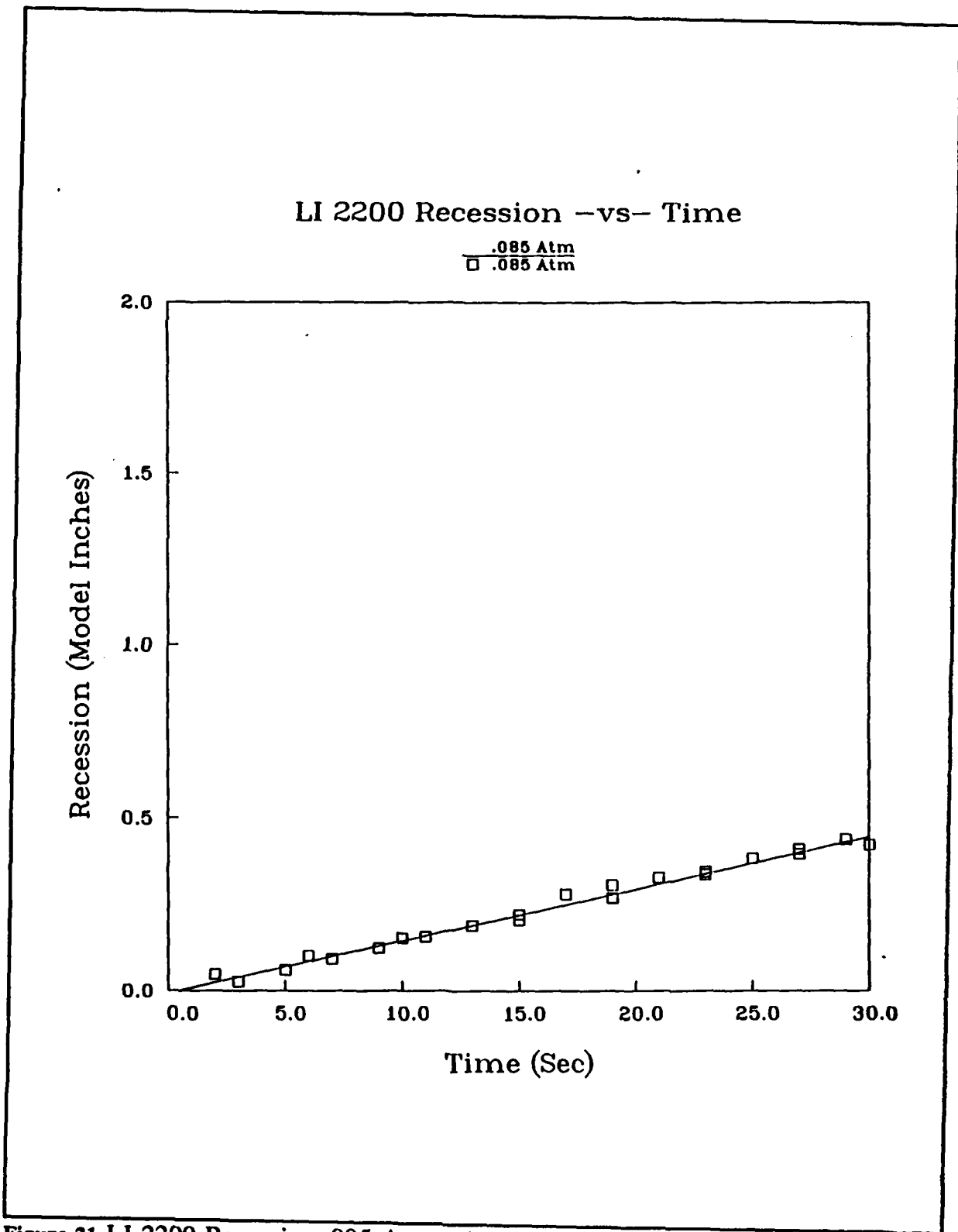
.085 Atm
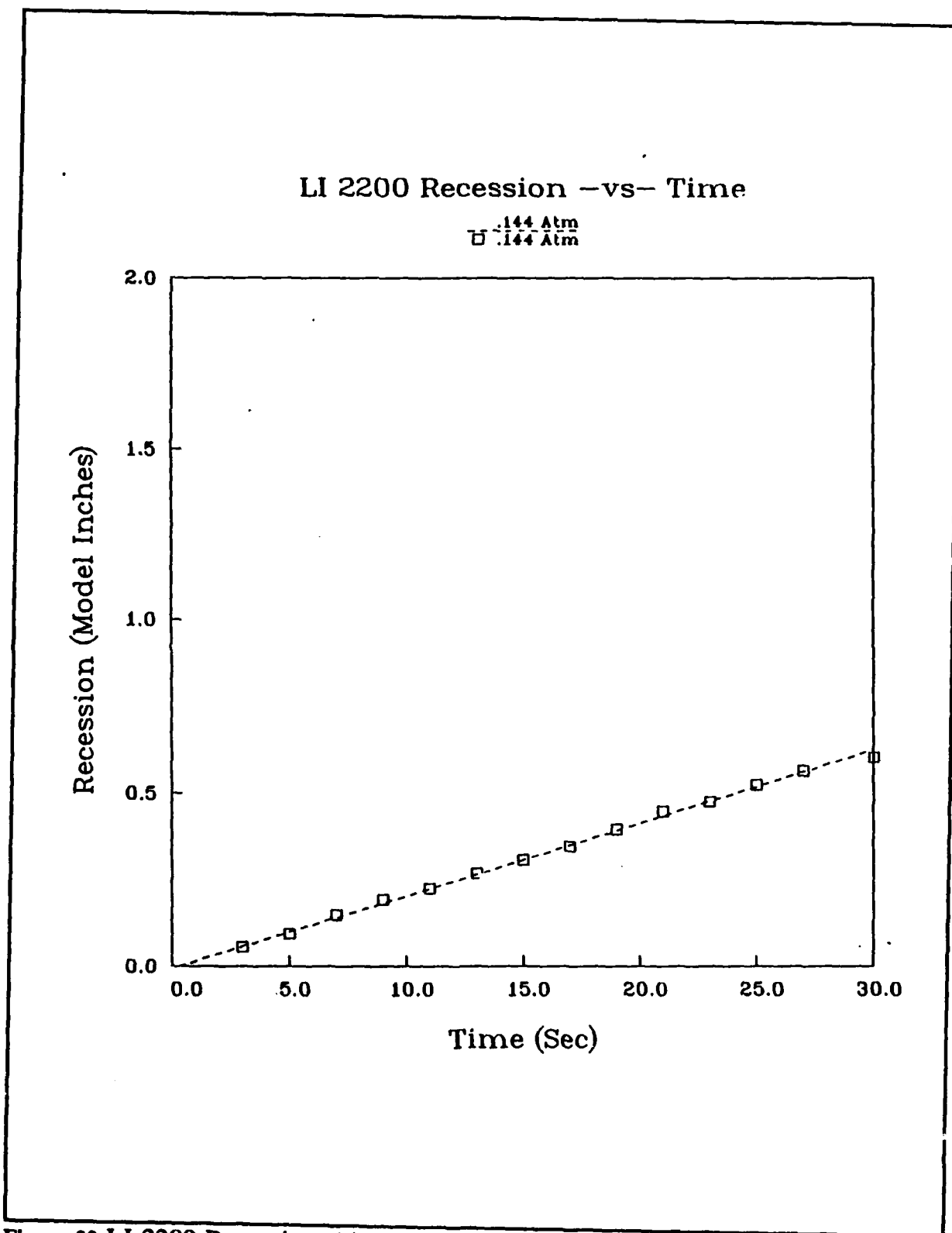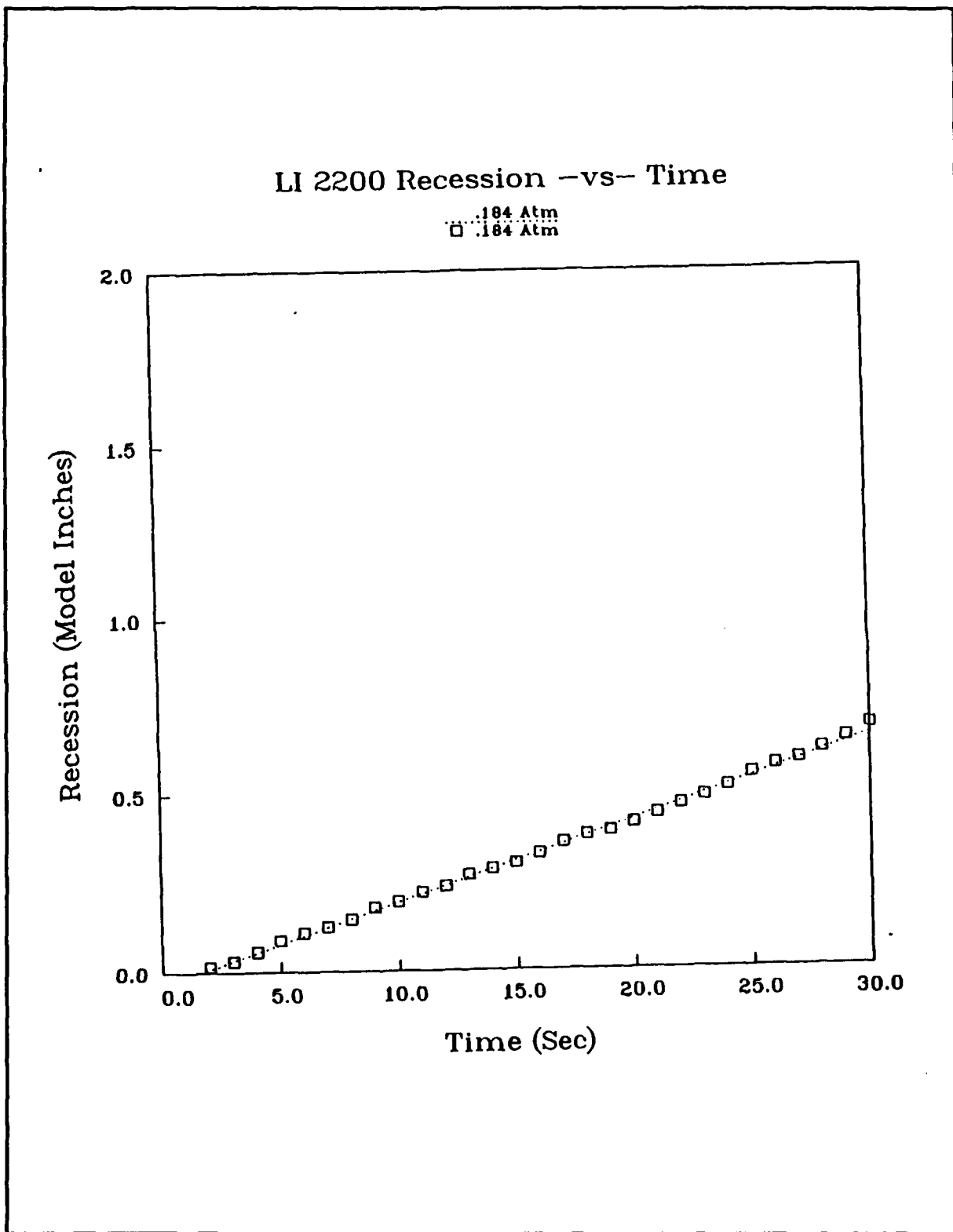□ .085 Atm

Figure 21 LI 2200 Recession .085 Atmospheres

41

Figure 22 LI 2200 Recession .144 Atmospheres

42

Figure 23 LI 2200 Recession .184 Atmospheres

LI 2200 Recession −vs− Time
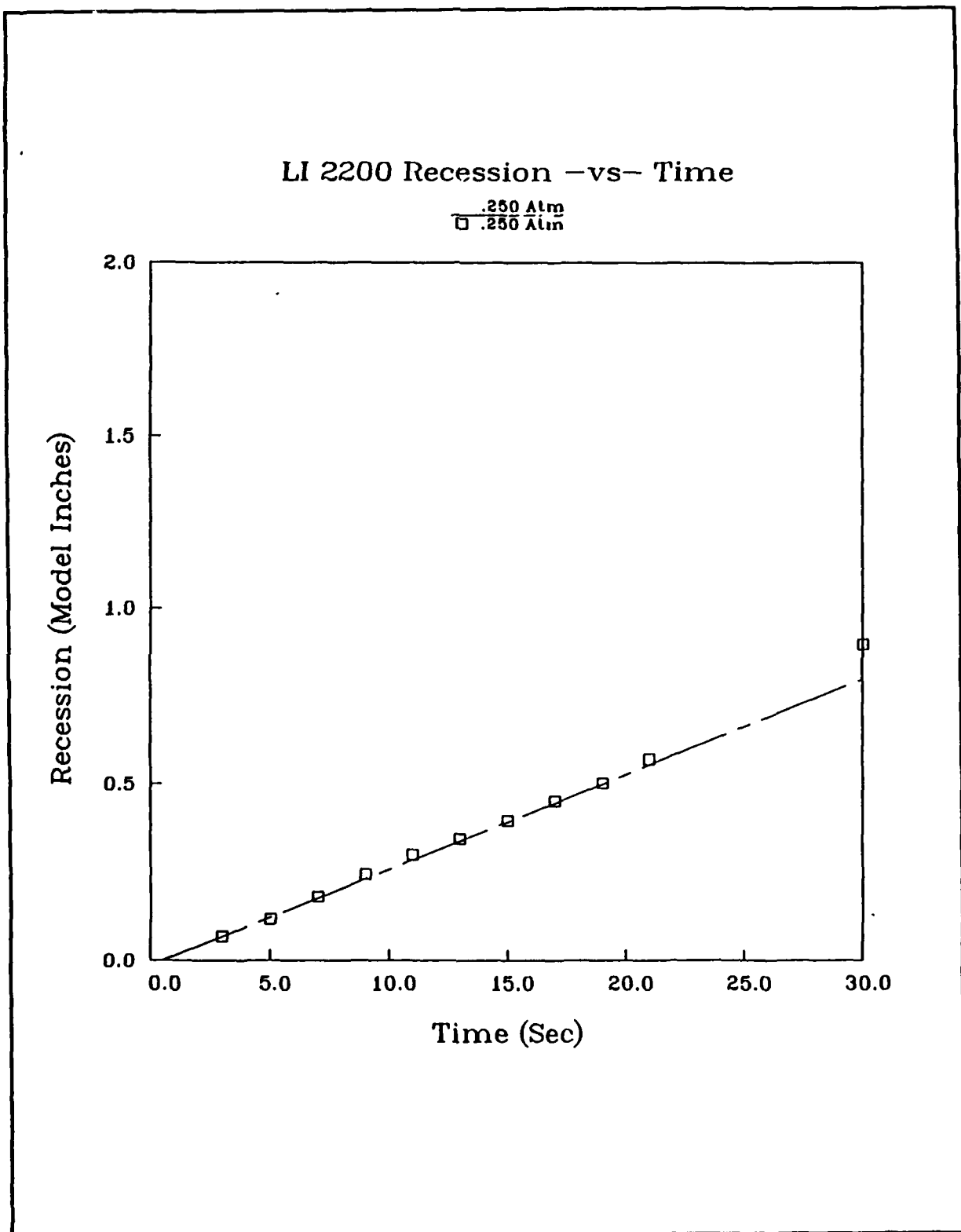
.250 Atm
.250 Atm

Figure 24 LI 2200 Recession .250 Atmospheres
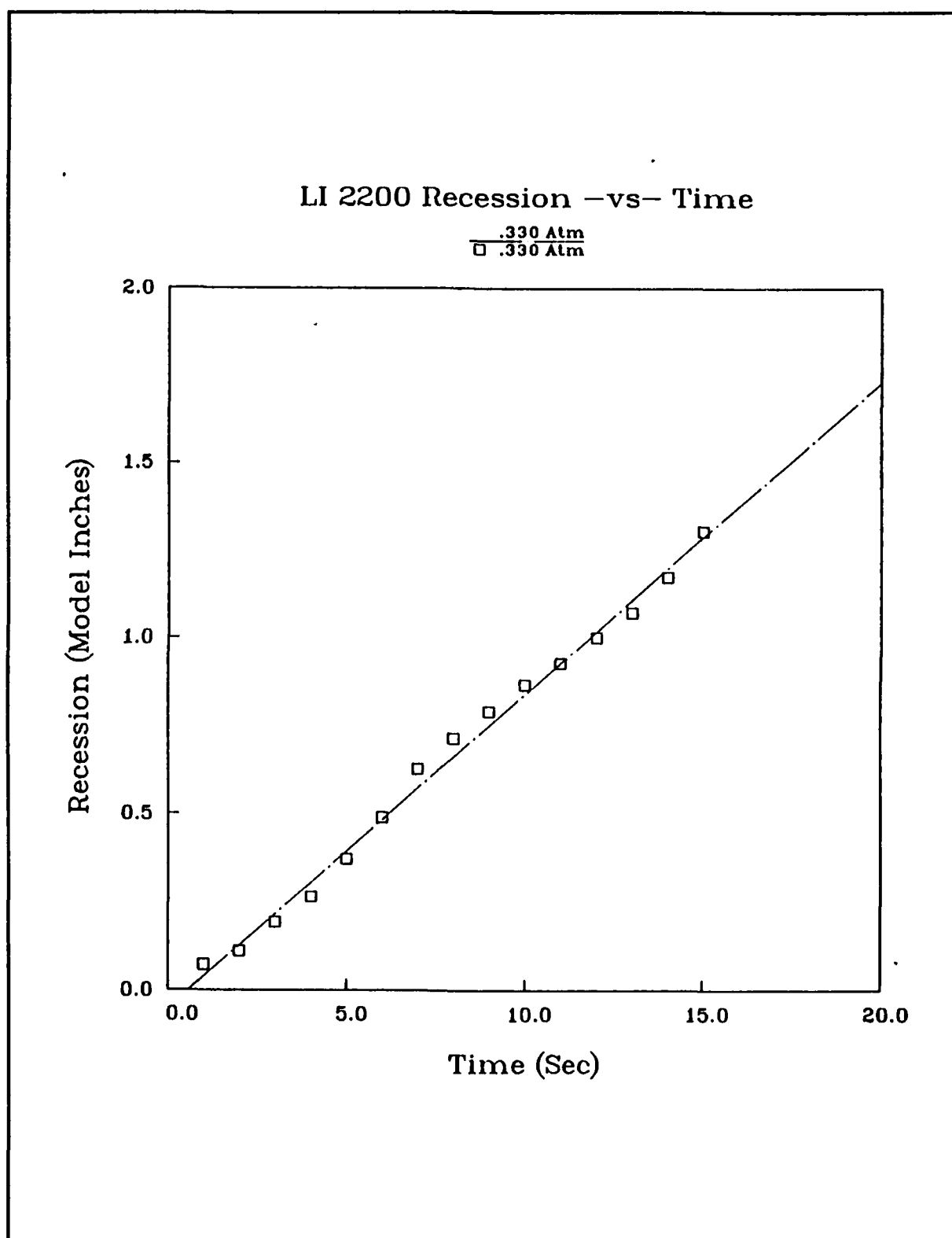
Figure 25 LI 2200 Recession .330 Atmospheres

LI 2200 Recession −vs− Time
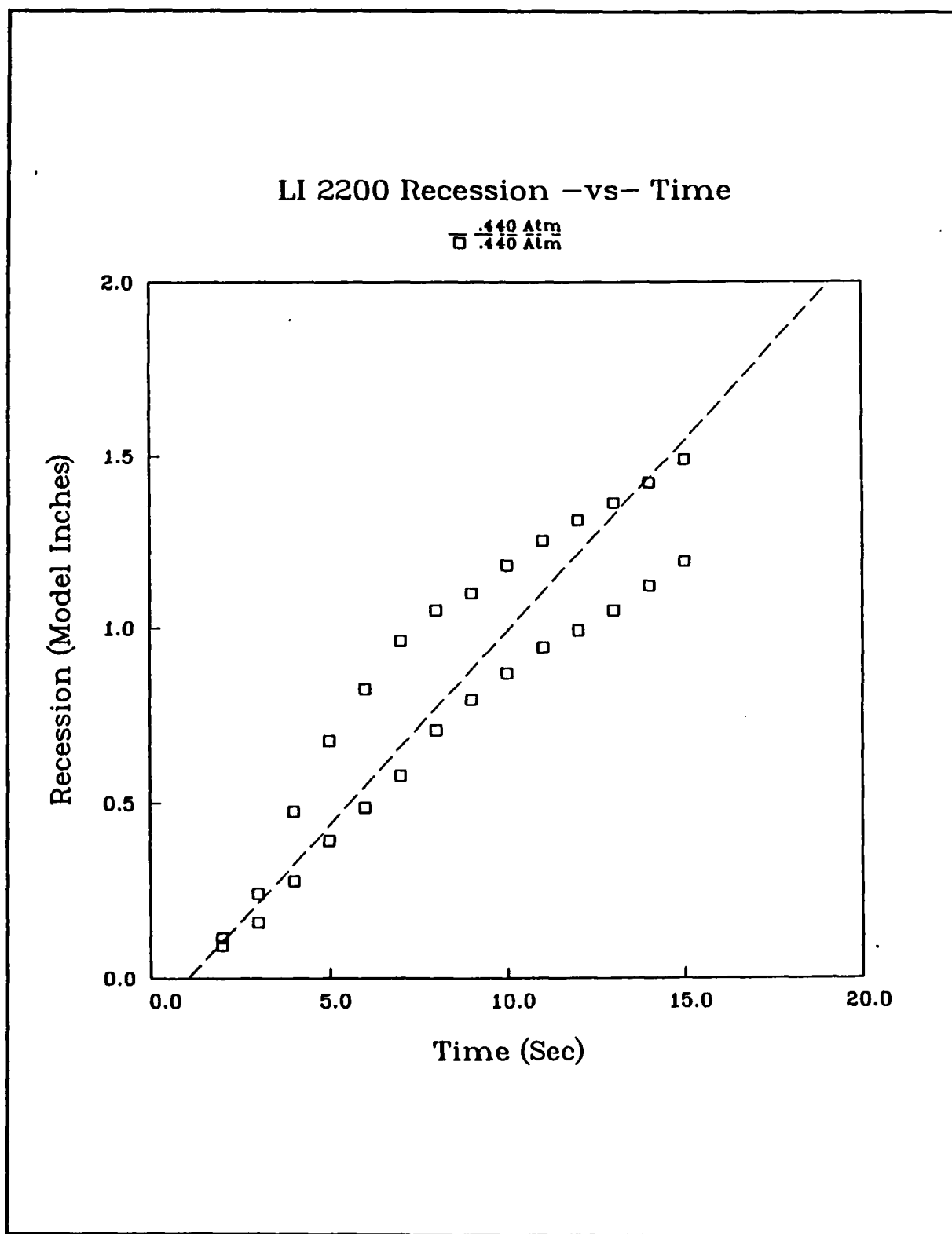
Figure 26 LI 2200 Recession .440 Atmospheres

46

Figure 27 Solid Quartz Recession

47

Figure 28 Solid Graphite Recession

48
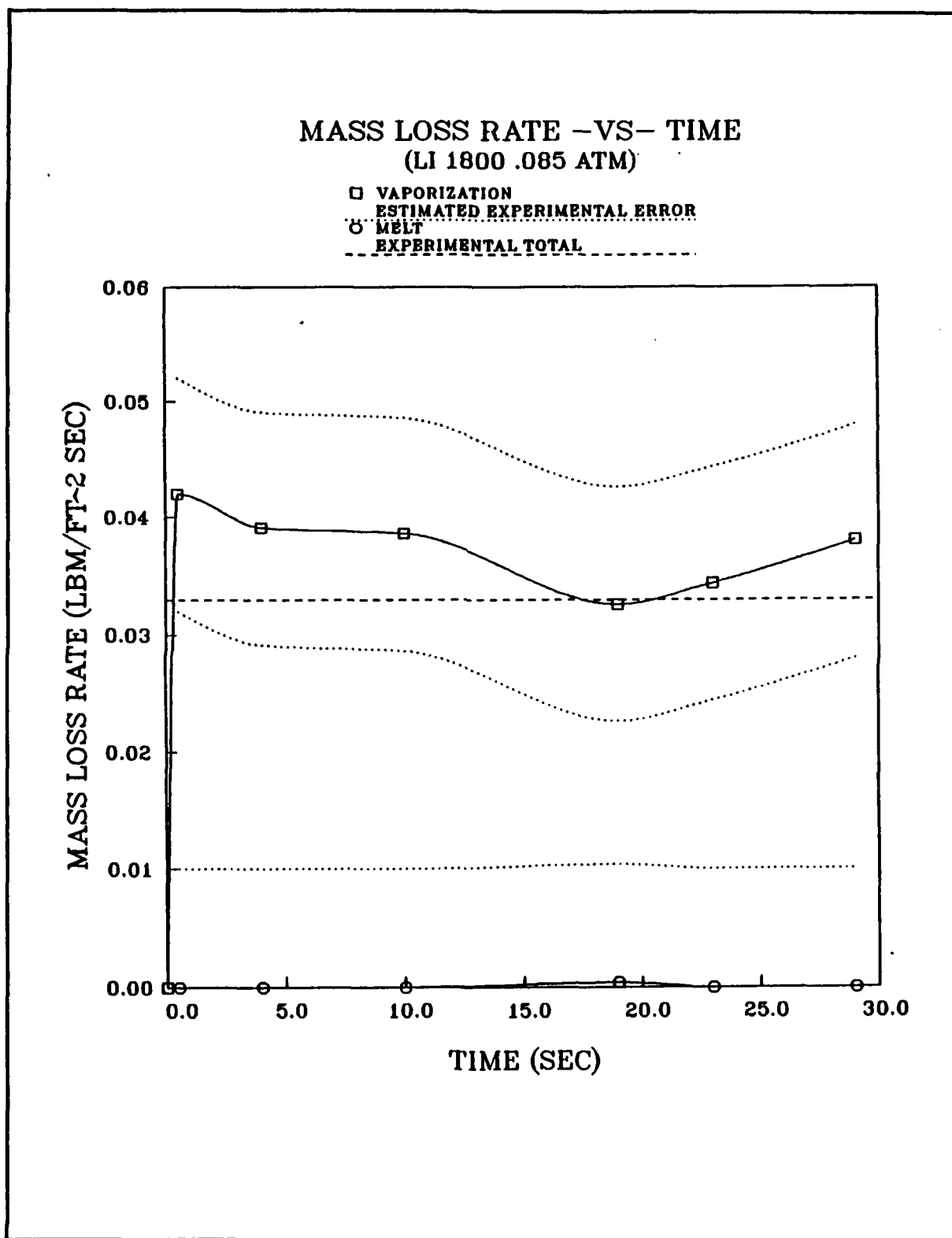
Figure 29 LI 1800 Mass Loss Rate .085 Atmospheres
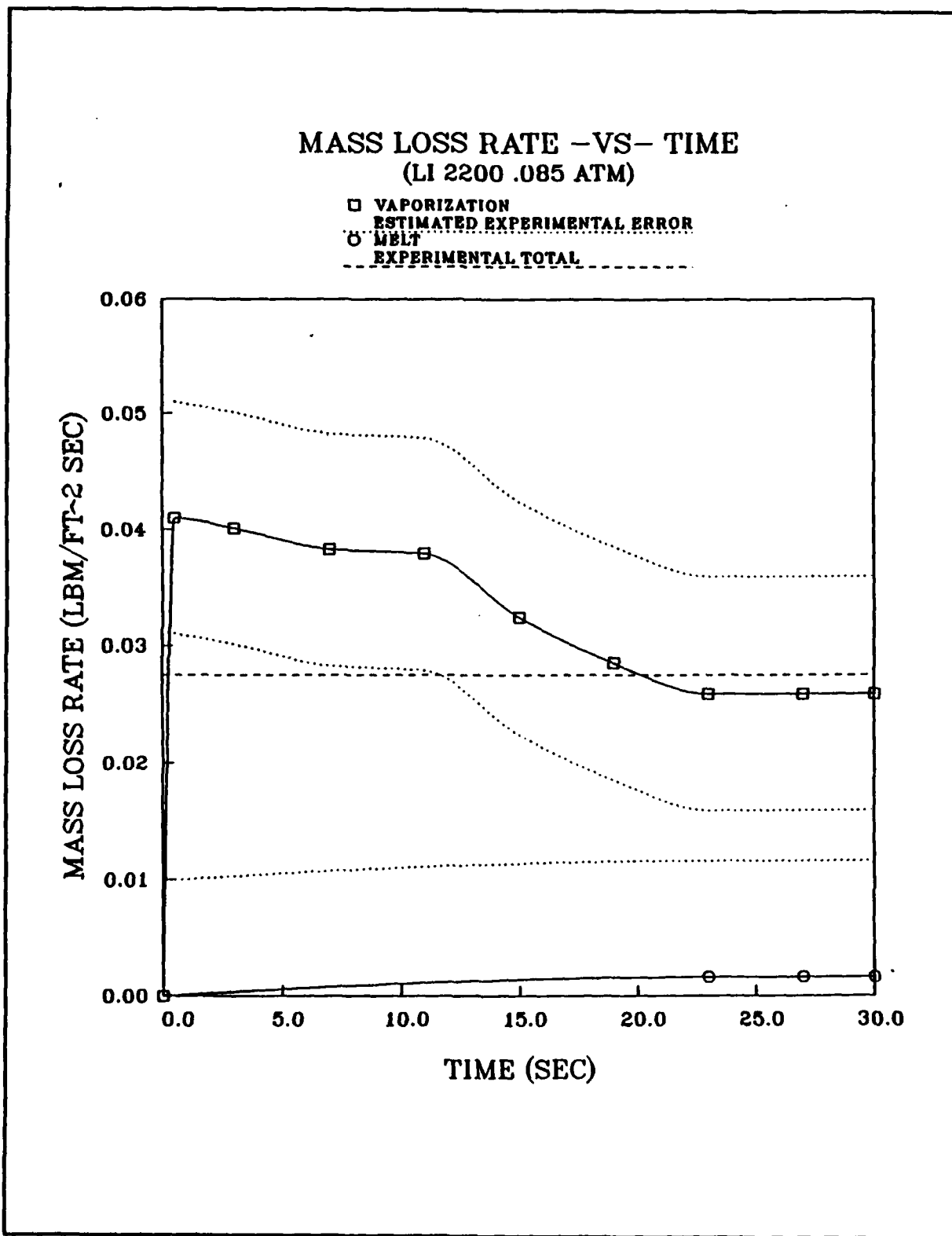
Figure 30 LI 2200 Mass Loss Rate .085 Atmospheres

50

MASS LOSS RATE –VS– TIME
(LI 2200 .144 ATM)

□ VAPORIZATION
ESTIMATED EXPERIMENTAL ERROR
Ö MELT
EXPERIMENTAL TOTAL
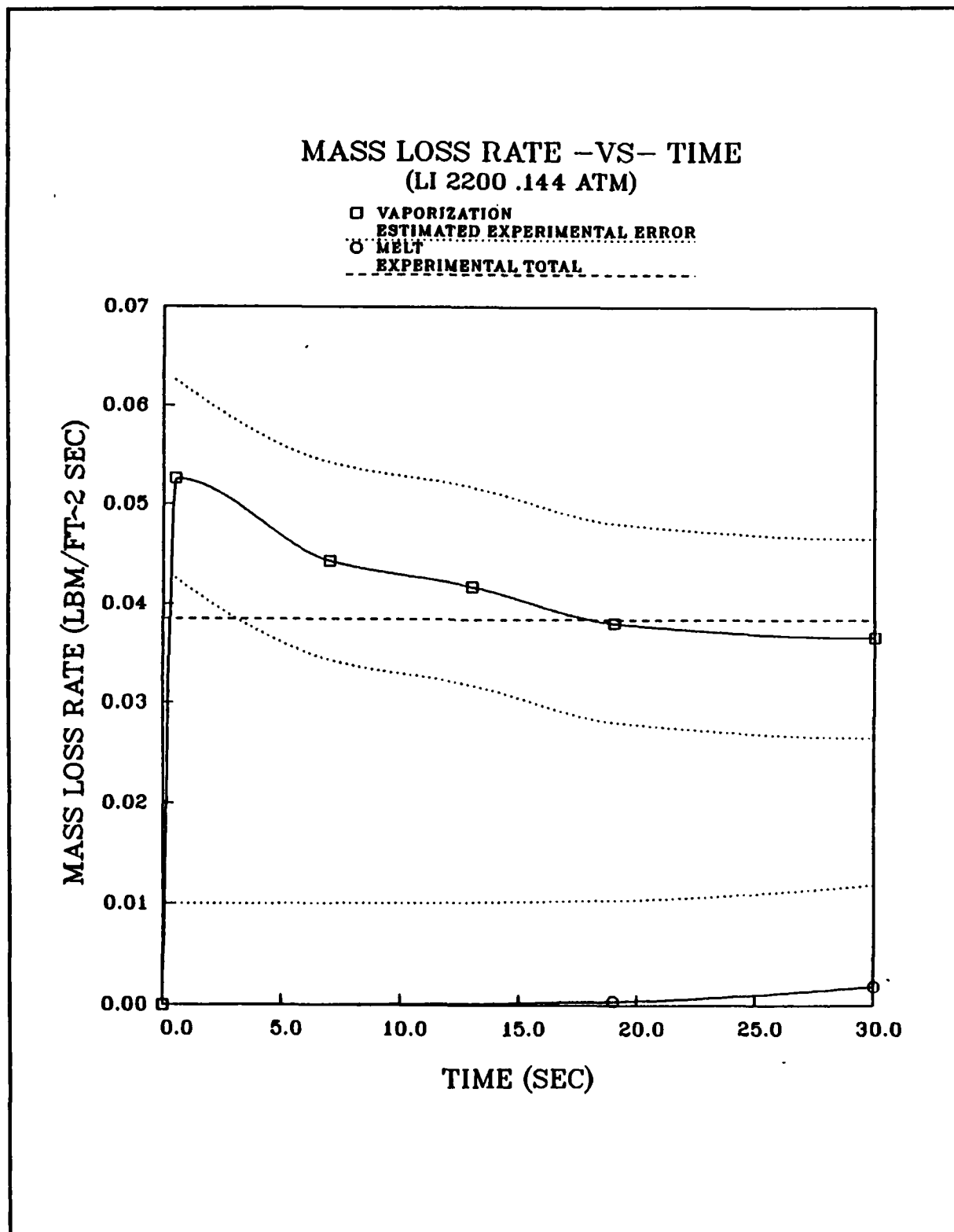
Figure 31 LI 2200 Mass Loss Rate .144 Atmospheres

51
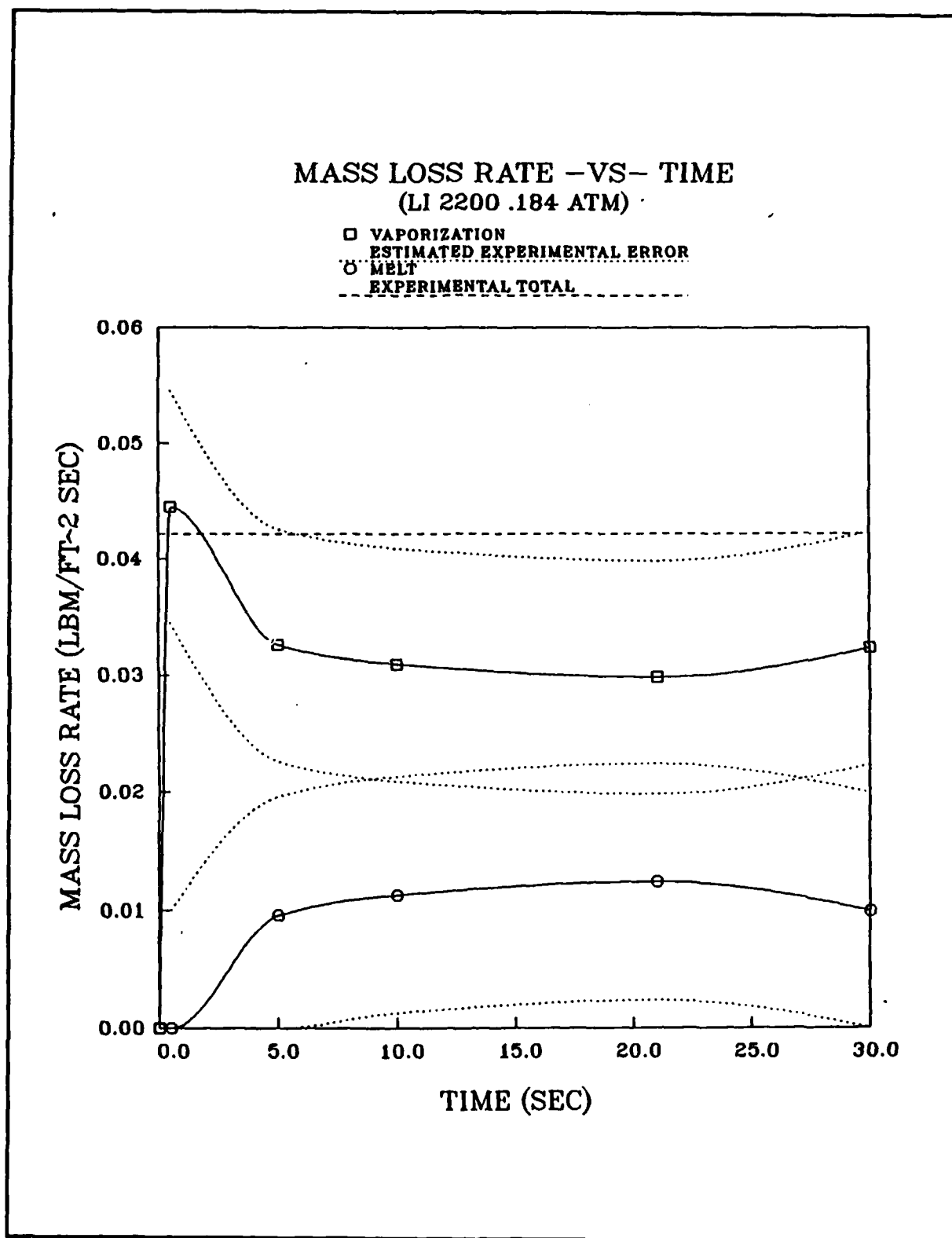
Figure 32 LI 2200 Mass Loss Rate .184 Atmospheres
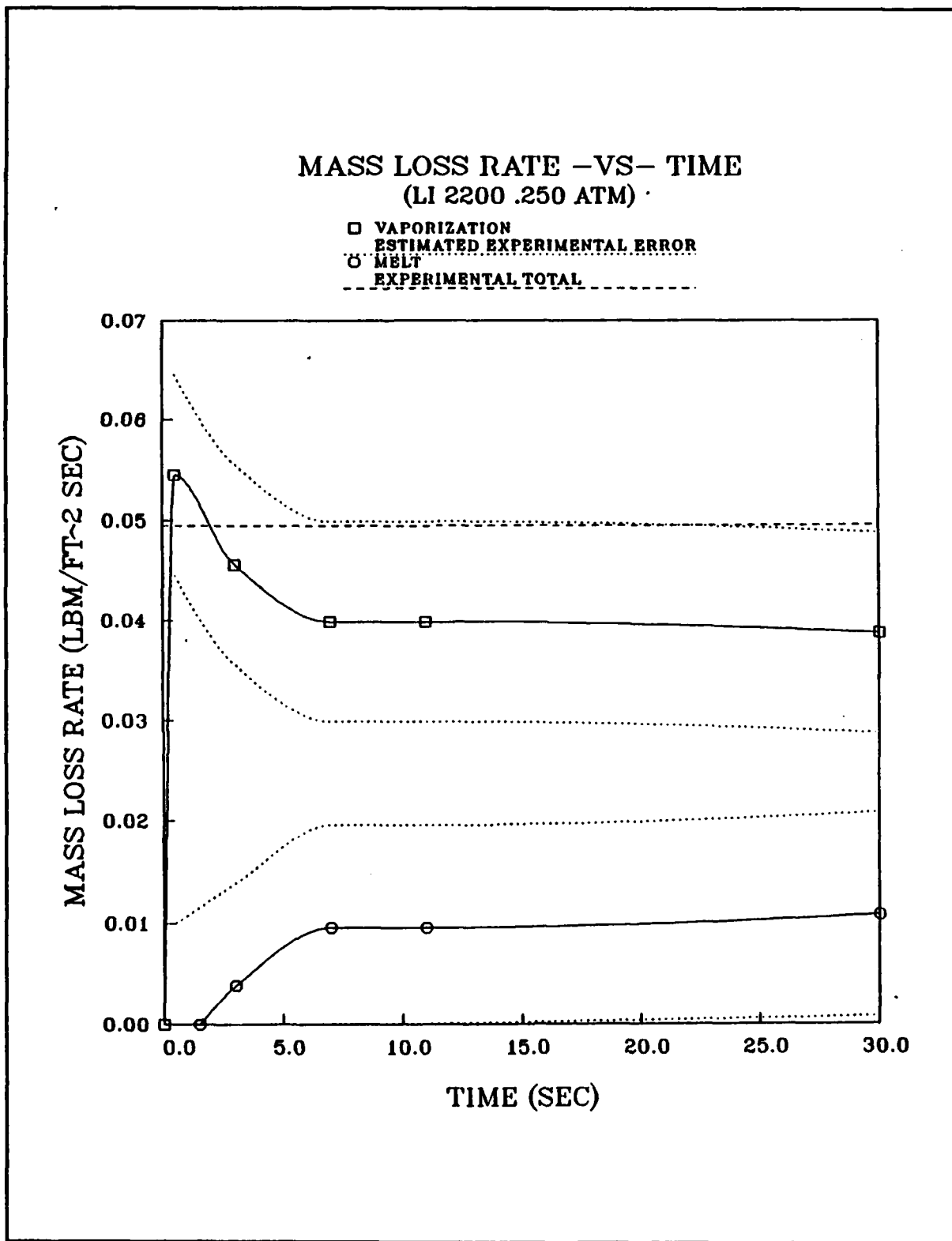
Figure 33 LI 2200 Mass Loss Rate .250 Atmospheres

MASS LOSS RATE —VS— TIME
(LI 2200 .330 ATM)

□ VAPORIZATION
ESTIMATED EXPERIMENTAL ERROR
O MB
EXPERIMENTAL TOTAL
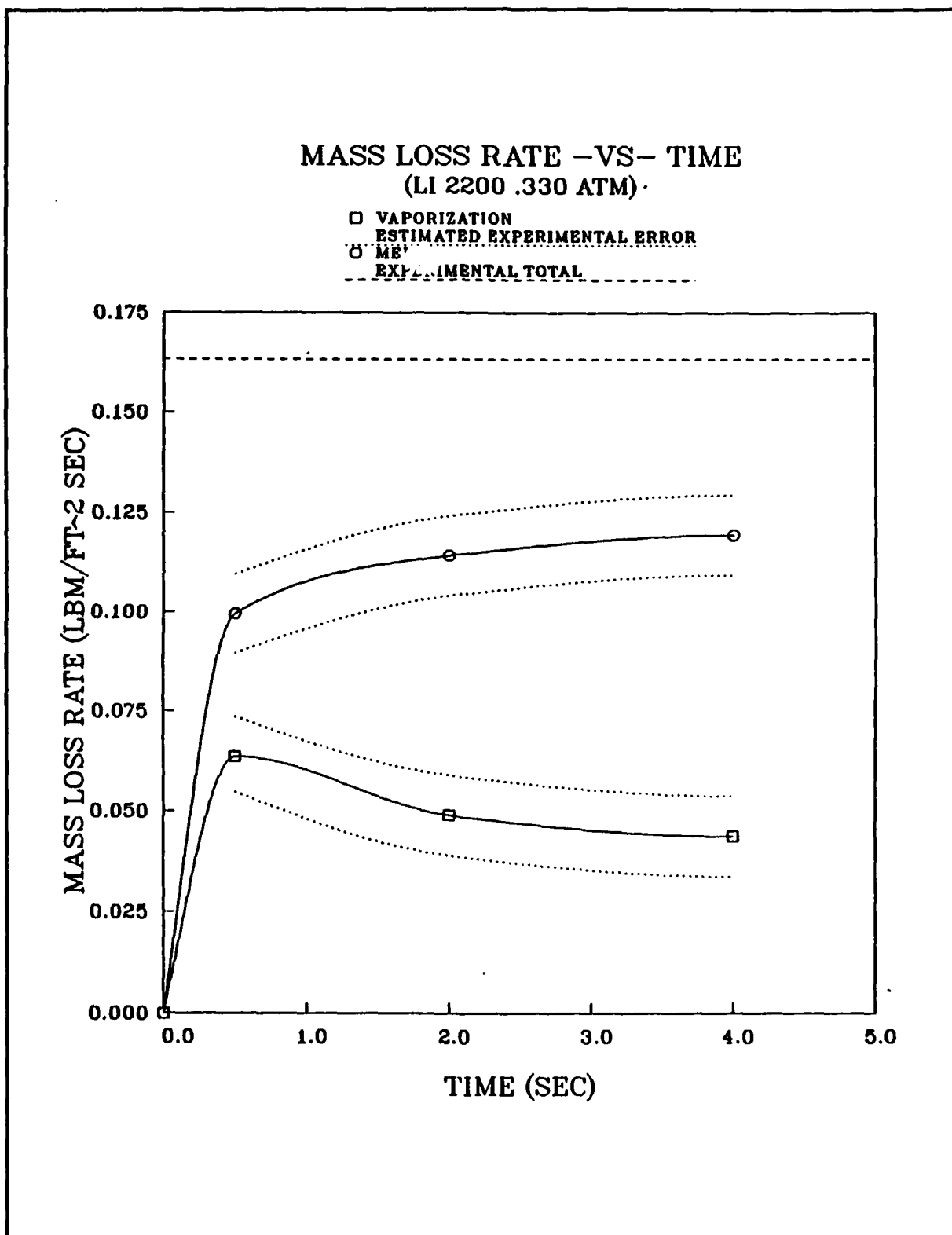
Figure 34 LI 2200 Mass Loss Rate .330 Atmospheres

54
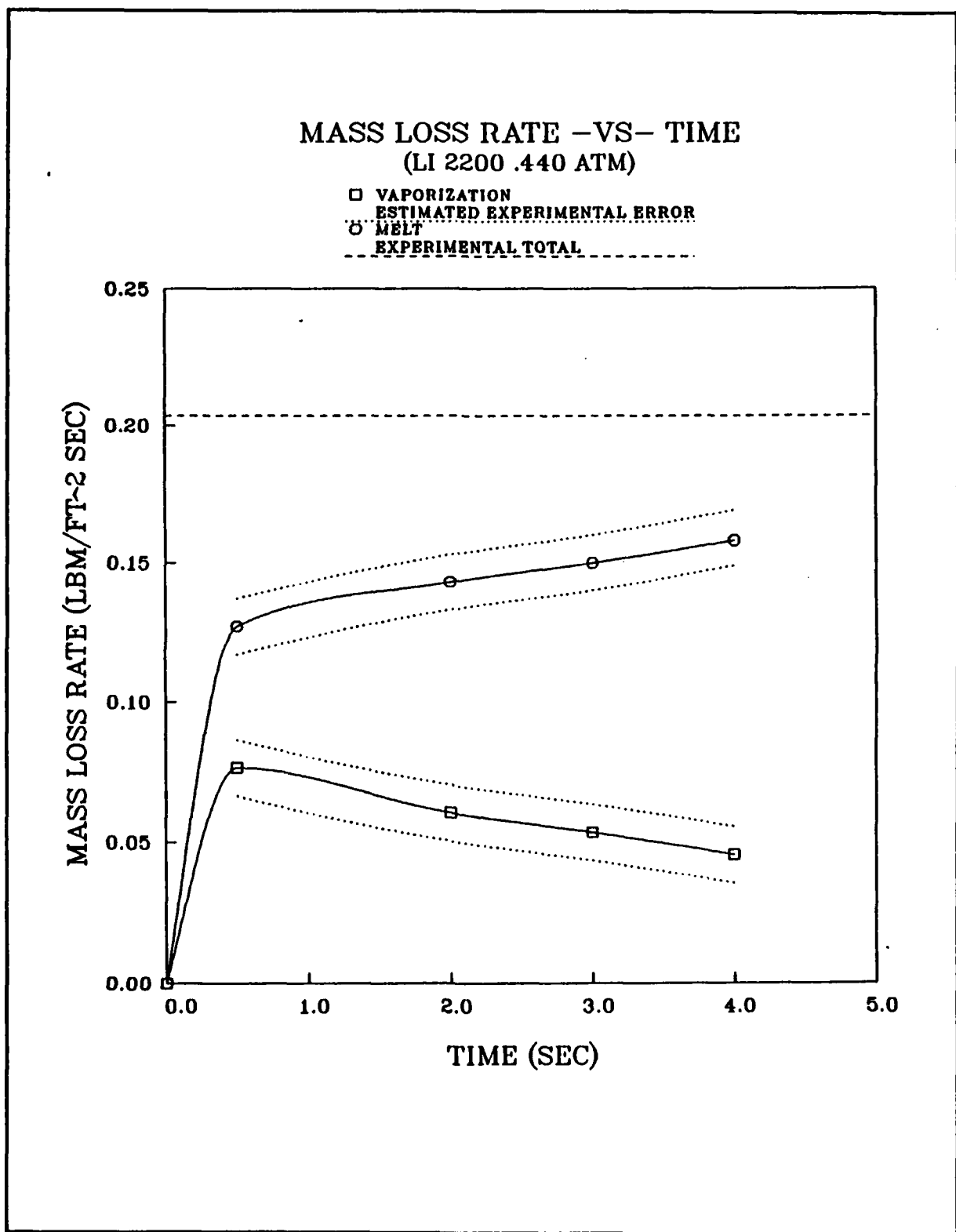
Figure 35 LI 2200 Mass Loss Rate .440 Atmospheres
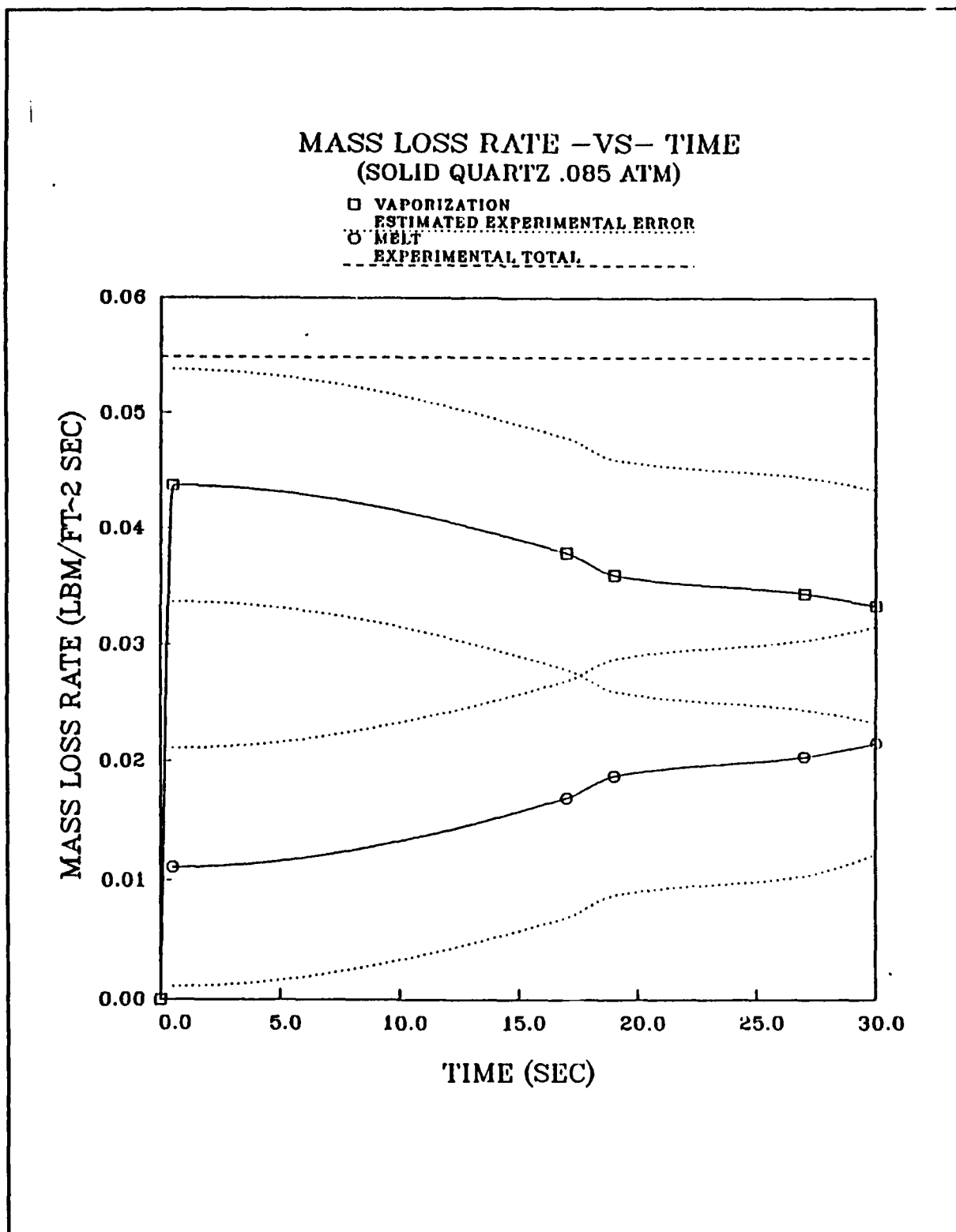
Figure 36 Solid Quartz Mass Loss Rate .085 Atmospheres
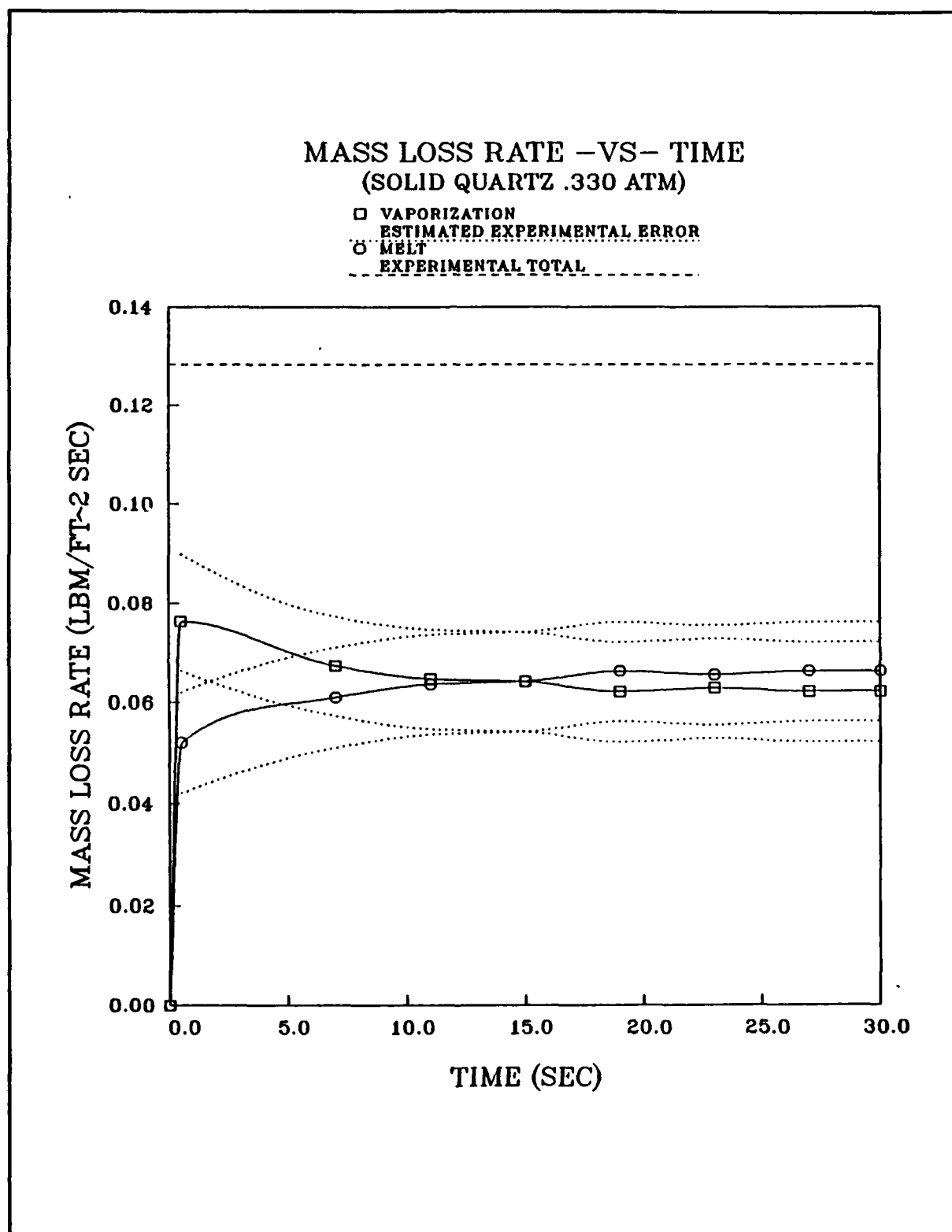
Figure 37 Solid Quartz Mass Loss Rate .330 Atmospheres

MASS LOSS RATE –VS– TIME
(SOLID QUARTZ .440 ATM)

□ VAPORIZATION
..... ESTIMATED EXPERIMENTAL ERROR
ⵔ MELT
– – EXPERIMENTAL TOTAL – – – – – –
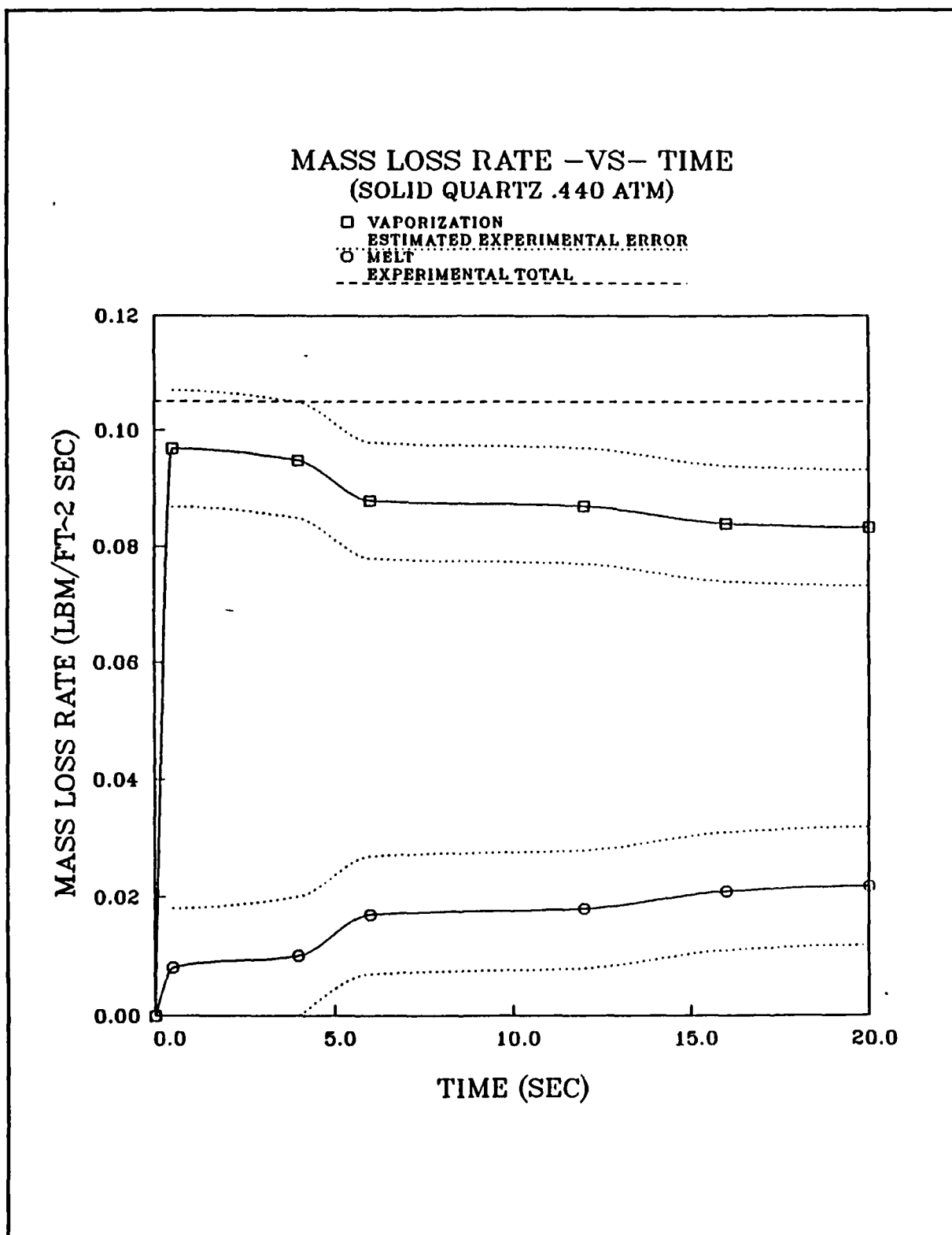
Figure 38 Solid Quartz Mass Loss Rate .440 Atmospheres

58

Figure 39 Mass Loss Rate -vs- Pressure

59
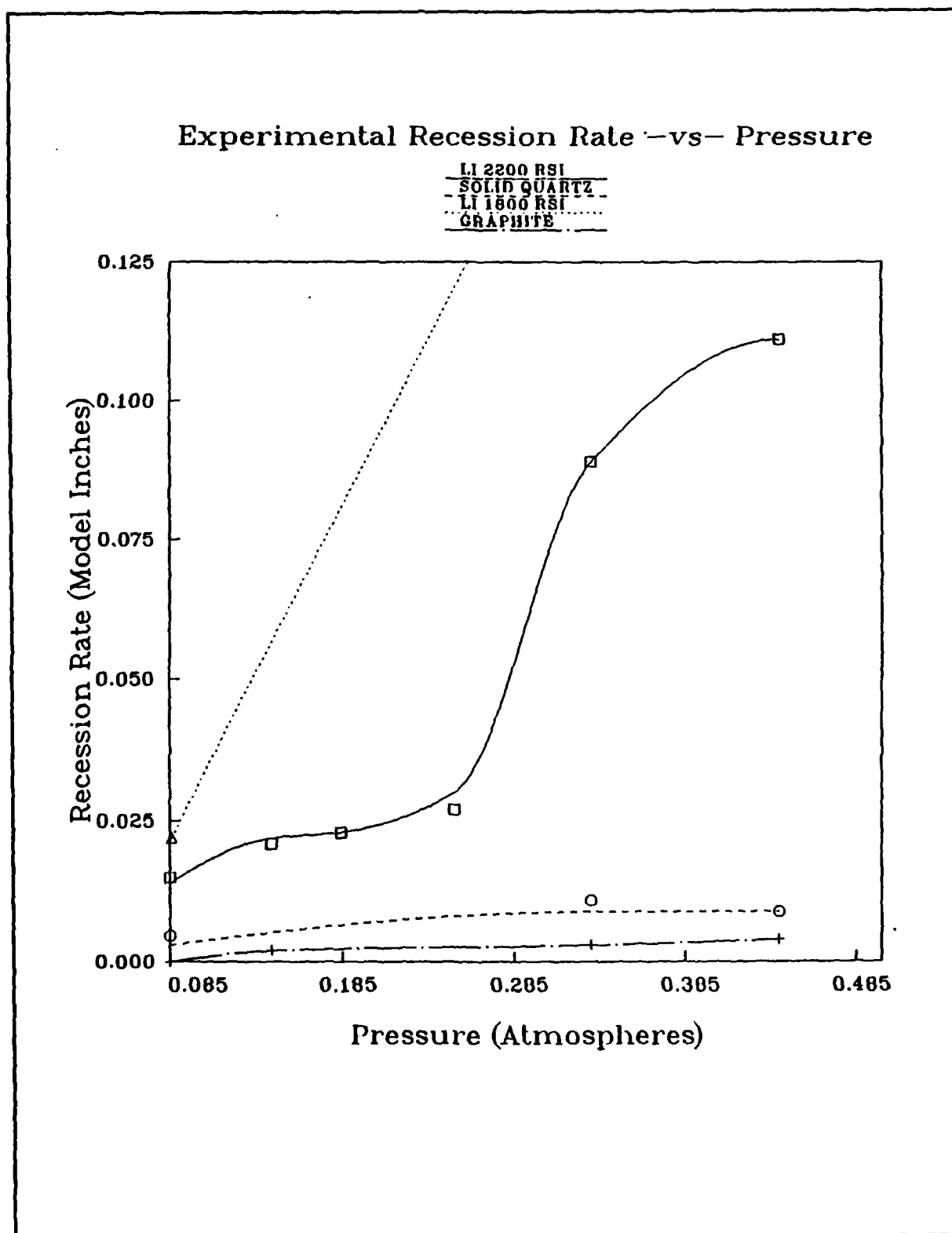
Figure 40 Recession Rate -vs- Pressure

60

GRAPHITE SURFACE TEMPERATURE 60 MW IIIF ARC-JET
CMA Prediction-ATJ Graphite Properties

0.085 Atm.	☐ .085 Atm
0.144 Atm.	○ .144 Atm
0.33 Atm	△ .330 Atm
0.44 Atm	+ .440 Atm
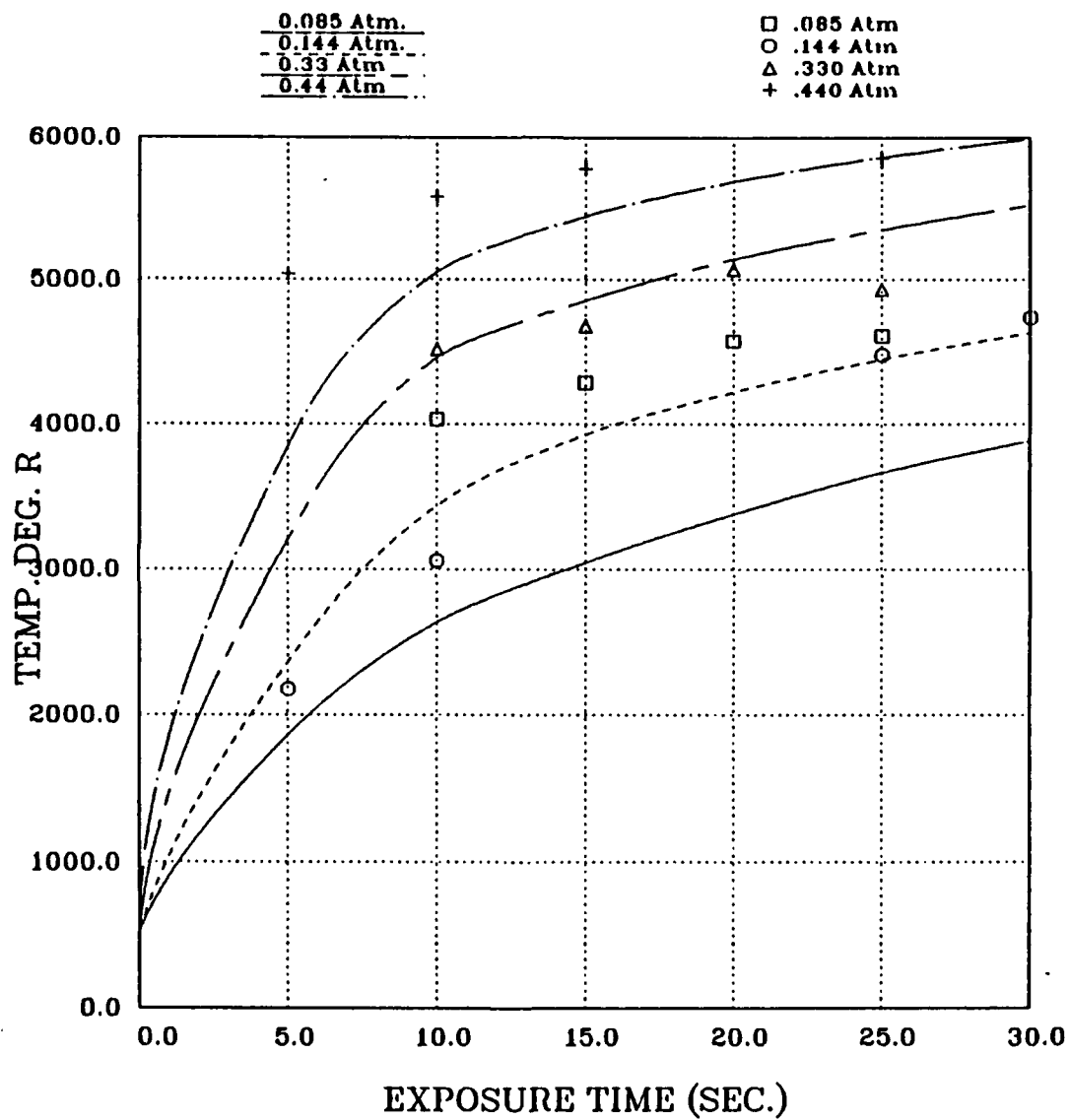
Figure 41 Graphite Surface Temperatures

61

GRAPHITE SURFACE TEMPERATURE 60 MW IHF ARC—JET
CMA Prediction—ATJ Graphite Properties
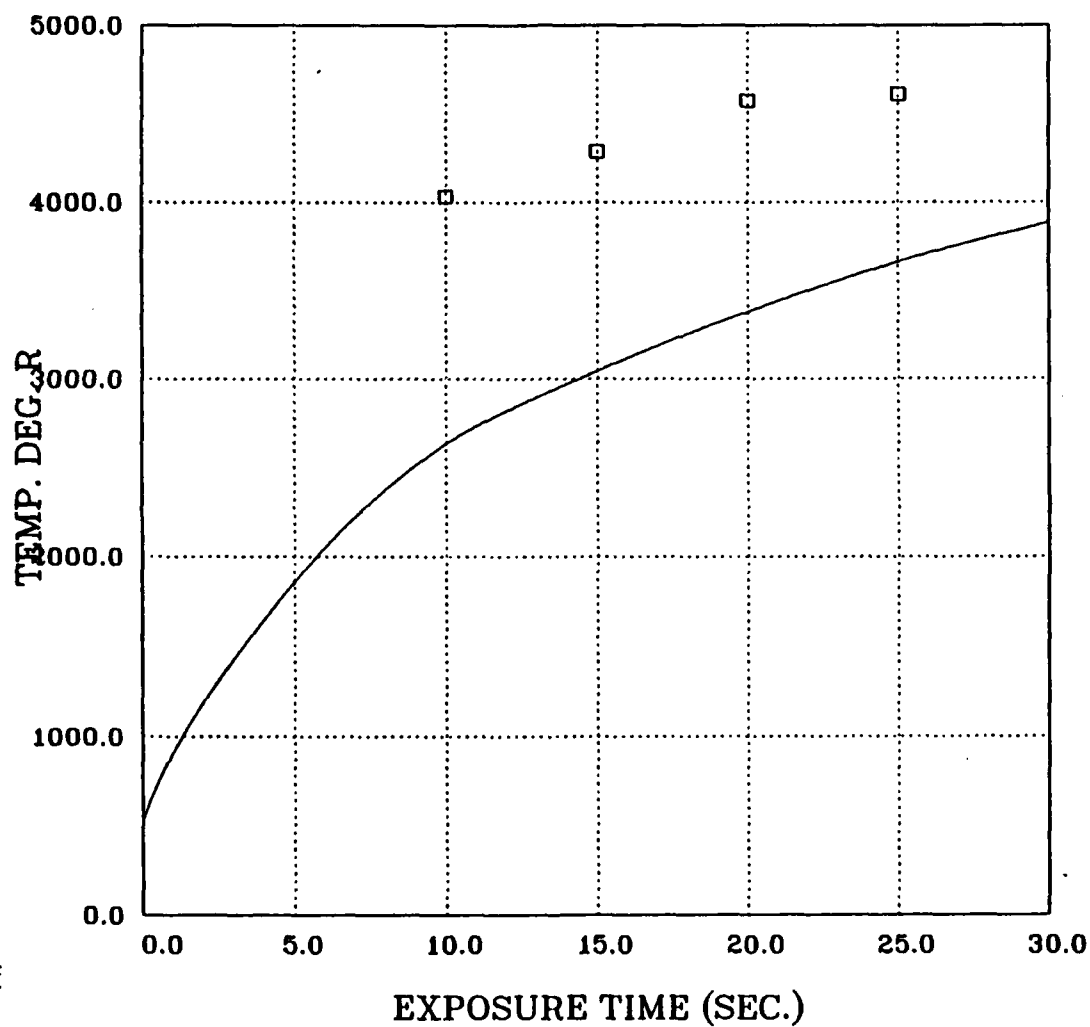
0.085 Atm.
□ .085 Atm

Figure 42 Graphite Surface Temperature .085 Atmospheres

62

GRAPHITE SURFACE TEMPERATURE 60 MW IIIF ARC−JET
CMA Prediction−ATJ Graphite Properties
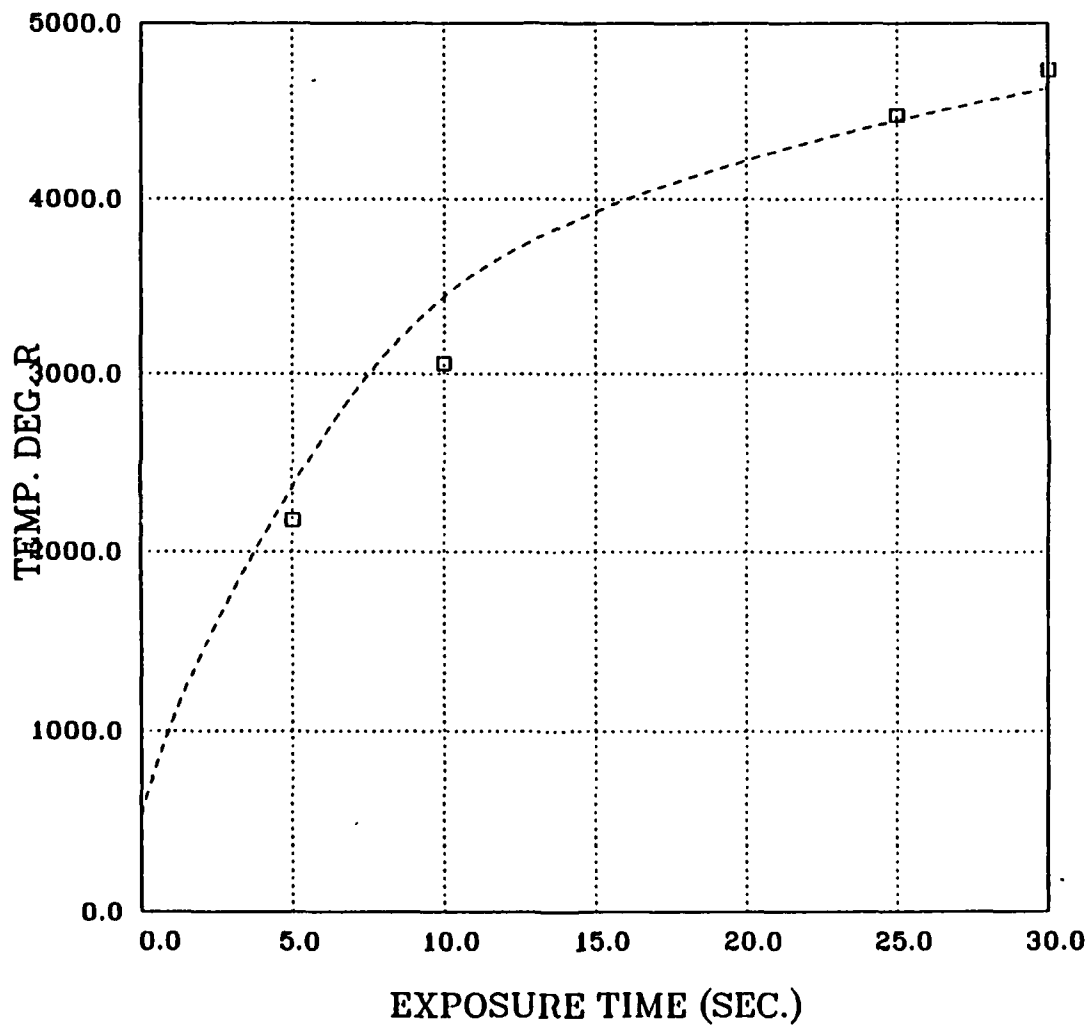
Figure 43 Graphite Surface Temperature .144 Atmospheres
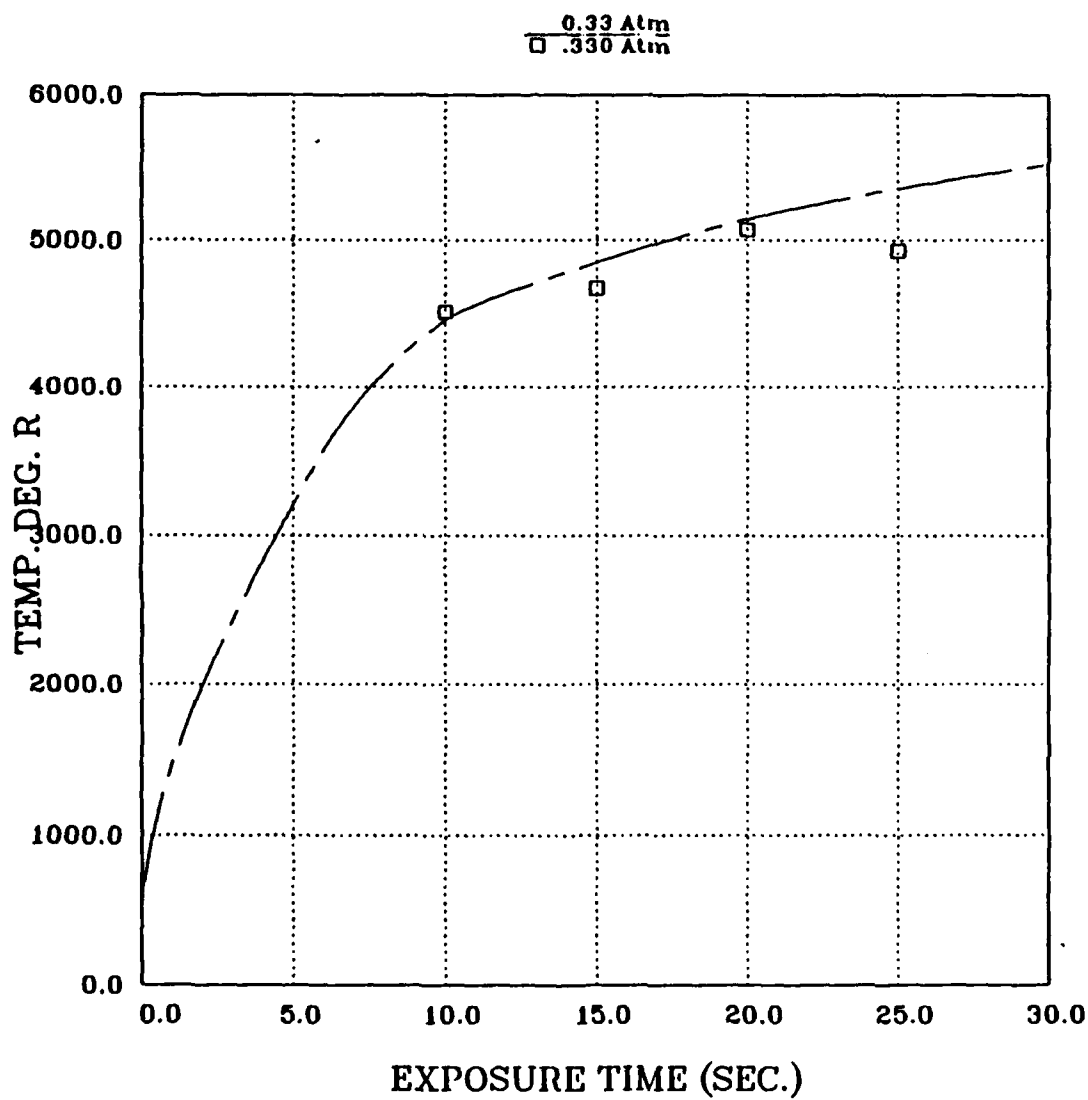
Figure 44 Graphite Surface Temperature .330 Atmospheres

64

GRAPHITE SURFACE TEMPERATURE 60 MW IIIF ARC-JET
CMA Prediction-ATJ Graphite Properties

0.44 Atm
.440 Atm
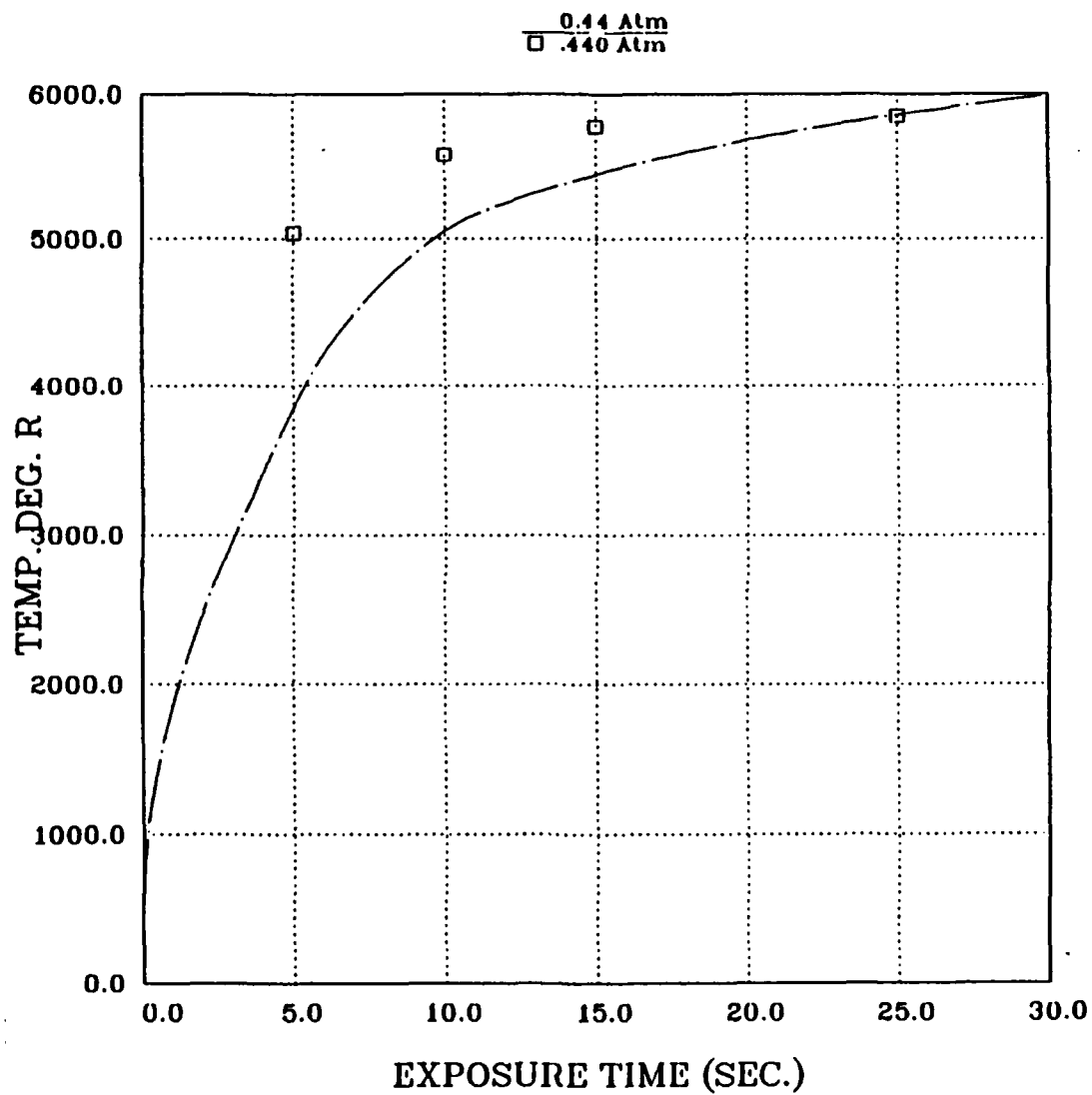
Figure 45 Graphite Surface Temperature .440 Atmospheres

65

F.   SCANNING ELECTRON MICROSCOPY

As was shown in Figure 9 in which the RSI contains the silicon carbide crystals and as mentioned previously with the structure of the RSI being a fibrous matrix of silicon dioxide fibers that have been sintered for structural integrity. Figure 47 shows a 1000 times magnification of LI 900. The fibers in the micrograph have been measured with a mean diameter of .003 mm.

Figure 26 shows a cross section of the melt layer near the surface of the RSI after it has been subject to the arc jet flow. As the surface ablates, the RSI fibers form a flowing ,frothing, bubbling liquid quartz surface. This surface near the stagnation point is shown in Figure 48 and 49, which contains many holes which are open to the virgin RSI material below. This melt layer is affected by the stagnation pressure and distance from the model stagnation point. It is theorized that the melt layer thickness increases with stagnation pressure and that there is minimal melt thickness of this layer. Confirmation can only be given to the minimal thickness of the melt layer, which agrees with the assumptions for the porous RSI melting ablator model, as shown in Figure 48. As can be seen in Figure 49 and more prominently in Figure 50 are the hardened ring waves that propagate across the melt cap surface as the model recedes. These surface ring waves are more evident in the high speed motion pictures and propagate outward from the stagnation point until the surface temperature becomes low enough that the congealing of the liquid silica overcomes the surface shear forces and the melt layer "freezes".

Figure 51 shows a similar region in a higher pressure arc jet run in which the stagnation pressure and the shear forces are great enough to close the holes found in the surface of the lower pressure test runs and make the surface smooth. The melt cap flows outward until it congeals at the lower temperature near the outer edge of the model nose where it begins to accumulate. The "frozen" layer accumulates at the edge and forms a melt layer ring around the model tip. The density of the melt layer ring may vary depending on the amount of void fraction present.

66

The melt layer ring can be seen in Figure 52 and 53, with Figure 52 containing more void area than Figure 53 melt layer ring which appears almost solid. The melt layer accumulation effectively increasing the nose radius which decreases the surface heat flux. The virgin material of the model can be seen to the right of center in Figure 52 as the melt layer rolls over the edge in a spiraling motion [Ref. 7].

The proof of concept test on water matrix models tested in the arc jet had very dissimilar surface flow appearance [Fig. 54]. The liquid silicon remained highly viscous and left large open areas exposing virgin RSI material to the flow which contained vaporizing water as a transpirative cooling agent.

Melt Runoff
Edge Ring

Flow

Cut Edge
Face

Stagnation Point

Melt Cap

FLOW
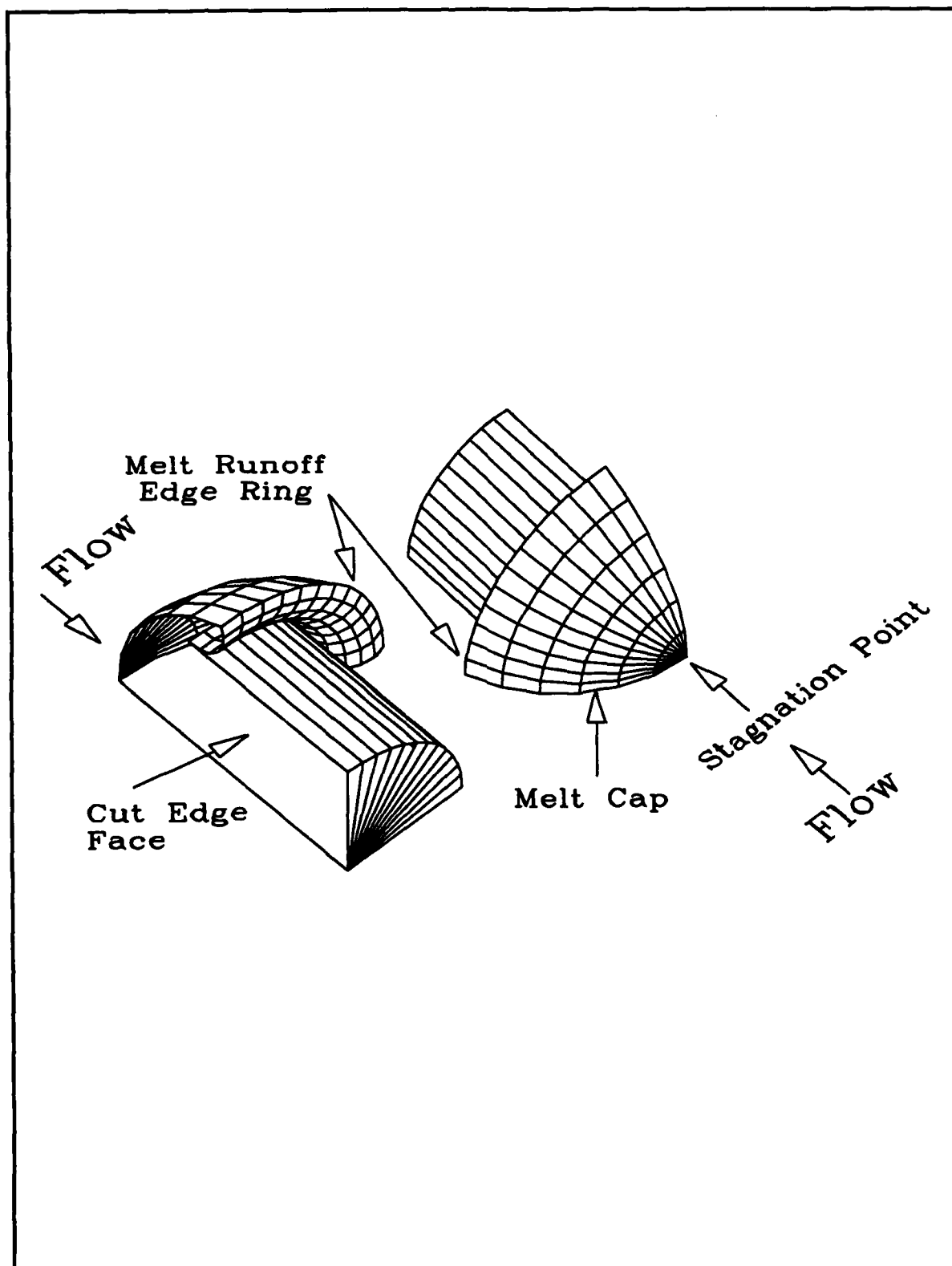
Figure 46 SEM Model Orientation

Figure 47 RSI Fibers

69

Figure 48 Melt Layer Cross Section
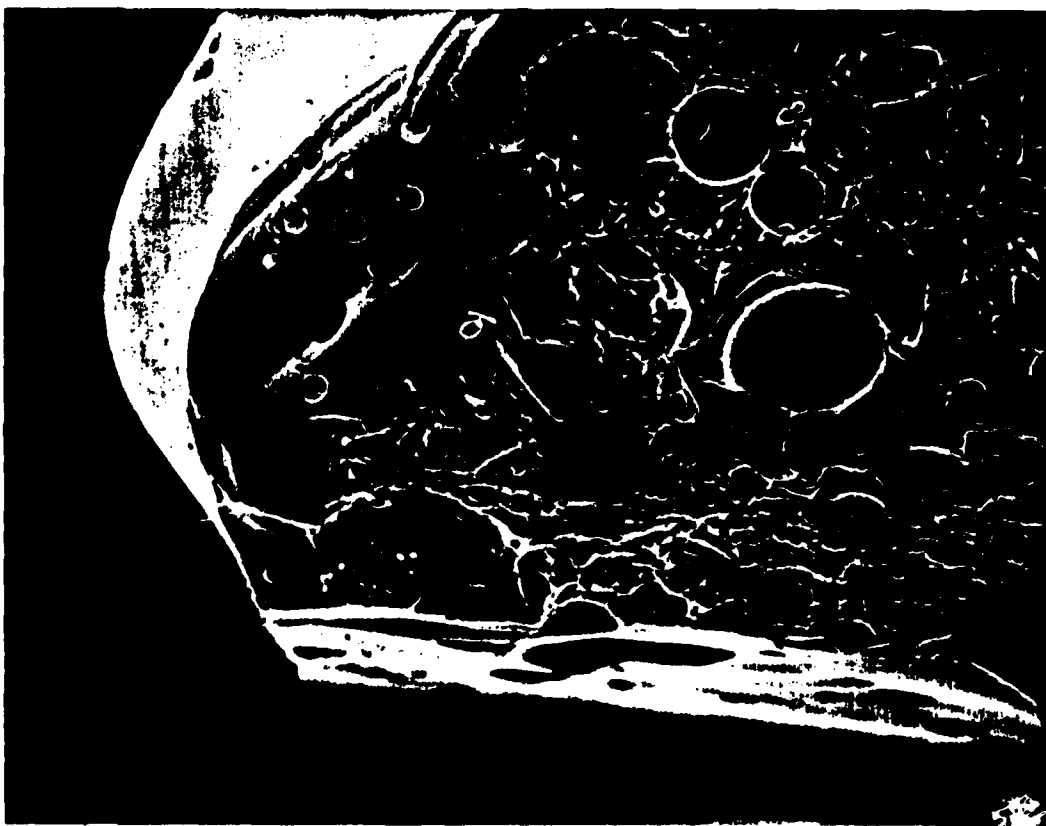
70
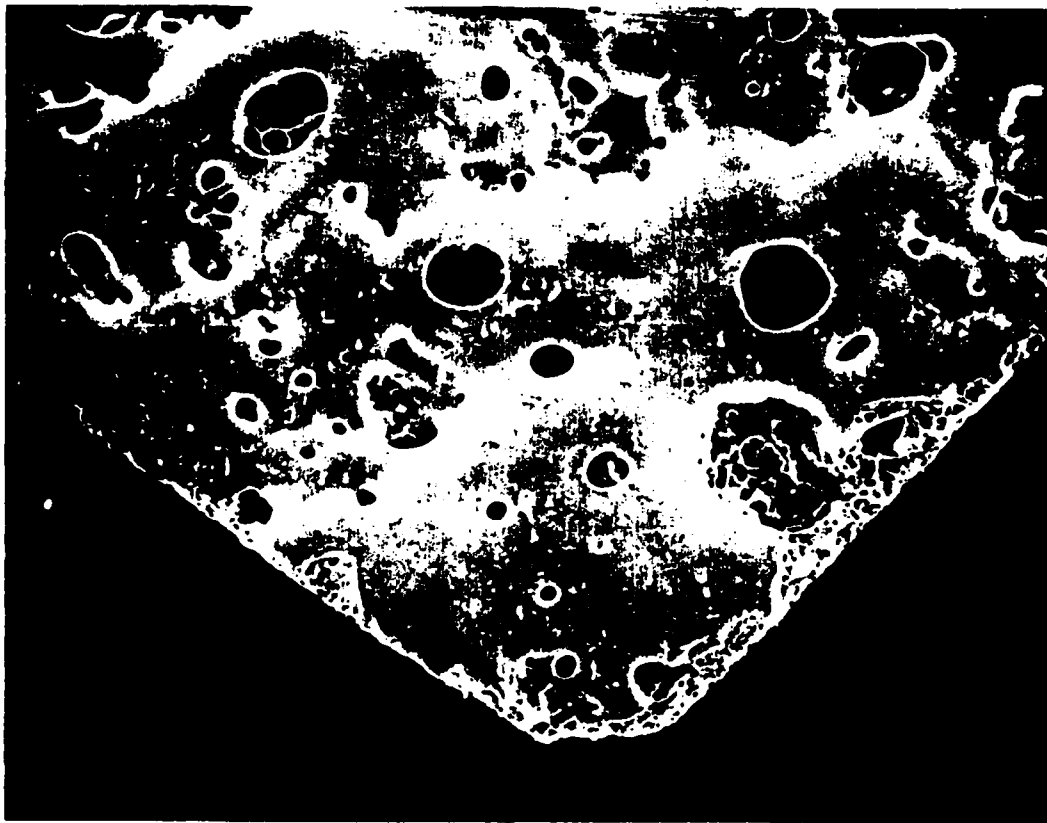
Figure 49 Melt Cap Near Stagnation Region
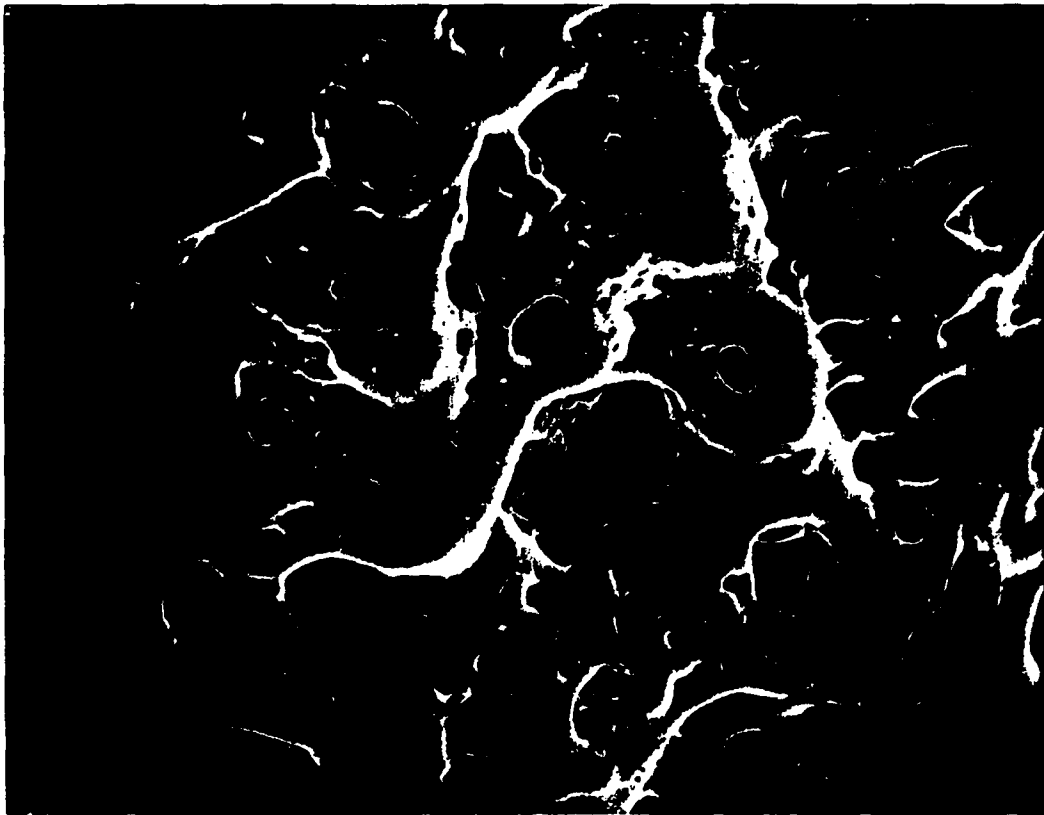
Figure 50 Melt Cap Frozen Ring Waves
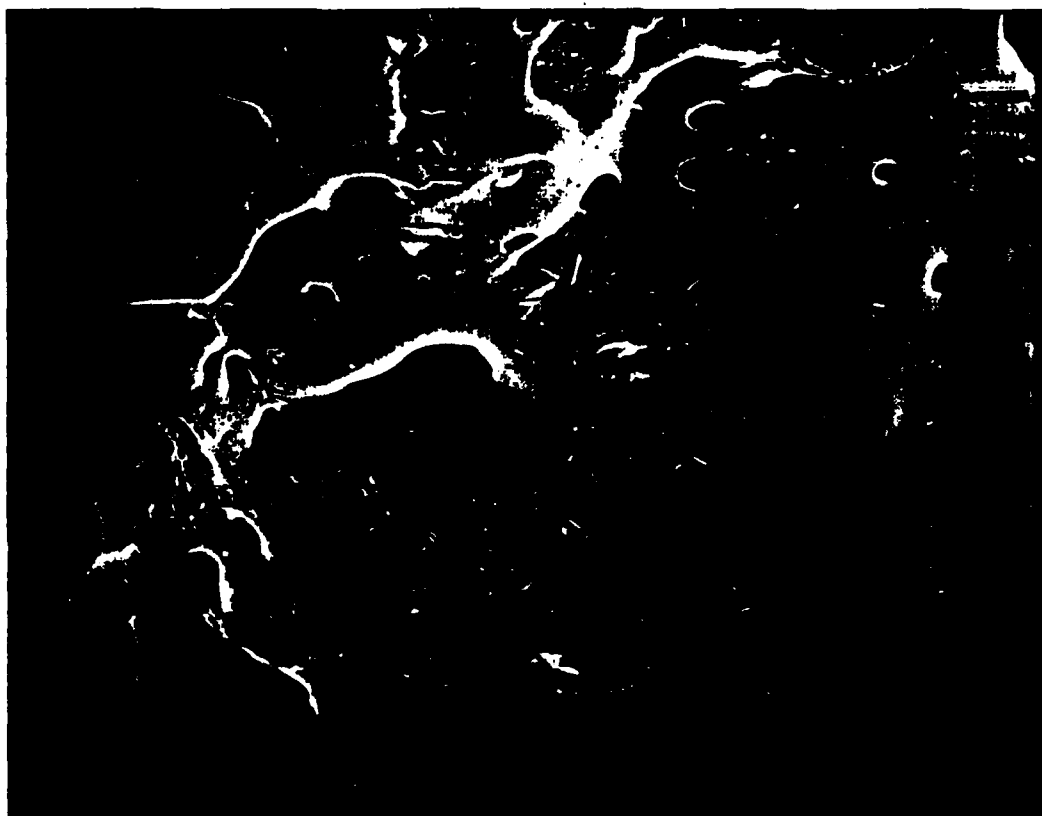
Figure 51 High Pressure Smooth Melt Cap
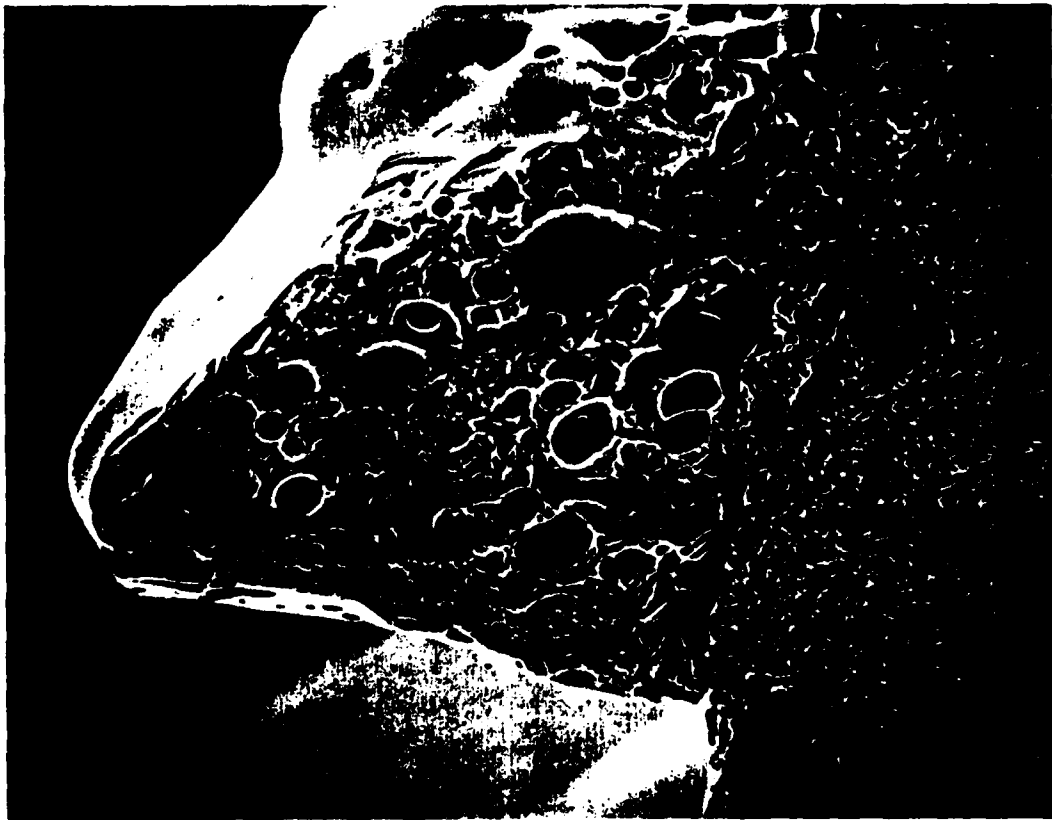
Figure 52 Melt Edge Runoff Ring

Figure 53 Melt Edge Runoff Ring

Figure 54 RSI Water Matrix Melt Cap

VI. DISCUSSION

A.   GENERAL

The data obtained from the high speed movie tracings provided the numerical values used in all of the computations. The experimental error found in the numerical evaluation of the movie tracings is estimated at approximately ten percent.

From the numerical values, the recession rates were calculated and plotted in Figures 17 through 28. The data points for each run are shown and the linear interpolation line is provided. It is apparent in some of the figures [Fig. 27 at .085 atmosphere pressure] that a time lag exists before the ablative material reaches equilibrium heating. It is after this lag that the numerical simulations assume equilibrium conditions, and the recessional values are taken. As can be clearly seen in some of the recession plots the data points are clearly linear [Fig. 23 and 18] and others are intermittently linear [Fig. 26]. With the assumption that the models ablate in a linear manner throughout the complete test run all data is compiled to represent a single line.

The structural failure of the model, which is shown in Figure 13 and correlated in Figure 20 directly affects the surface nose radius at the time of failure. However, structural failure is not accounted for in the recessional plots. This may be seen in the discontinuities of the data points in these plots.

Generally the linearity of the recession rate can be clearly seen in the model tracings Figure 12 and the Appendix.

B.   RECESSION -VS- TIME PLOTS

1.   LI 900

For the LI 900 models, only test run stagnation pressures of .085 atmospheres were performed due to the structural failure of the model almost immediately upon insertion into the act jet flow

[Appendix]. The structural failure of the model is clearly seen in the tracings. This structural failure appears to be a combination of surface ring waves in association with the surface shear forces causing a "peeling" effect of the melting surface material. The surface begins to melt, then the melt layer "peels" away leaving virgin material exposed to the arc jet flow. Due to this surface "peeling", small amounts of the melt layer would disassociate from the nose region and reattach at the model flare area. Possible mass loss could result from this mechanism and is noted on the data summary chart.

The test condition of .085 atmosphere was run three times and the data is very repeatable on the recession rate of the material.

2.   LI 900 Water Matrix

The behavior of the LI 900 water matrix model was a proof of concept experiment in transpiration cooling of the surface due to the energy absorption in the phase transformations of the water inside the model. The influence of the water into the LI 900 models had a dramatic effect on the recessional rate [Fig. 17 and 18] which is 16 times less than dry LI 900 models and even allowed an increase in the test run time duration and an increase in the flow stagnation pressure.

The model tracings clearly indicate the absence of surface "peeling" of the melt layer away from the model nose. The behavior of the model surface is very similar to a high density material at the same pressure conditions.

One concern prior to the LI 900 water matrix test was the structural toughness of the RSI to the water rapidly freezing upon pressure reduction in the test chamber. This however was not a problem as evidenced by the lack of model failure and the slow recession rates produced.

3.   LI 1800

The LI 1800 models were fabricated to test a RSI material which was an intermediate density to the LI 900 and LI 2200. This RSI contained no silicon carbide crystal as in the LI 2200 and

was pure silicon dioxide as in the LI 900 models. The model nose radius was smaller than all the other models which meant that the surface heat flux would be higher for these models. The two pressures run for the LI 1800 are one which induced structural failure, .330 atmospheres stagnation pressure and .085 atmospheres, in which the model remained intact and exhibited linear recessional properties as well as the higher pressure that cause the model to fail structurally.

4. LI 2200

Each material recession plotted against time is shown with the various pressure values having a characteristic slope difference. As seen in the Figure 20 the behavior of LI 2200 is not continuous to increasing values of stagnation pressure for approximately the same incident heat flux condition. The lower values of pressure .085, .144, .184, and .250 all are in an increasing recession rate order as the pressure increases without a major discontinuity. However when the pressure is raised to .330 and .440 atmospheres, there is a dramatic increase in the recession rates.

5. Solid Quartz

The solid quartz models are a standard against which the RSI models are compared in recession rates and surface behavior. The quartz models were run at .085, .330, and .440 atmospheres stagnation pressure for the arc jet flow. The .085 atmosphere displays the lag period discussed earlier. The discontinuity of pressures can be seen in the quartz models which is similar to that seen in the LI 2200 models, when the pressure is increased to .330 atmospheres.

The high speed movies of the quartz models show ring wave propagation from the stagnation point outward, and these waves increase in size as the stagnation pressure increases.

6. Solid Graphite

Graphite models serve as a standard for arc jet heat flux calibration data test runs which provide the flow conditions in the arc jet stream.

79

C.   NUMERICAL SOLUTIONS & DATA ANALYSIS

The values for the mass loss due to vaporization and melt runoff were obtained by application of the energy balance Equation 26 through an iterative mathematical algorithm [Appendix] in which the known test condition values along with the linear interpolative value for the equilibrium recession rate for the specific model and conditions. This interpolation produced the curves shown in Chapter 5. The mass loss by vaporization is much higher when the nose radius is small due to the higher heat fluxes. As the model surface begins to recede the heat flux decreases by the nose radius increase and also by the larger effective geometric expansion ratio of the nozzle at the model surface. Along with the calculated values is the range of the experimental error. The combination of vaporization and melt mass loss combines to result in the total measured mass loss of the model in the arc jet flow. These numbers are not in agreement at the beginning of the run but soon approach the experimental total mass loss rate. The difference between the calculated and the actual value is due partly to the non-equilibrium conditions that exist when the model is first placed into the arc jet flow and experimental model error of plus or minus 20 percent.

D.   MASS LOSS RATE -VS- TIME PLOTS

Figures 29 through 40 show graphs of the calculated mass loss rates due to vaporization and melt plotted against time and the experimental total mass loss rate measured. These plots contain an estimated 0.01 pound mass per square foot second error margin which is shown in all plots. The lower pressure test runs showed a high deviation from the experimental results. This deviation is attributed to the high percent experimental error compared to the total mass loss, which is as high as 25 percent of the total mass loss rate in .085 atmosphere LI 2200 test runs. In the higher pressure test runs the total mass loss rate is much higher and the experimental error is only ten percent of the total mass loss rate.

The mass loss rate trends with time and pressure show that the melt runoff from the ablative model is the complement of the vaporization mass loss rate to the total mass loss rate. The vaporization

80

mass loss decreases with time until a near equilibrium condition between the vaporization and melt are established. This equilibrium state between the vaporization and melt mass loss rates assumes a constant surface heat flux with a changing nose radius and subsequent heat flux changes due to the larger surface area. The surface heat flux of the model in actuality will decrease with time due to the distance change from the nozzle exit effectively increasing the geometric expansion ratio for the isentropic expansion, lowering the surface heat flux to the model surface.

The equilibrium deviations seen in Figure 29 through 40 are due to the measured nose radius fluctuations once surface thermochemical equilibrium has been reached, changing the surface heat flux and also the mass loss rates.

In all test runs except for solid quartz at .440 atmospheres, the vaporization mass loss is predominant for stagnation pressures below .330 atmospheres. Once the pressure has increased above .330 atmospheres then the melt mass loss rate predominates.

E.   SCANNING ELECTRON MICROSCOPY

Complete scanning electron microscopy studies of the ablative surface along with structural analysis of the fiber behavior near the melt surface is beyond the scope of this thesis. The use of the micrographs was vital in modeling the surface behavior for mathematical predictions, and also provided information to the validity of previous assumptions regarding the melt layer thickness with regard to the radius of curvature of the model.

F.   GRAPHITE SURFACE TEMPERATURE

Figures 42 through 45 show the correlation between the observed surface temperatures of the solid graphite models and that generated by a computer code [Ref. 4]. There is good correlation at .144 and .330 atmospheres in both trend and equilibrium temperature. The .440 atmosphere computer approximation had the same equilibrium temperature yet the actual temperature increase was much lower than predicted.

81

The predicted values for the .085 atmosphere test conditions was much lower then the observed data points, up to 1500 degrees Rankine. The high variance in the .085 atmosphere test run may be attributed to improper arc jet conditions or a lack of accuracy in the computer prediction at the lower pressure.

VII. CONCLUSIONS

A. GENERAL

The results of the investigation of the ablative properties of RSI materials for the vehicle return of the proposed Earth/Mars indicate that this material would be a feasible option at pressures less than 0.1 atmospheres on the heat shield material and that mathematical model predictions are possible for mass loss rate and melt runoff.

Recession was not a linear function of material density and stagnation pressure. This indicates weight savings is possible through use of RSI materials as a melting ablative heat shield. The structural failure of the RSI at higher pressures would create not only inconsistencies in the heat transfer rates to the back face of the heat shield, but also controllability problems in the vehicle trajectory, with aberrations in the ablative surface as indicated in the tracings [Appendix].

A more in-depth study of the pressure effect is needed to determine the proper density needed for the RSI used in an aerocapture or earth reentry profile. The use of RSI as an ablative heat shield is promising for the future of the proposed NASA Earth/Mars mission.

B. PRESSURE EFFECTS ON RSI

Stagnation pressure increases of the test conditions with constant surface heat fluxes show that the material behavior is responsible for the dramatic increase in the recession at the higher pressures through failure and disruption of the flow surface. The shear forces on the melting surface overcome the surface tension of the melt layer and cause the "peeling" effect. A more viscous melt layer perhaps could withstand the shear forces and not "peel". The transition of all recession rates of the glassy materials at the .330 atmospheres stagnation pressure shows a material behavioral change in the glassy ablator which is not displayed in the graphite, charring ablator models. The discontinuity in the recession rate of the

83

glassy ablators as compared to the continuous change in the charring ablator shows that the arc jet flow does not have an abrupt discontinuity in the flow characteristics at this point. Rarefied gas flow may exist in the arc jet model test conditions and this may be a large component in the deviations of the observed and calculated results.

C.   RSI WATER MATRIX

The proof of concept in the use of a water RSI matrix exposure to reentry heating had a recessional rate much less than was anticipated. The possibility of using a water matrix material for a reentry heat shield purpose would allow great weight savings in the heat shield,and the payload weight could be increased, provided water was already needed on-board. The water used in the matrix would come from existing on-board supplies and possible use of aqueous waste materials which contain high percentages of water. The aqueous liquid would be pumped from the on-board containment vessels into the dry RSI heat shield which would be isolated from space so that the liquid would be allowed to flow throughout the RSI. Once the liquid had completely permeated the RSI, the heat shield would be exposed to the low pressure (vacuum) of space and allow the liquid to freeze, just as in the arc jet tests. The frozen water matrix would then be ready for reentry or an aerocapture maneuver. The behavior of the water matrix showed a 16 fold decrease in the recession rate compared with the same RSI in a dry state. Using this technique, the use of existing materials could provide for a large weight savings in the heat shield and should be considered for future studies.

APPENDIX
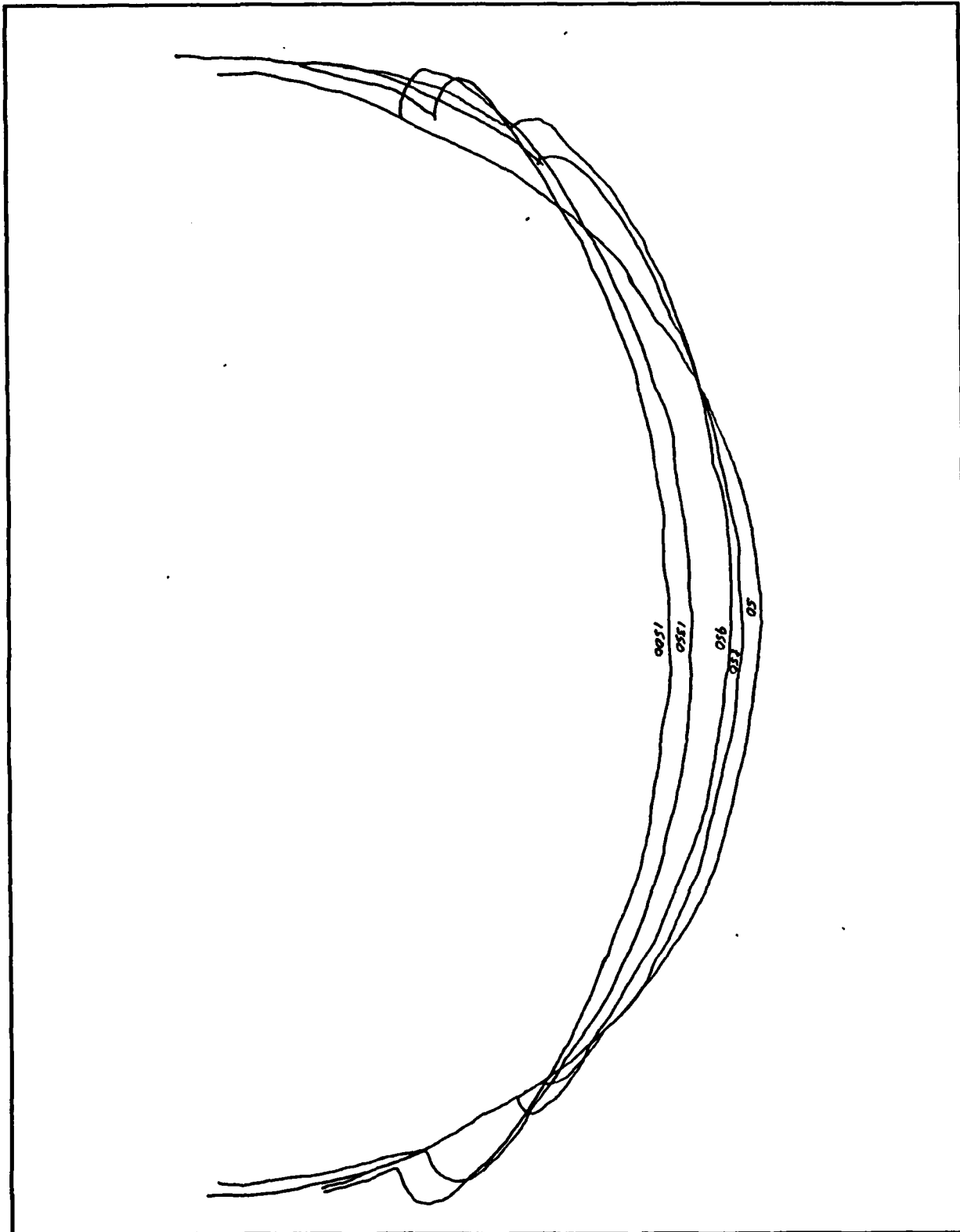
Figure 55 Run 1 Tracing
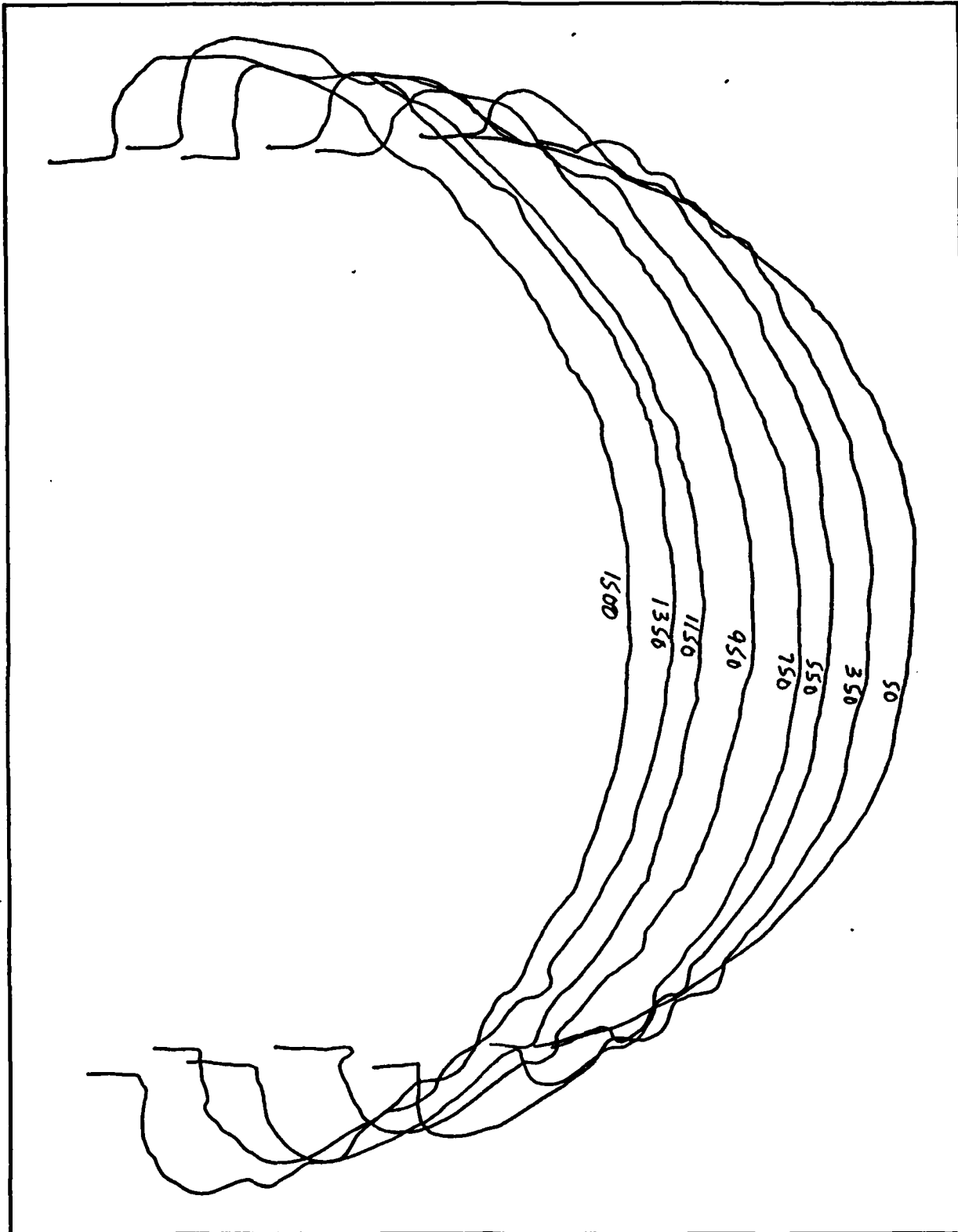
Figure 56 Run 2 Tracing
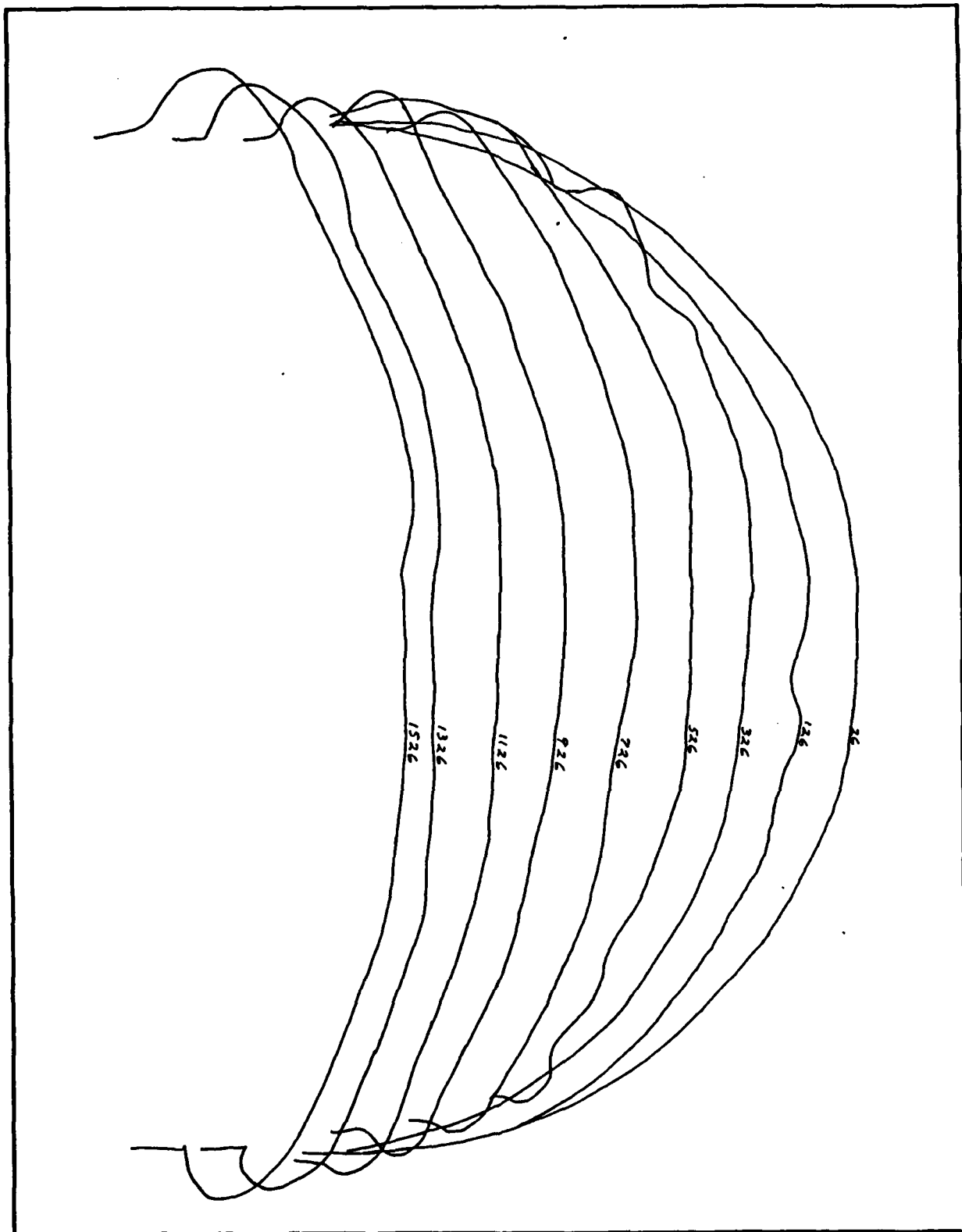
Figure 57 Run 3 Tracing

88
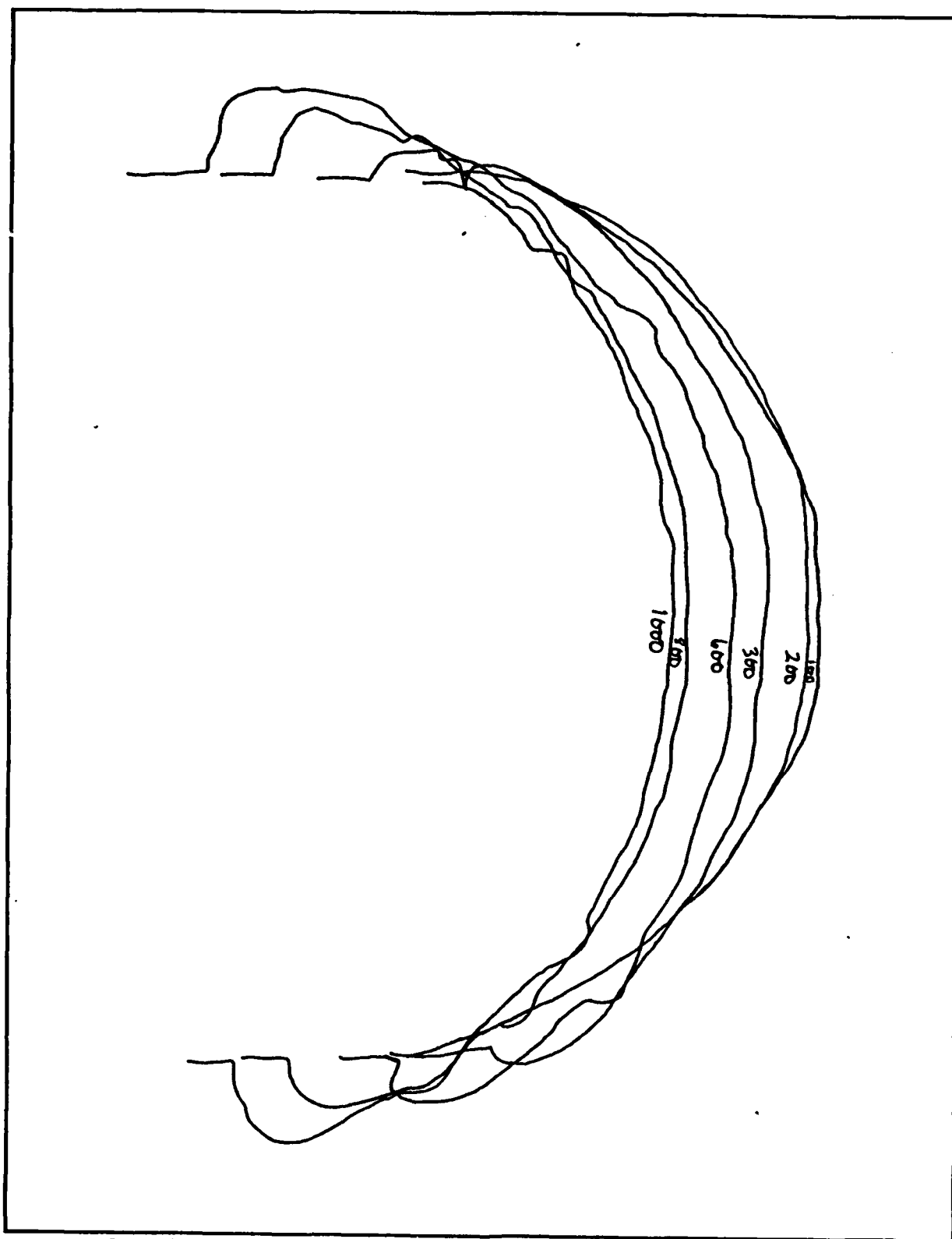
Figure 58 Run 4 Tracing

89
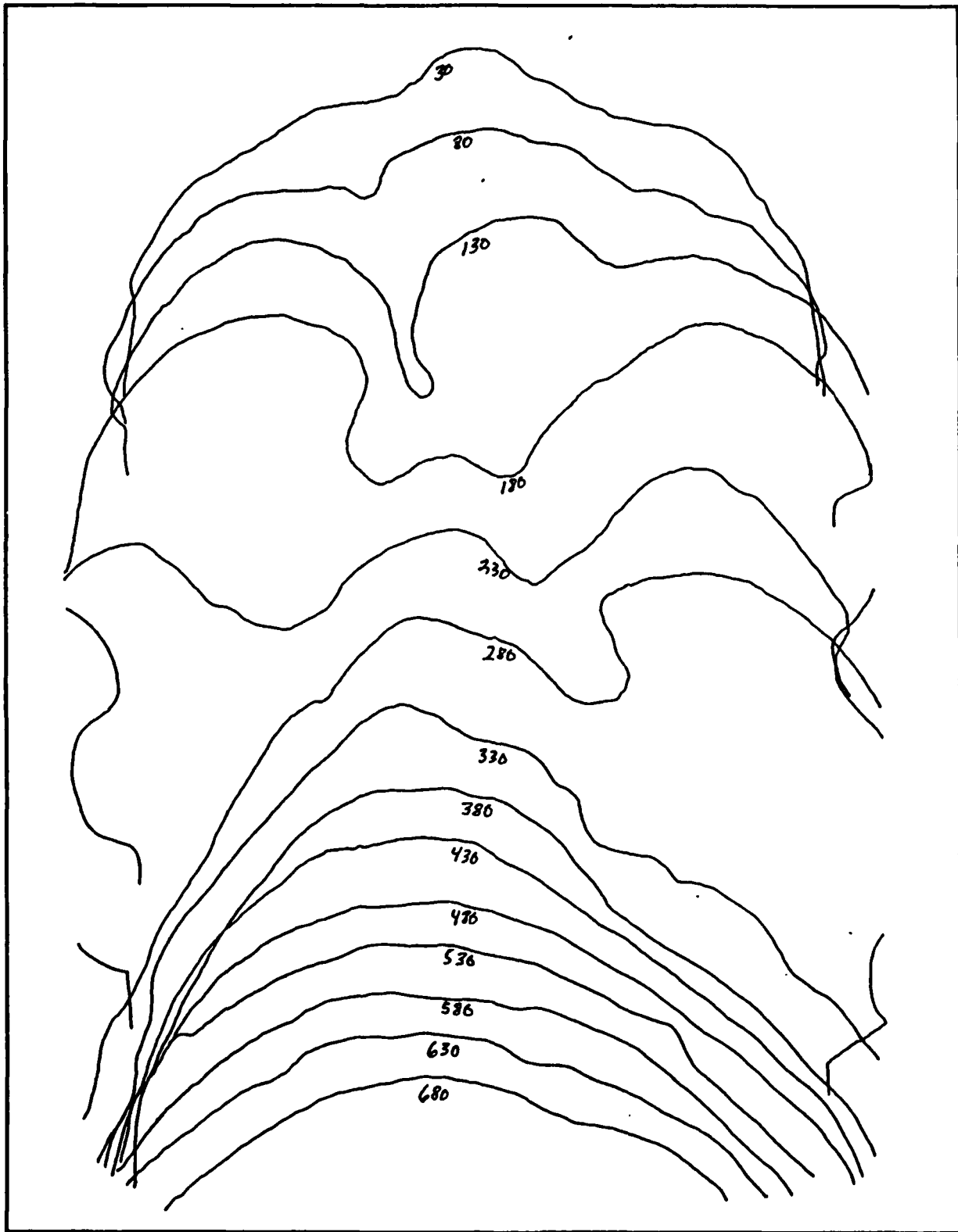
Figure 59 Run 7 Tracing

90
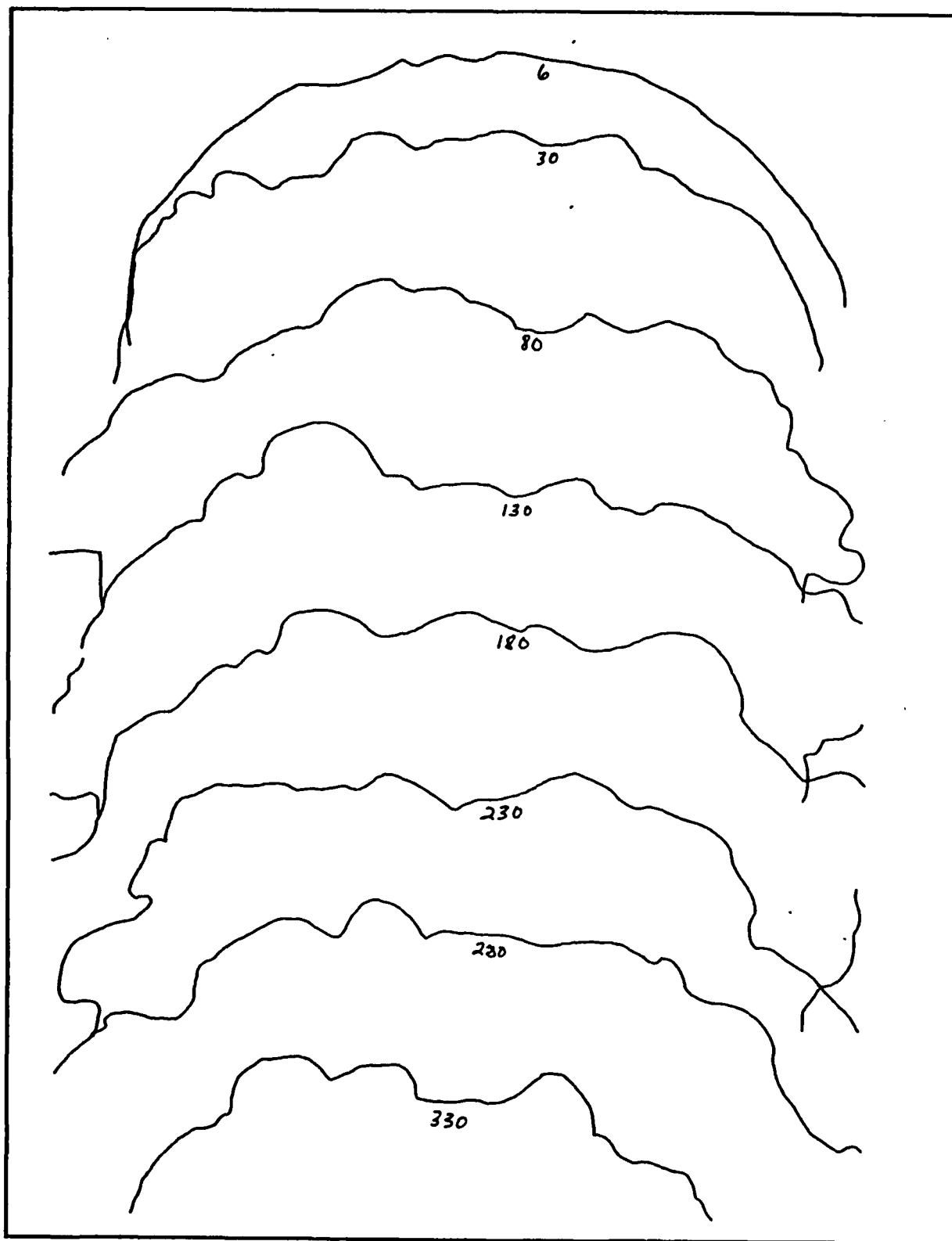
Figure 60 Run 8 Tracing
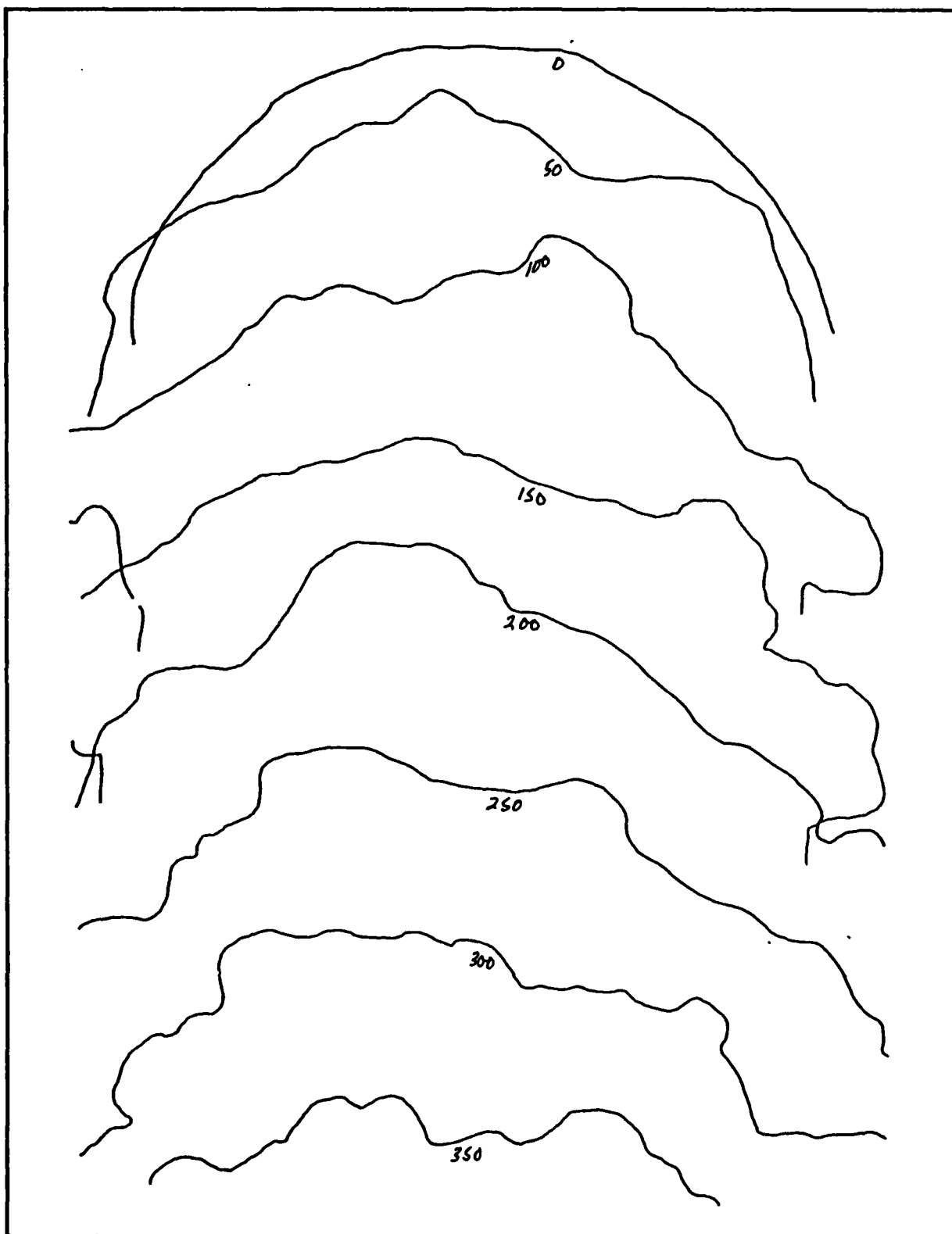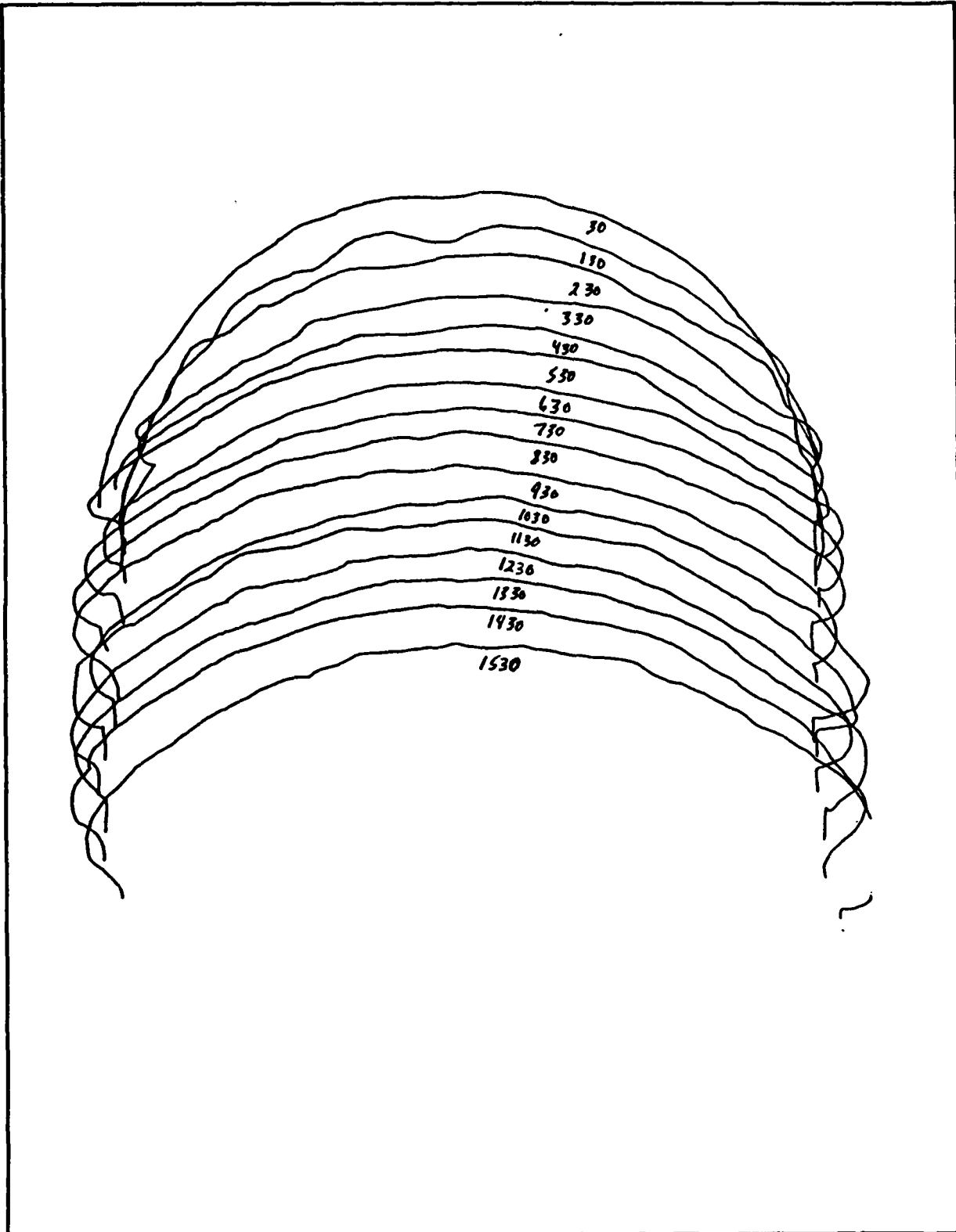
Figure 61 Run 9 Tracing
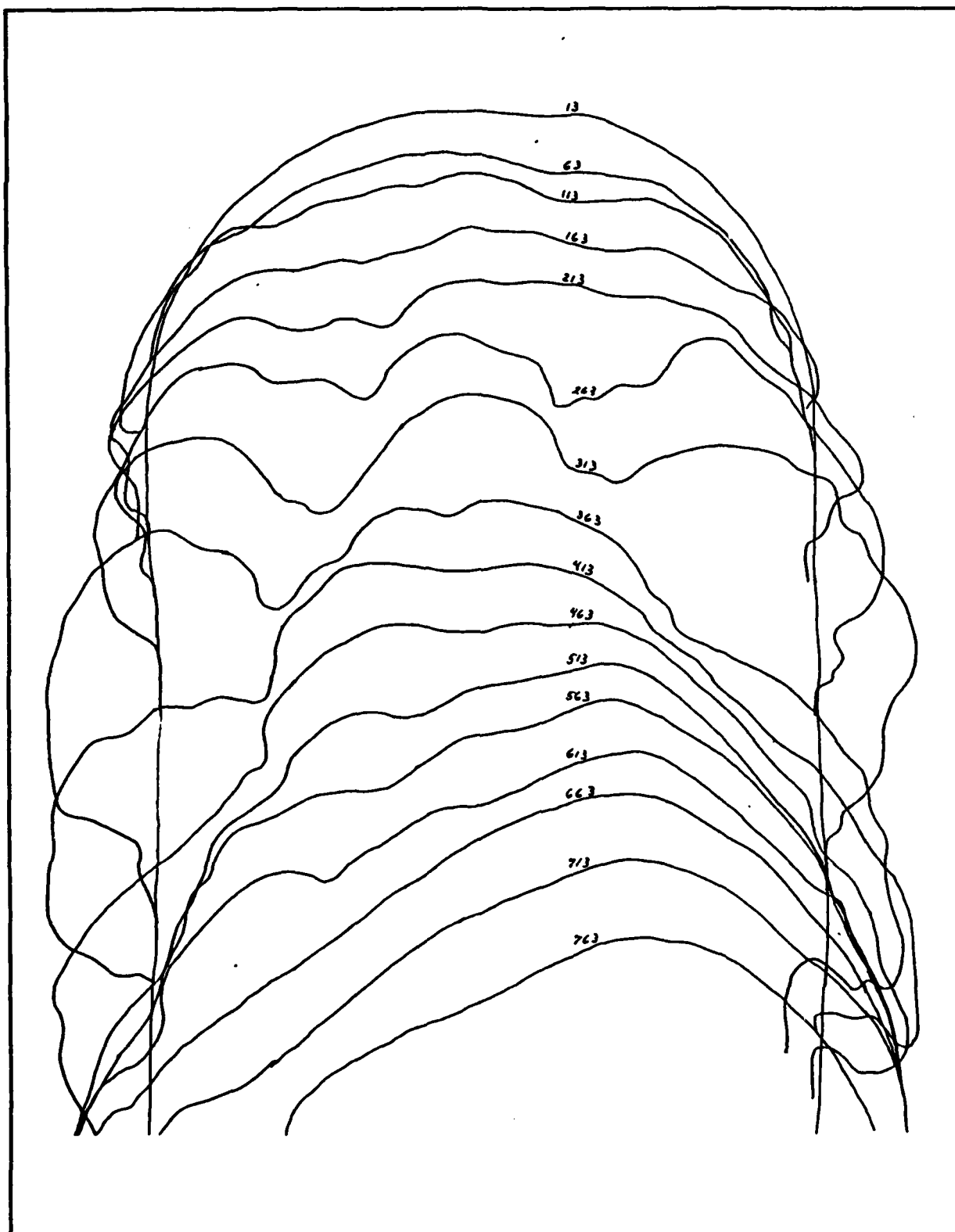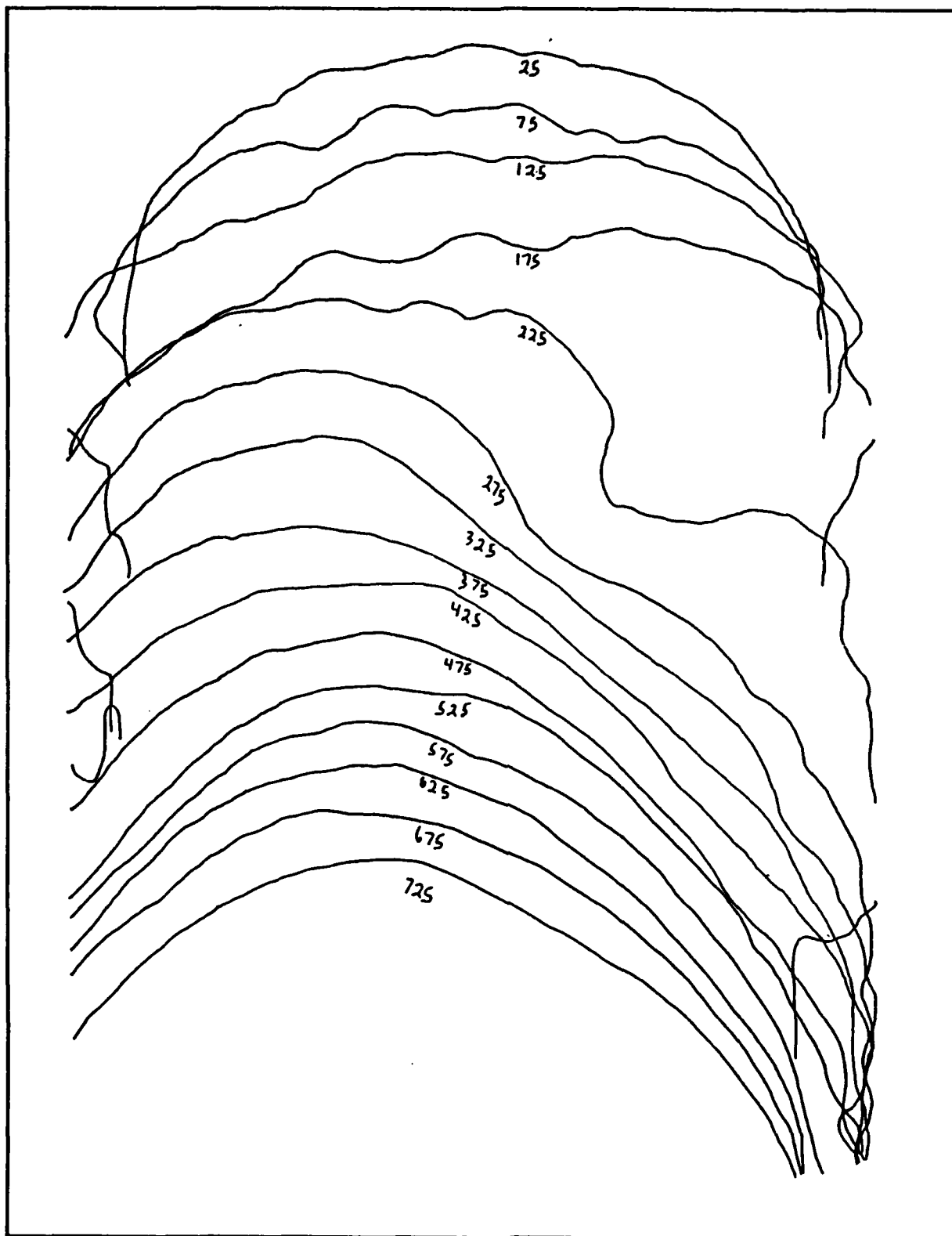
92

Figure 62 Run 10 Tracing

Figure 63 Run 12 Tracing
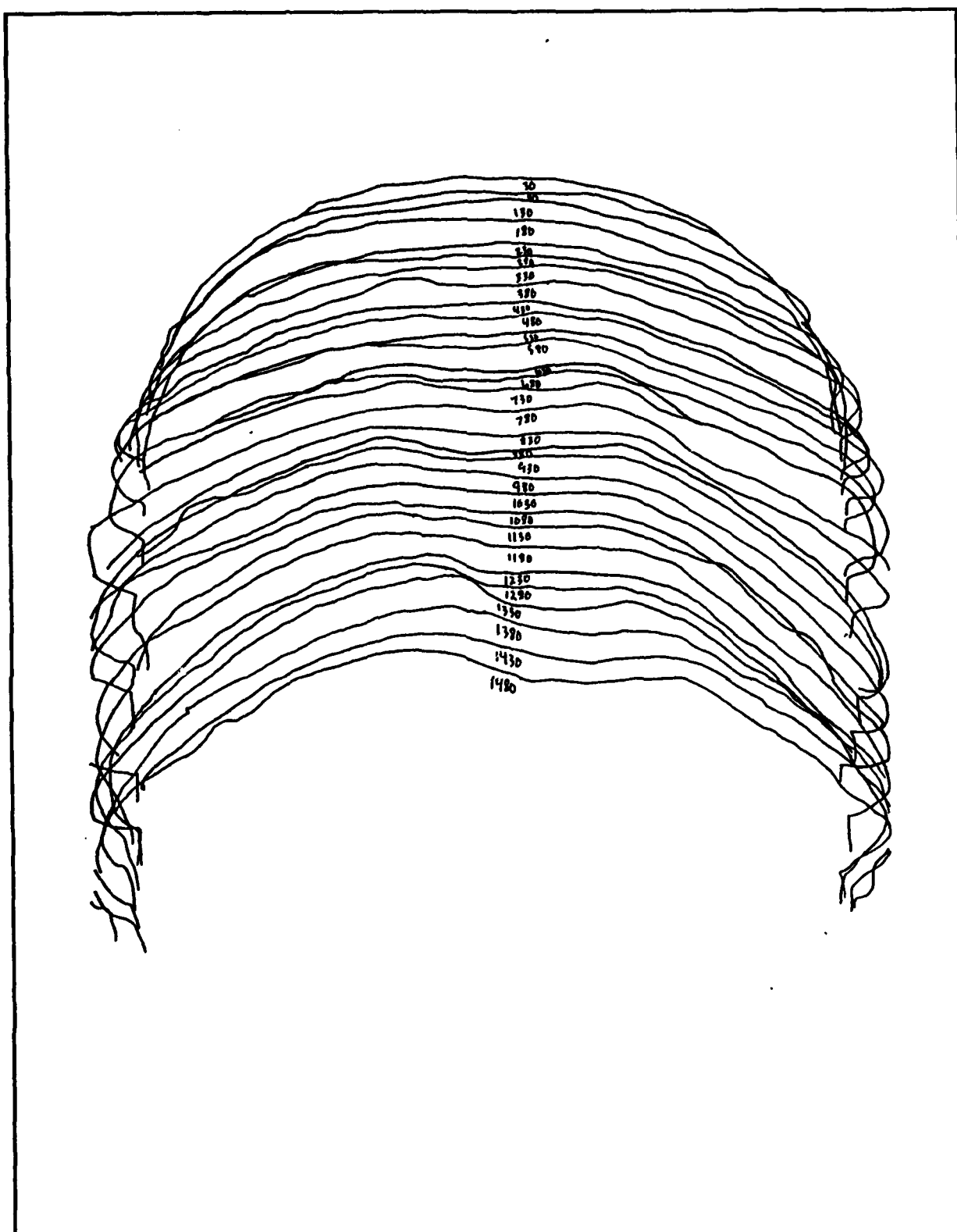
94

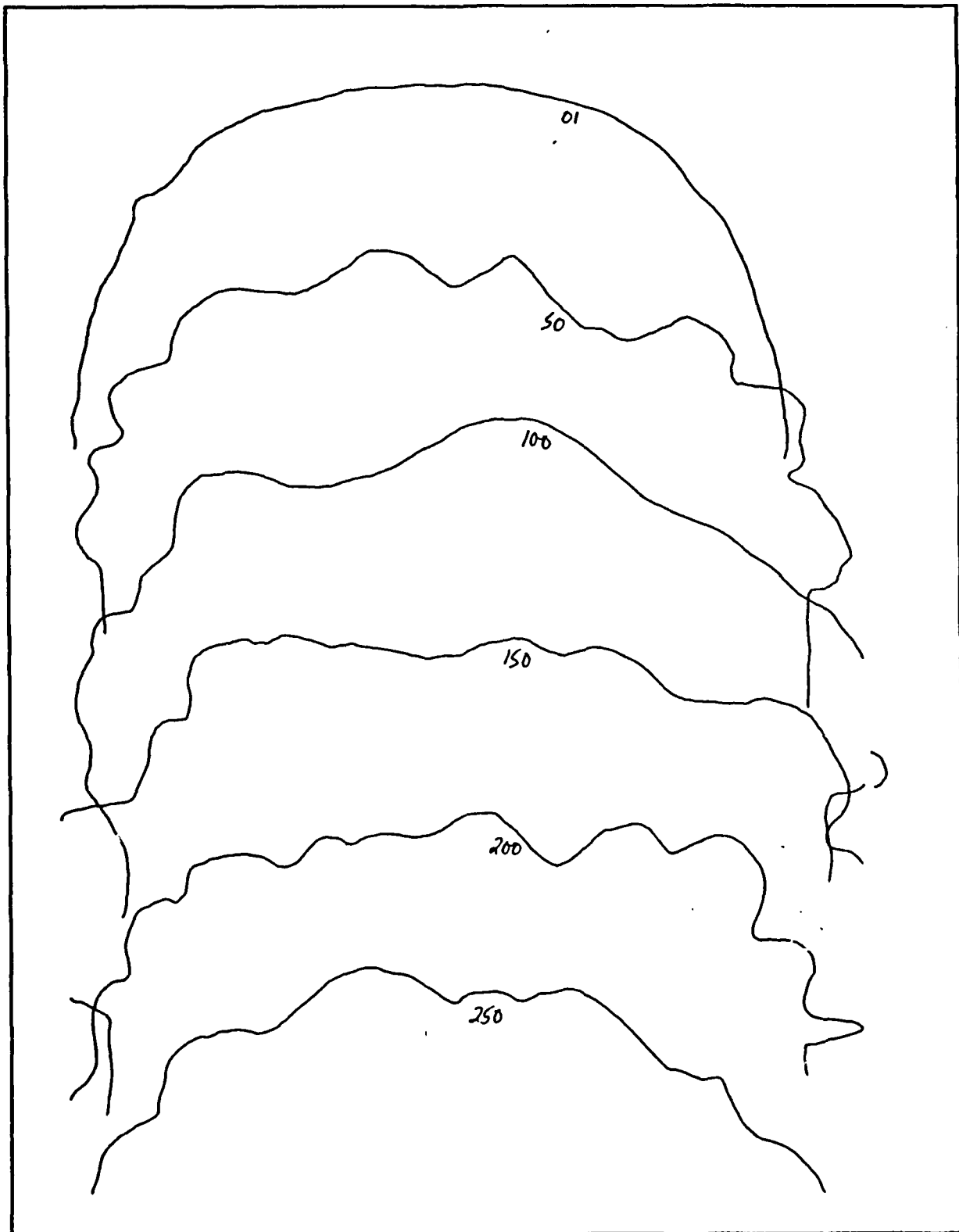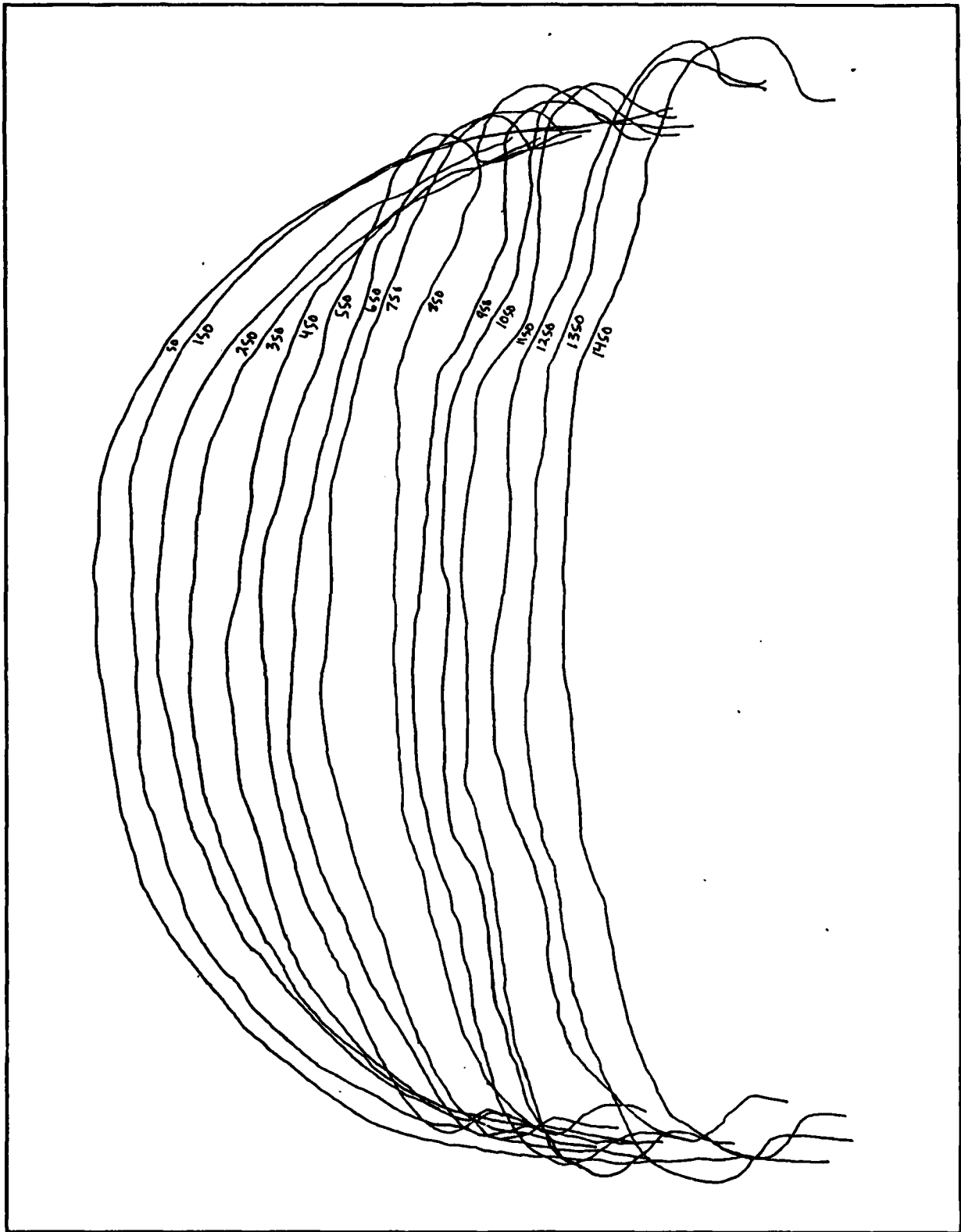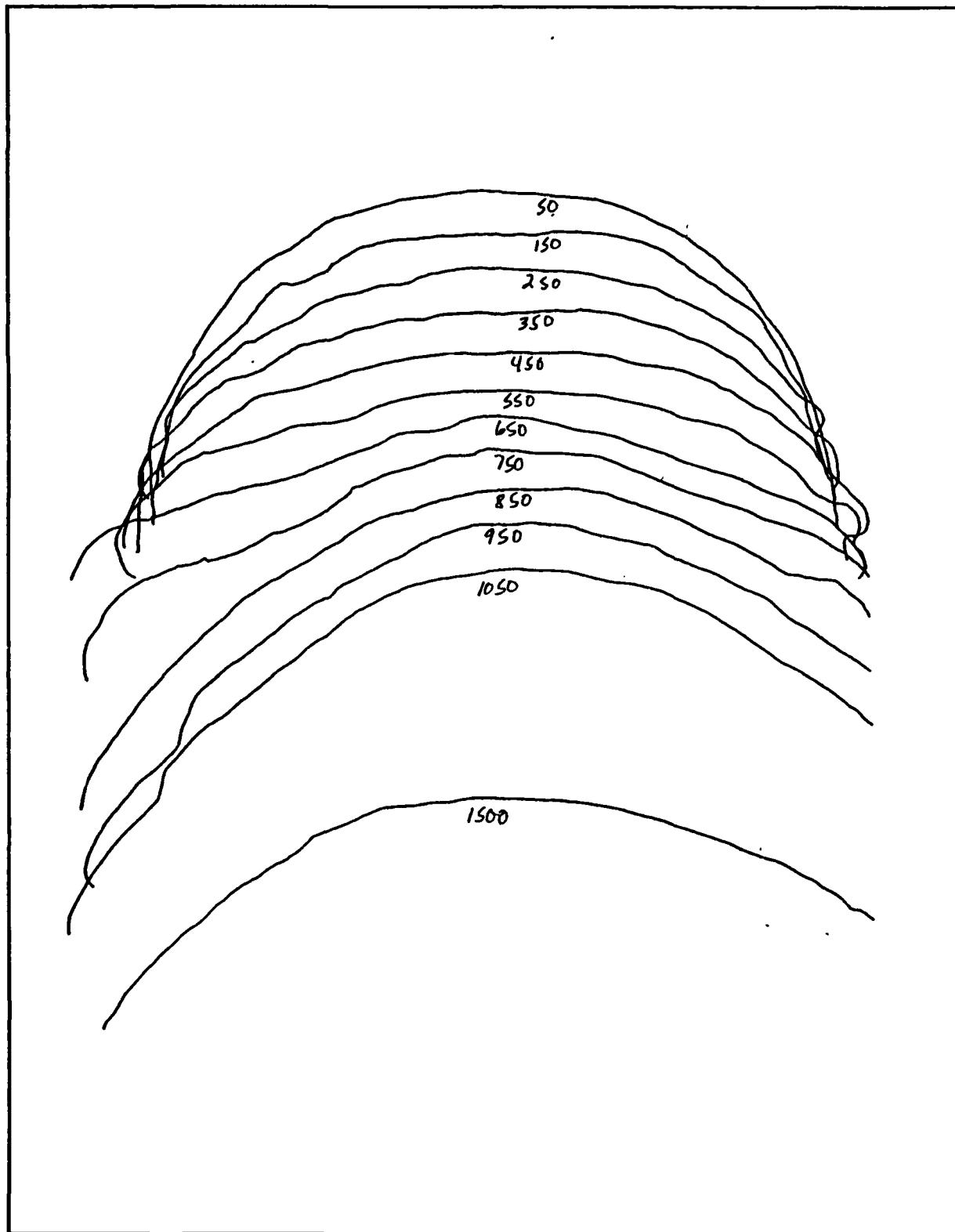**Figure 64 Run 13 Tracing**

Figure 65 Run 16 Tracing

96

Figure 66 Run 17 Tracing

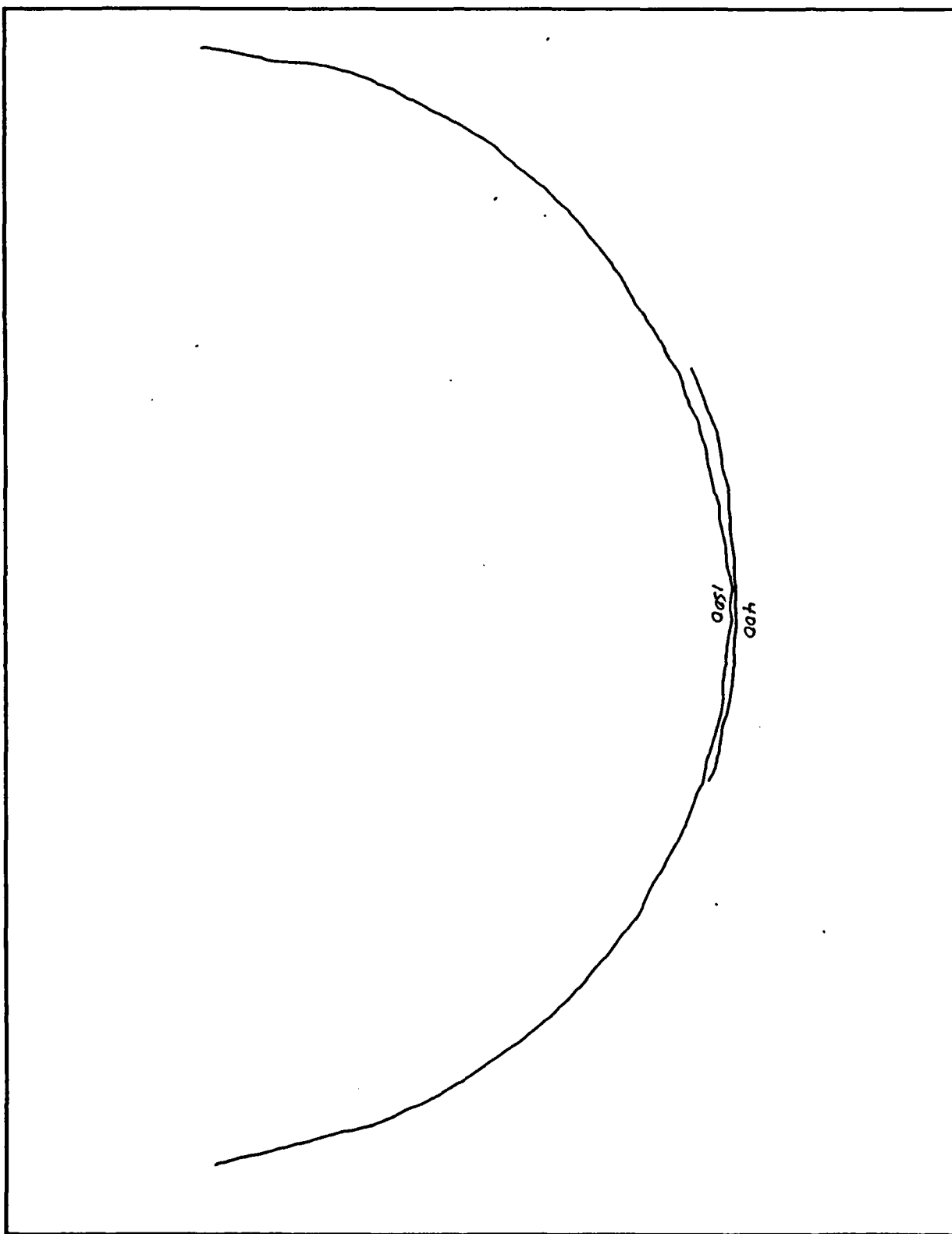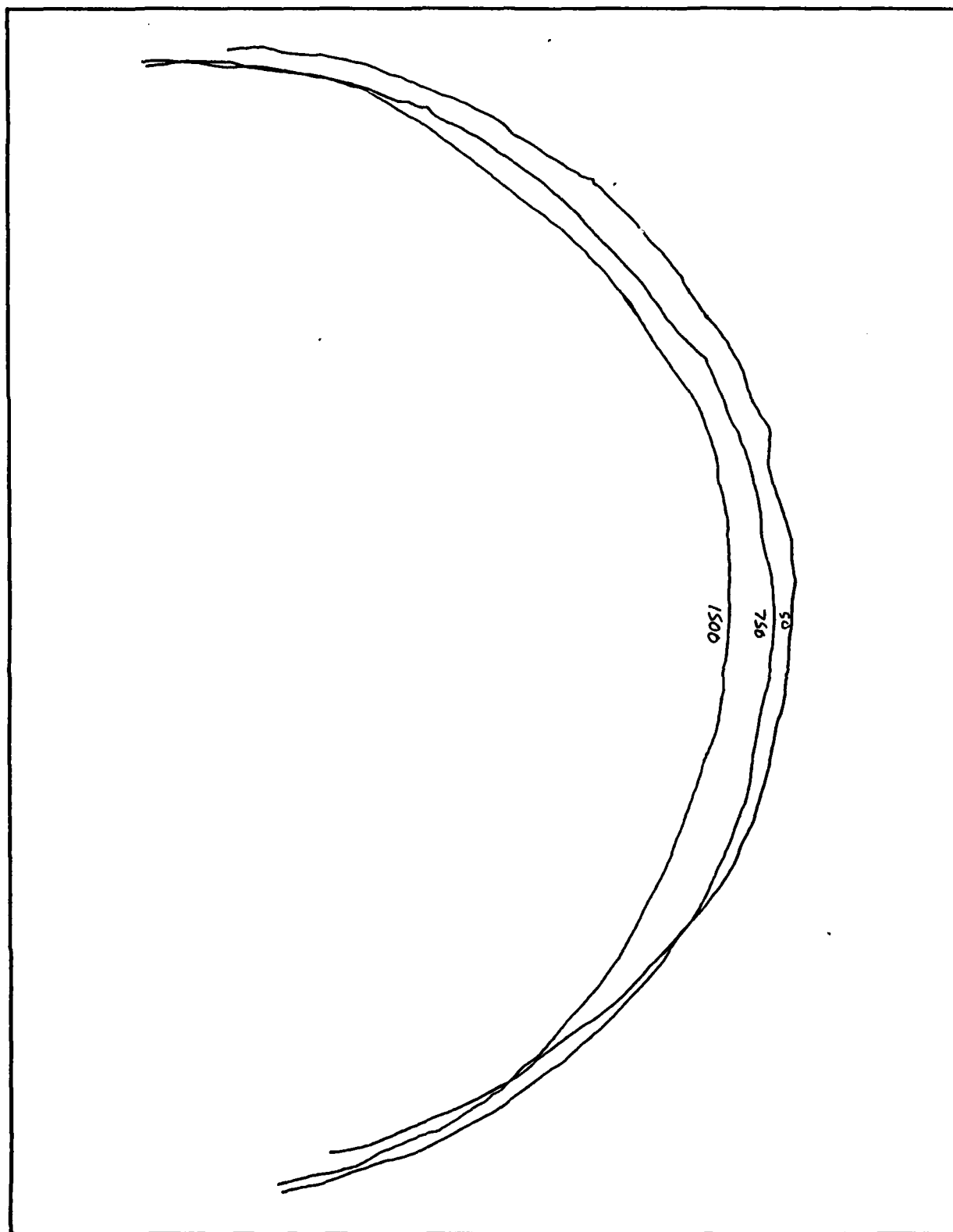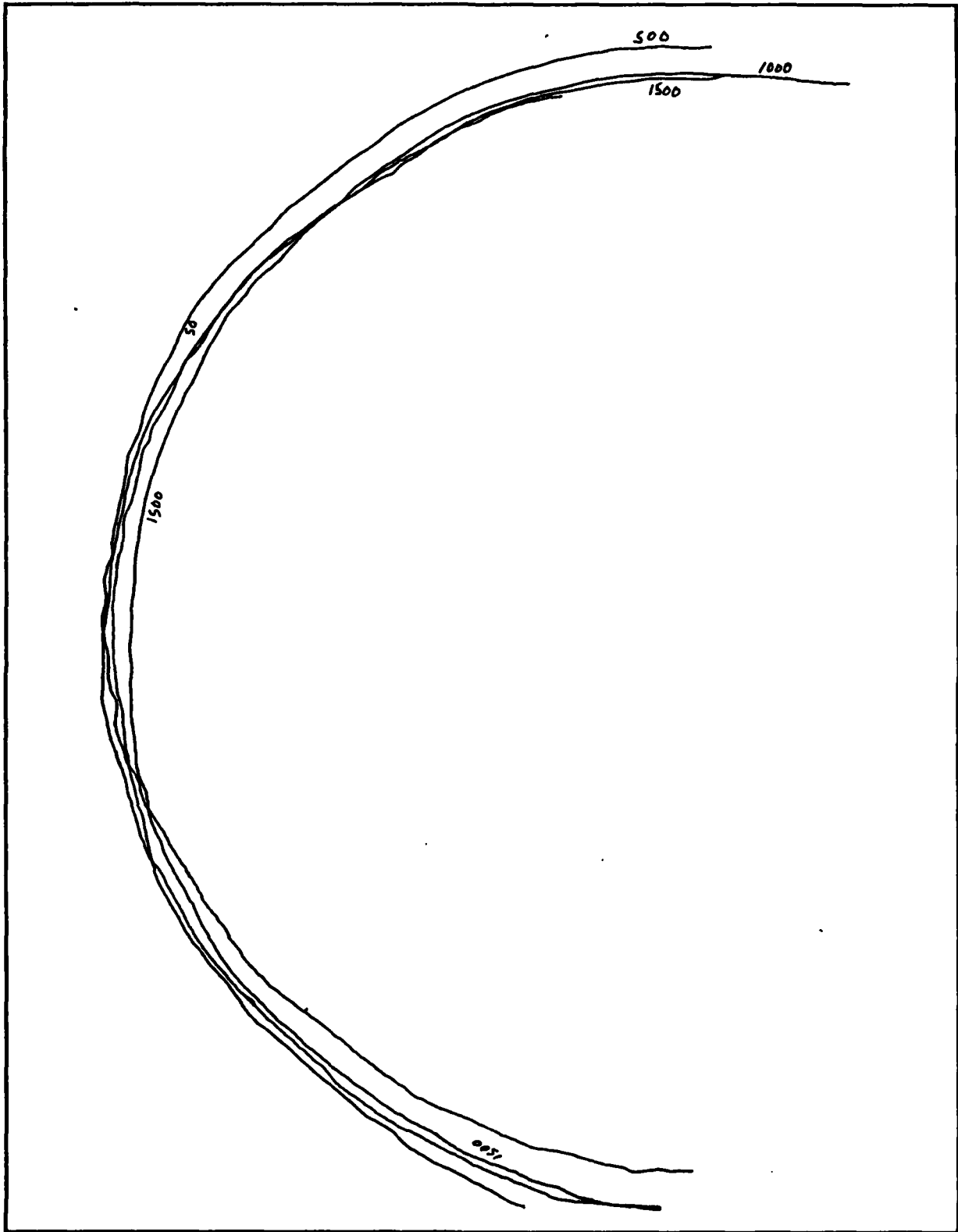**Figure 67** Run 18 Tracing

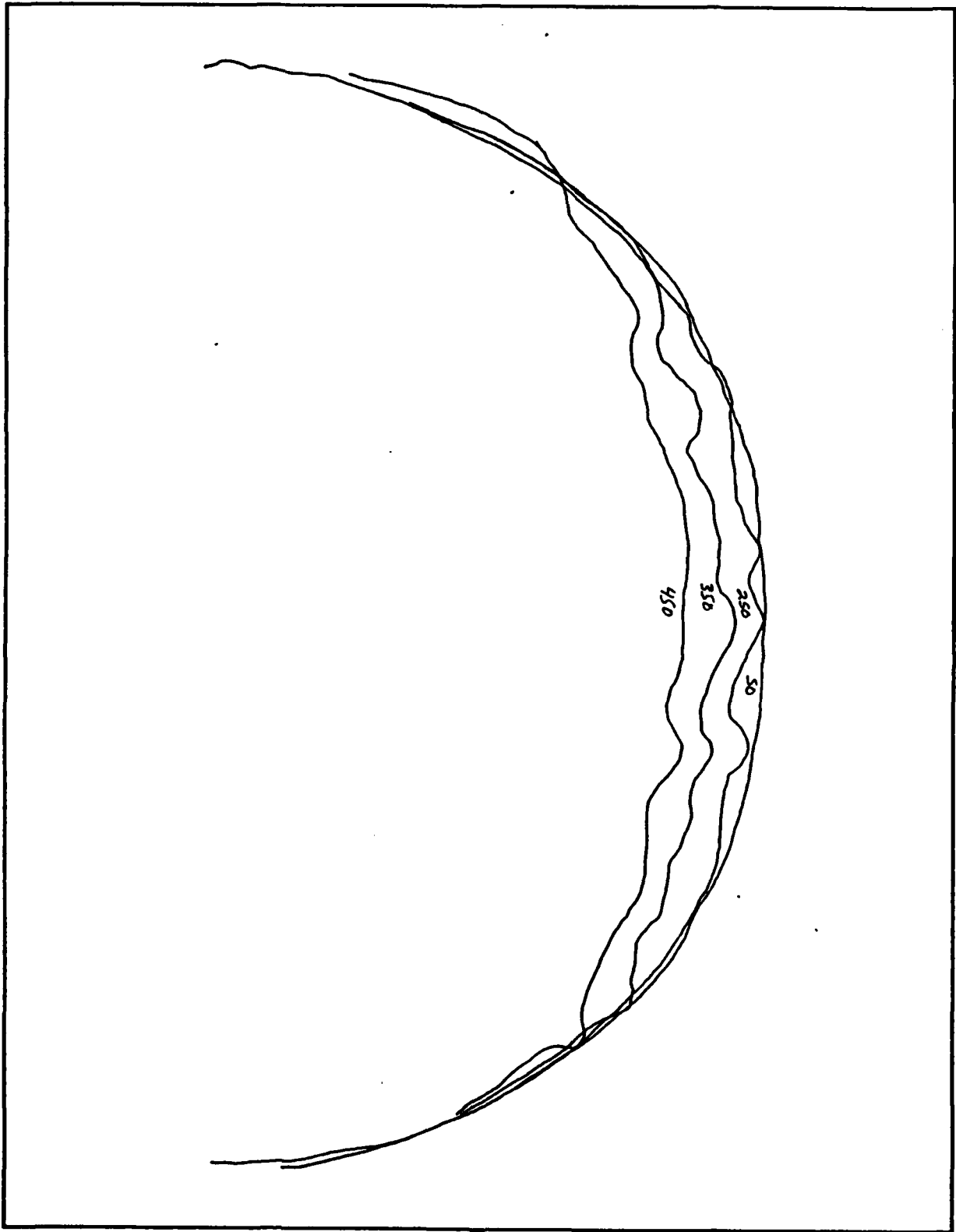Figure 68 Run 19 Tracing

99

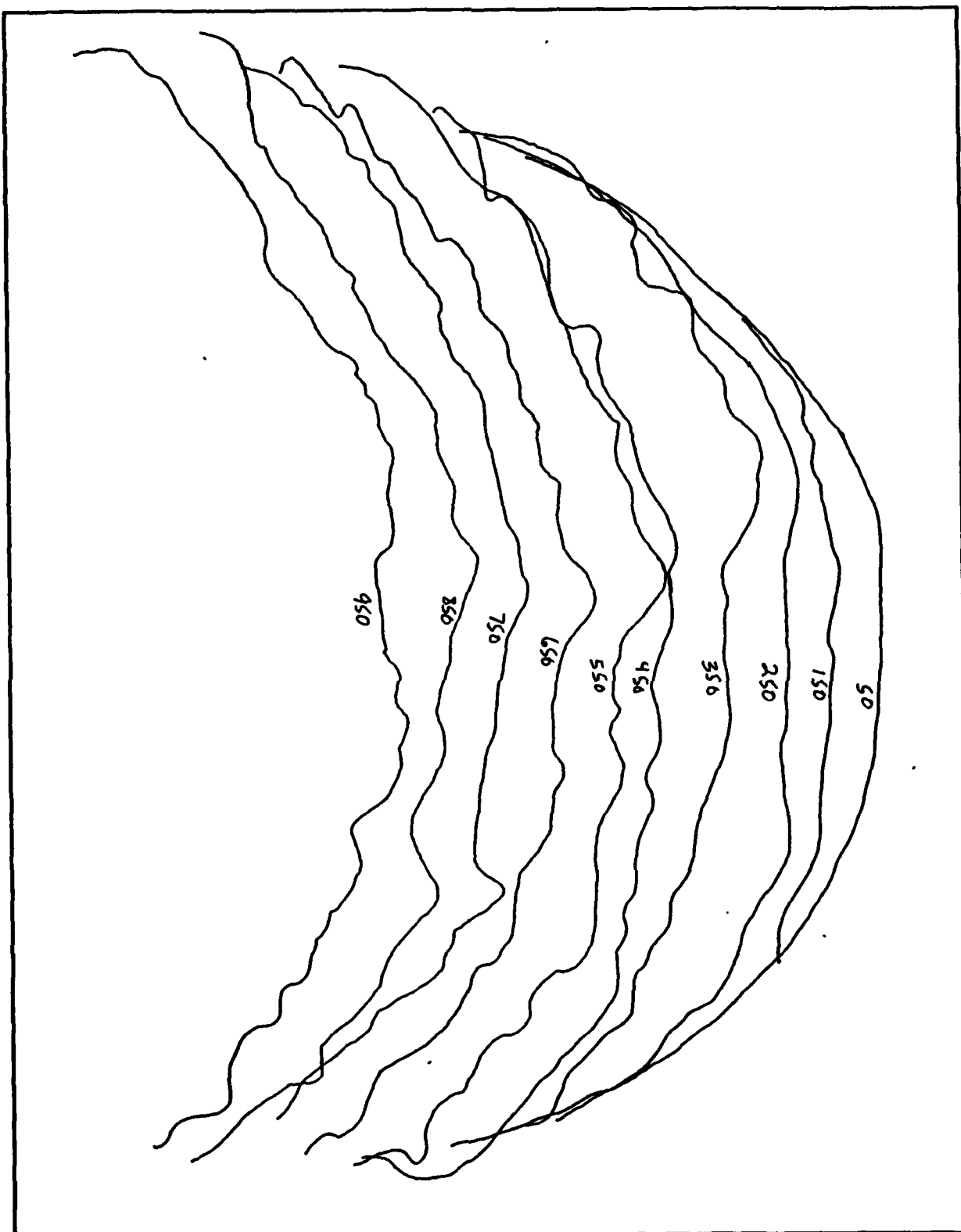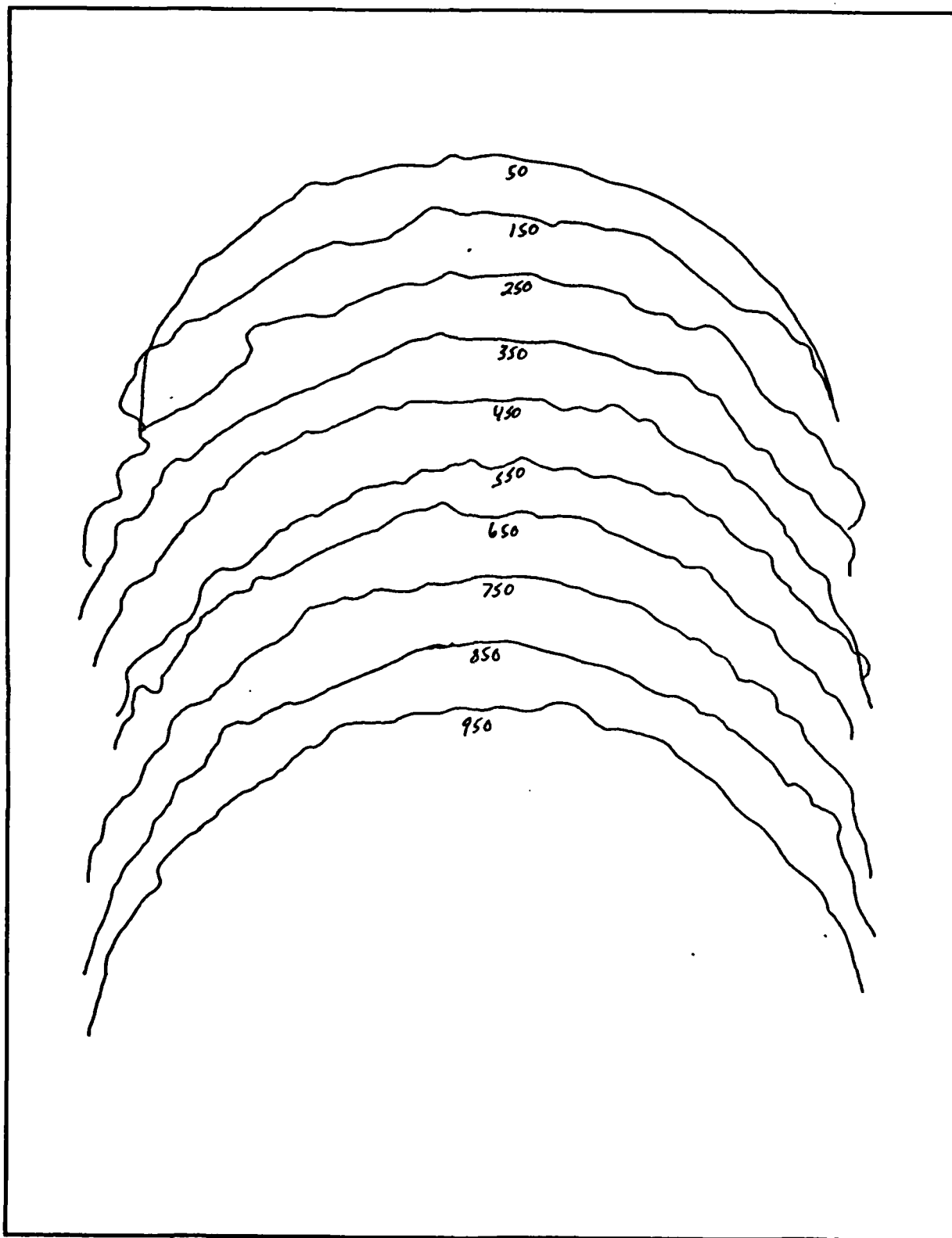**Figure 69** Run 22 Tracing

Figure 70 Run 23 Tracing

Figure 71 Run 24 Tracing

Figure 72 Run 25 Tracing
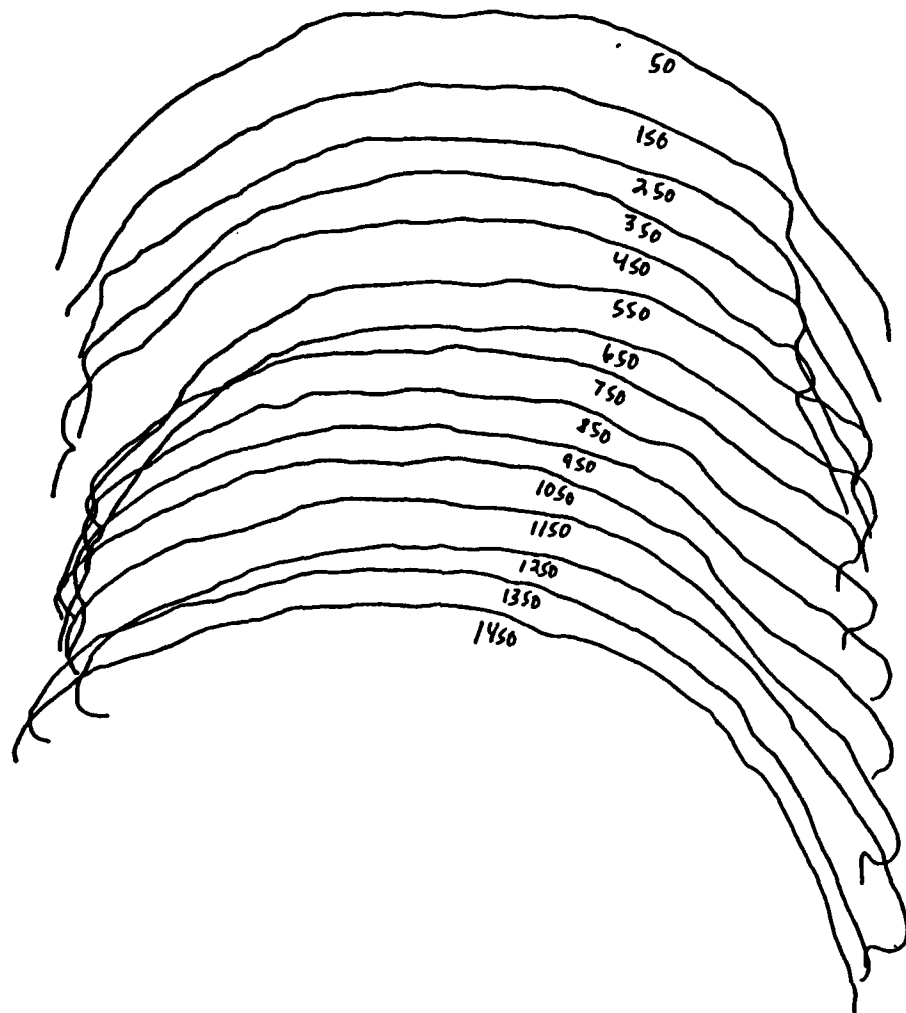
Figure 73 Run 26 Tracing

Figure 74 Run 27 Tracing

50
156
250
350
450
550
650
750
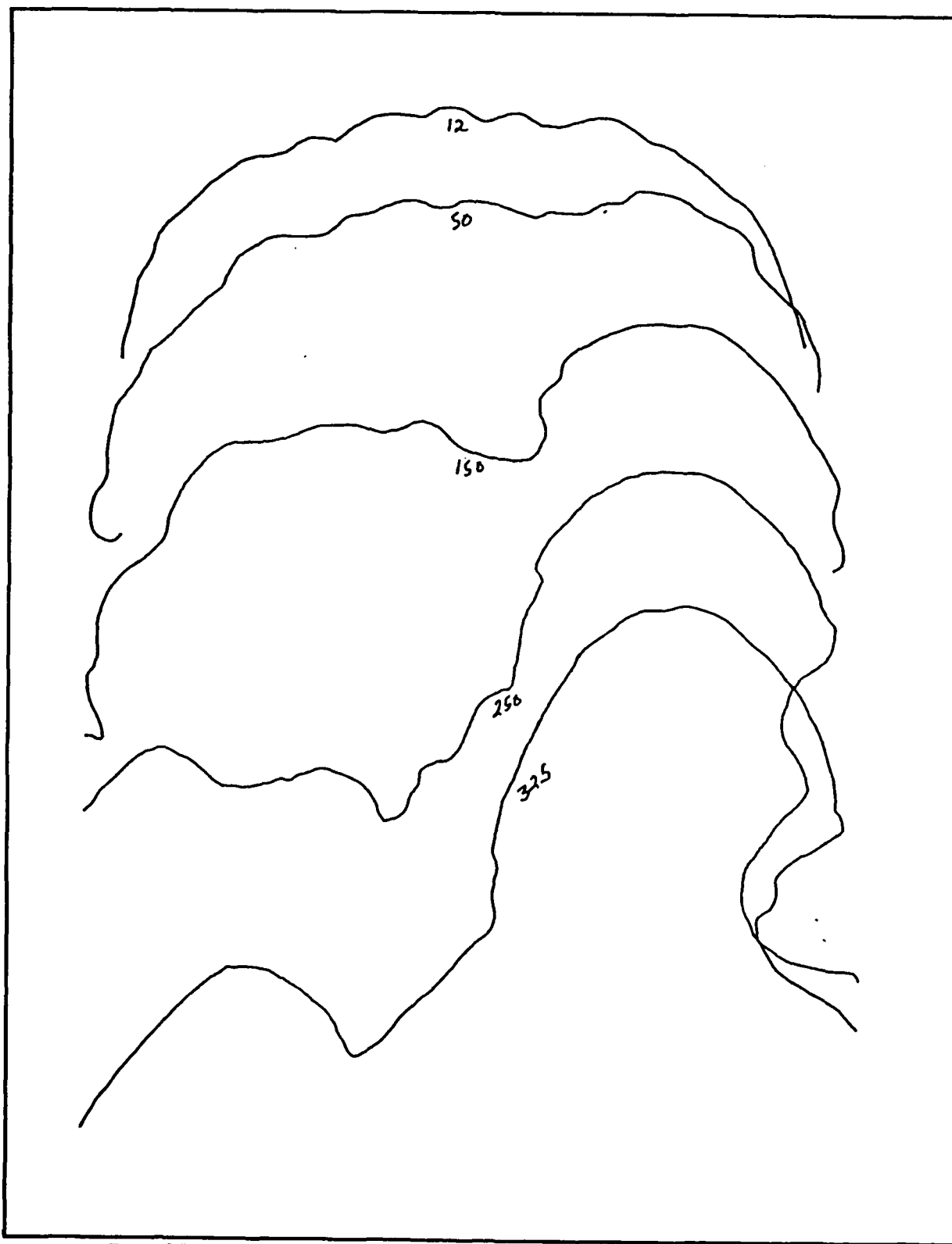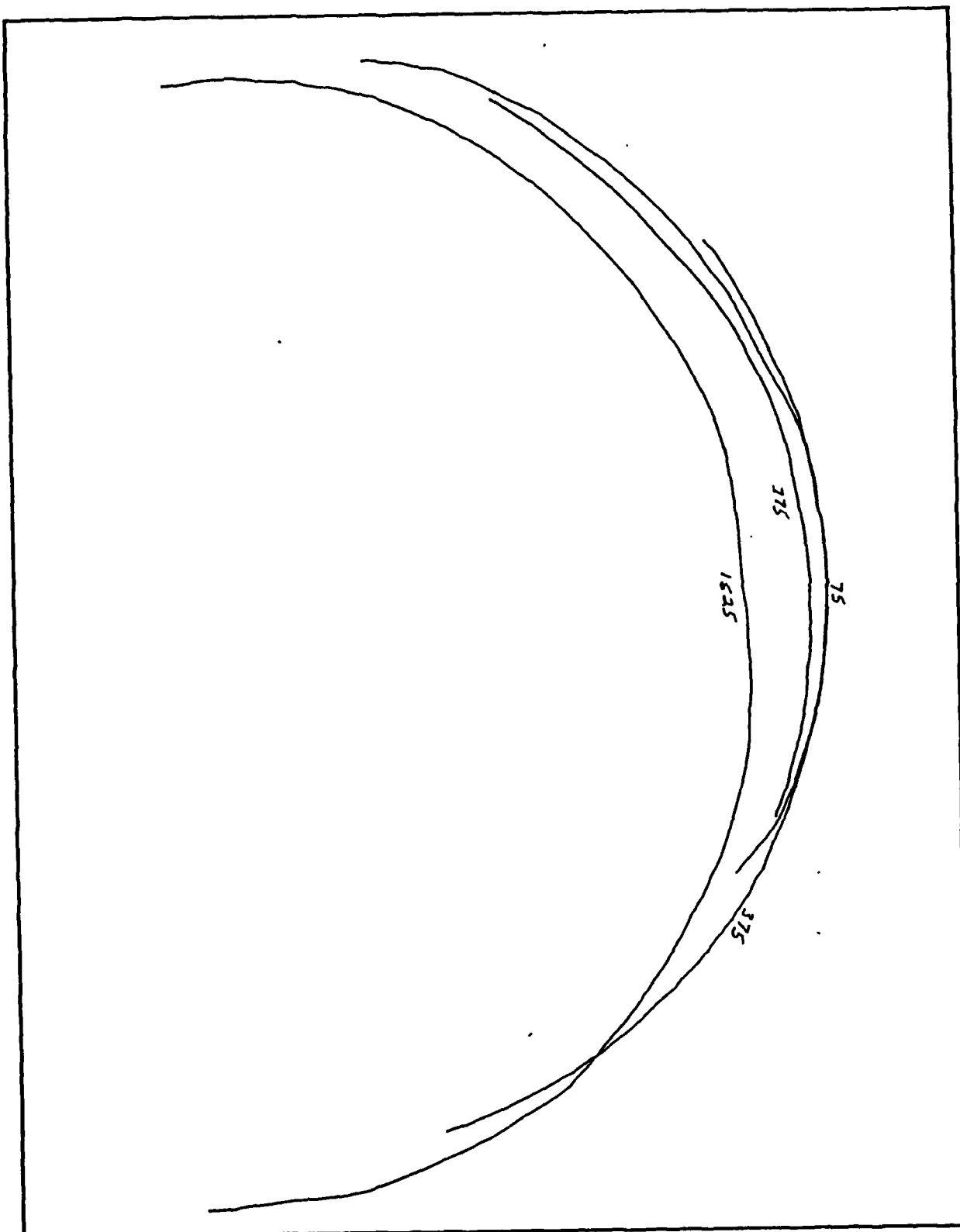850
950
1050
1150
1250
1350
1450

Figure 75 Run 28 Tracing

106

Figure 76 Run 29 Tracing

Figure 77 Run 30 Tracing

MATHCAD_{TM} PROGRAM

$a := 50 \ ..100$

$$R_a := \frac{a}{1200}$$

$T0 := 492$

$Tw := 5040$

$\sigma := 4.758 \cdot 10^{-13}$

$\S H_v := 5500$

$\lambda := 0.5$

$mdv := .0001$

$hw := Cp \cdot (Tw - T0)$

$Hw := \S H_v + hw$

VARIABLES

$Peo := .085$

$Cp := .33$

$Hs := 22500$

$V_{inf} := 25720$

$Tw_i := 2290 \cdot 1.8$

$Rec_{rate} := .237$

$\rho := 9$

$$mdt := \frac{Rec_{rate}}{12} \cdot \rho$$

$mdt = 0.1778$

$$Q_{0_a} := \frac{89.74}{Hs} \cdot \left[\frac{V_{inf}}{10000}\right]^2 \cdot \sqrt{\frac{Peo}{R_a}}$$

given

$$Q_{t_{size}} := \frac{2 \cdot \lambda \cdot mdv}{\exp\left[\frac{2 \cdot \lambda \cdot mdv}{Q_{0_{size}}}\right] - 1}$$

$$Q_{t_{size}} \cdot (Hs - hw) - mdv \cdot Hw \approx \sigma \cdot Tw_i^4 + mdt \cdot hw$$

$mdvr := find(mdv)$

$mdvr = 0.0092$ $\qquad Q_{0_{size}} = 0.0266$

$mdm := mdt - mdvr$

$mdt = 0.1778$

$mdvr = 0.0092 \qquad size \equiv 100$

$mdm = 0.1686$

$Hw = 7.0008 \cdot 10^3$ $\qquad mdt \cdot hw = 266.7743$ $\qquad mdvr \cdot Hw = 64.3955$

$hw = 1.5008 \cdot 10^3$ $\qquad \sigma \cdot Tw_i^4 = 137.3588$

$Hs = 2.25 \cdot 10^4$ $\qquad\qquad\qquad\qquad \sigma \cdot Tw_i^4 + mdt \cdot hw = 404.1331$

LIST OF REFERENCES

1. Henline W.D., "Phenomenological Study of the Thermal Response of Vaporizing-Melting Ablators to High Enthalpy Radiating Flows", unpublished paper, NASA Ames Research Center, Thermal Protection Branch, June 1990

2. NASA Technical Note R-134,"*Aerodynamic evidence pertaining to the Entry of Tektites into the Earth's Atmosphere*",Chapman, Larson, and Lewis, 1962

3. Bethe H.A. and Adams M.C., "A Theory for the Ablation of Glassy Materials", *Journal of the Aero/Space Sciences*, v. 26, n. 6, pp. 321-328, June 1959

4. Acruex Corporation, *Aerotherm Charring Material Thermal Response and Ablation Program*, November 1987

5. NASA Technical Note R-224, "*Convective Heat Transfer in Planetary Gases*", Marvin J.G. and Deiwert G.S., July 1965

6. Mitvalsky G. and Russell Y.S., "*Interaction Heating Facility Operations and Maintenance Manual*", Thermophysics Facilities Branch, Thermoscience Division, NASA Ames Research Center, December 1986

7. NASA Technical Note D-1556, "*The Lunar Origin of Tektites*", Chapman D.R. and Larson H.K., February 1963